Novel Catalytic Material with Enhanced Heterogeneous Contacting Efficiency for VOC Removal at Ultra-short Contact Time

by

Sabrina Wahid

A dissertation submitted to the Graduate Faculty of
Auburn University
in partial fulfillment of the
requirements for the Degree of
Doctor of Philosophy

Auburn, Alabama
May 4, 2014

Keywords: Microfibrous entrapped catalyst, VOC removal, heterogeneous contacting efficiency, pressure drop, wash-coated monolith, computational fluid dynamics

Approved by

Bruce J. Tatarchuk, Chair, Professor of Chemical Engineering
Yoon Y. Lee, Professor of Chemical Engineering
William R. Ashurst, Professor of Chemical Engineering
Ruel A. Overfelt, Professor of Materials Engineering

Abstract

Gas processing operations conducted at high velocities (e.g., filtration and catalytic reaction) require specialized media and structure in order to achieve the highest possible level of filtration and/or reaction per unit of pressure drop. A novel catalyst structure, microfibrous entrapped catalyst (MFEC), has potential to achieve high conversion with negligible pressure drop in cases requiring high mass flow rates, compared to other media, e.g., wash-coated monoliths and catalyst particulates in packed bed reactors. These composite structures provide distinctive physical properties in terms of void volume, surface area, porosity, permeability, conductivity, ease of pleating, uniform structure, etc. MFECs are prepared by entrapping small catalyst/support particles into the microfibrous materials by wet lay paper making process followed by sintering in hydrogen. These materials are in the form of thin flexible sheets. In this work, pleated structures (e.g., flat, V-shaped, and W-shaped structure) of MFECs, containing mixed metal oxide catalyst, were investigated systematically for VOC removal (e.g., ethanol, toluene, and n-hexane) at various face velocities and low temperatures. The optimized structure of MFEC resulted low intra-layer residence time with significantly low pressure drop. The study showed that low intra-layer residence times had significant effect on the catalytic reaction which followed Mars-Van Krevelen mechanism in this unique velocity controlled region. The overall rate of reaction for VOC decomposition was limited by the surface reaction regardless to the tested catalysts (Chapter III).

In this study, the performance of pleated MFECs was calculated in terms of heterogeneous contacting efficiency (η_{HCE}) which relies on the logarithmic removal of reactant concentrations per unit of the pressure drop ($\eta_{HCE} = log(C/C_o)/\Delta P$). The critical pressure drop denominator in the above noted expression was determined and compared theoretically, computationally and experimentally for both flat as well as pleated structures. For theoretical modeling, porous media permeability (PMP) equation, which is a modified Ergun equation, was altered by a factor for dealing with the dimensional heterogeneity created by the fibers and particles, Reynolds number and shape factor dependent form drag co-efficient, and a pleat factor for estimating decreased face velocities inside the media of the pleated geometry. This developed model was segregated into the inertial loss and the viscous loss, which together address the friction factor and the form drag factor. For computational modeling, simulations were performed by ANSYS FLUENT using a turbulence flow model. This study explicated solution methods, and discretization techniques for determining pressure drops and fluid flow characteristics across the pleated media. In Chapter IV, a detailed discussion on comparative pressure study has been presented.

Furthermore, head-to-head theoretical and experimental performance comparisons for flow through pleated MFEC structures were made with conventional packed beds of various particle sizes and wash-coated monolith of different CPSI. This study showed that while packed bed had resulted higher pressure drops and monolith had caused low fluid-solid mass transfer rates, pleated MFEC had shown significantly improved performance in VOC removal in terms of conversion along with a significant reduction in pressure drop. Small particles in MFEC enhanced the intra-particle and inter-phase mass transfer rates and the flexibility of pleating lowered the effective velocity inside the media that resulted lower pressure drop and higher

conversion. To verify the theoretical comparison, experimental pressure drops and VOC conversions at various flow rates were measured using pleated MFEC and wash-coated monolith. Furthermore, a reaction kinetic model was developed for pleated MFEC considering the Peffer's model to substantiate the experimental results in the velocity controlled region (Chapter V).

Moreover, catalyst characterization of mixed metal oxide was performed in this study using different techniques to investigate the effect of sintering on the support and to evaluate the critical parameters of the mixed metal oxides, i.e., active metal sites, metal dispersion, metal phase. In Chapter VI, all the techniques are discussed in details.

This study has demonstrated the potential advantages of MFEC as heterogeneous contacting systems for the use in high throughput applications as well as for applications requiring multi-log-removal capability. This will assist to design better and more practical catalytic reactor systems through the use of optimized pleated MFEC configurations. Furthermore, this may help to extend the knowledge of high single pass removal efficiency with minimum energy penalty across the contacting system.

Acknowledgments

First of all, I would like to thank the almighty Allah. Then I would like to express my sincerest gratitude to Dr. Bruce J. Tatarchuk for all his support and guidance during the research. Working under his supervision and learning from his tremendous knowledge has been a thrilling experience for me. I would also like to express my sincerest appreciation to Dr. Christopher B. Roberts and Dr. Mario R. Eden for all their efforts in improving the department and making it a wonderful place for the graduate students. The financial support from the US Army (TARDEC) for this research is gratefully acknowledged.

I would also like to thank Dr. William R. Ashurst, Dr. Yoon Y. Lee and Dr. Ruel A. Overfelt for their time and efforts in serving on the committee and for their guidance during my research. I am grateful to Dr. Curtis G. Shannon for his suggestion as the outside reader of this dissertation. I am thankful to Mr. Troy Barron for his time and support during implementing the controlling system and also for his helpful suggestion. I would like to thank all the current and past members of the Center for Microfibrous Materials Manufacturing (CM^3), especially Dr. Amogh N. Karwa for all the helpful ideas. I would like to express my earnest appreciation to Mr. Ron Putt for his encouragement and helpful ideas. I am thankful to the following staff members who have helped me to a great extent during my graduate studies: Dr. Donald R. Cahela, Mr. Dwight Cahela, Ms. Kimberly Denis, Ms. Sue Ellen Abner, Ms. Karen Cochran, and Mr. Brian Scweiker.

I am thankful to my husband A H M Shahadat Hussain for all his supports. I would also like to thank my parents, brothers, and family for their love and support during my studies. I am also thankful to my friends in Auburn for their support in my graduate study.

Table of Contents

List of Tables

List of Figures

Nomenclature

a_i	External surface area per unit volume of solid component i, (1/m)
a_p	External surface area per unit volume of catalyst particles, (1/m)
a_c	External catalyst surface area per unit vol. of catalyst (1/m)
C_A	Gas-phase concentration of reactant (ppmv)
C_{in}	Reactant concentration at the inlet (ppmv)
C_{out}	Reactant concentration at the outlet (ppmv)
C_D	Co-efficient of drag
C_f	Co-efficient of friction
C_{FD}	Co-efficient of form drag, $(\mathrm{C_{FD}} = \mathrm{C_D} - \mathrm{C_f})$
Cr	Correction factor
C_2	Inertial resistance factor (1/m)
c_F	Forchheimer or inertia coefficient
D_c	Characteristic length of reactor (m)
D_i	Diameter of the solid component i, (m)
D_p	Catalyst particle diameter (m)
D_m	Molecular diffusivity (m^2/s)
D_e	Effective diffusivity inside catalyst (m^2/s)
d_{ch}	Monolith channel width (m)
E_A	Activation energy of reaction (kJ/mol)

f	Friction factor
f_F	Fanning friction factor
Gz	Graetz number, $\mathrm{Re_{ch}Scd_{ch}/L}$
GHSV	Gas hourly space velocity (h^{-1})
K_L	Co-efficient of friction for sudden contraction and expansion
K_V	Equilibrium rate constant of VOC
K_O	Equilibrium rate constant of oxygen
k_s	Specific reaction rate constant
k_{eff}	Effective reaction rate per unit catalyst volume (1/s)
k_f	Gas phase mass transfer coefficient,(m/s)
k_m	$\mathrm{k_f a_c}$, (1/s)
k_r	Surface reaction rate per unit catalyst volume (1/s)
L	Length/Thickness of reactor bed (m)
M_i	Molecular weight of gas component i (g/mol)
M_{AB}	$2[(1/\mathrm{M_A}) + (1/\mathrm{M_B})]^{-1}$, (g/mol)
n_p	Number of catalyst particles
ΔP	Pressure drop across the reactor (kPa)
Pe	Reactor Peclet number
PF	Pleat factor
p	Order of accuracy
Re	Reynolds number, $\mathrm{D_c v_o \rho/\mu}$
Re_{ch}	Reynolds number based on monolith channel width, $\mathrm{d_{ch} v_o \rho/\mu}$
Re_p	Reynolds number based on particle diameter, $\mathrm{\varphi_p d_p v_o \rho/\mu}$

r	Grid refinement factor
r_v	Rate of reaction (ppmv/s)
Sc	Schmidt number
Sh	Sherwood number
T	Temperature (K)
t_w	Catalyst wash-coat thickness (m)
t_c	Monolith wall thickness (m)
v_o	Face velocity (m/s)
x	Position along the reactor length (m)
x_i	Volume fraction of solid component i
x_p	Volume fraction of catalyst support particles
x_{FD}	Form drag parameter, $\varepsilon^2/12(1-\varepsilon)$
W	Function of γ, $W = 2 - 3\gamma + 3\gamma^5 - 2\gamma^6$

Greek Symbols

ρ	Gas density (kg/m^3)
ρ_c	Catalyst support density (kg/m^3)
μ	Viscosity (kg/m*s)
τ	Bed tortuosity, $1 + (1-\varepsilon)/2$
τ_p	Particle tortuosity
ε	Bed void fraction
γ	$(1-\varepsilon)^{1/3}$
θ	Flow path angle through bed

φ_p	Sphericity of catalyst particles, $6/D_p a_p$
φ_i	Sphericity of solid component i, $6/D_i a_i$
α	Porous media permeability (m^2)
η	Internal effectiveness factor
Φ	Thiele modulus
η_{HCE}	Heterogeneous contacting efficiency

Chapter I

Introduction and Literature Survey

I.1 Problem Identification and Significance

For the last few decades, adverse health effects from poor indoor and outdoor air quality are attracting more attention to the modern societies. The decline in the air quality has been linked to an increase in asthma, allergies, lung cancer, respiratory cancer, and other pulmonary diseases [1]. Furthermore, poor air quality is a principal cause of personal discomforts such as headaches; fatigue; dizziness; nausea; and irritation of skin, eyes, throats and lungs that has a strong impact on the quality of life and workers performance [2]. Researcher and scientists have been engaged in several approaches for understanding the factors that are responsible for poor air quality and thus discover techniques that could be applied to make the air clean [3-12]. According to the literature, heterogeneous contacting system is the most promising technology for improving air quality. Heterogeneous contacting system is the nucleus of chemical and environmental processes. The improvement of novel heterogeneous contacting systems with enhanced efficiency is the fundamental step of strengthening chemical process. Therefore, increasingly attention is being laid upon micro-structured and micro-engineered reactor systems that utilize higher external surface areas to provide higher transport rates. Microfibrous entrapped catalysts (MFECs), a novel micro-structured material developed by Auburn University [13-17], have shown great potential as a heterogeneous contacting scheme. These provide an innovative approach for a more effective design of a small, efficient, and lightweight heterogeneous contacting system. Microfibrous entrapped ZnO/SiO_2 has shown remarkable improvement (2-3 folds) over packed bed reaction rates in gas phase desulfurization of hydrogen reformate streams [18-26]. Moreover, significant improvements in conversion and selectivity

have been achieved by using these materials for preferential catalytic oxidation and low temperature oxidations of CO in hydrogen reformate streams [27, 28]. Microfibrous entrapped activated carbon beds and Ni/Al_2O_3 catalysts have shown substantial benefits in volatile organic compound (VOC) adsorption [29, 30] and in toluene hydrogenation in trickle bed reactors [31] , respectively. Furthermore, pleated MFEC for single pass removal of molecular contaminants has shown better performance than packed beds and commercial monolith [32]. In addition, an application of Cu MFEC in Fischer-Tropsch synthesis (FTS) has demonstrated an improvement in temperature distribution inside the catalyst bed and an increase in product selectivity [33].

Under the Clean Air Act, EPA regulates 187 toxic air pollutants where more than 90% pollutants belong to VOCs. Toxicity levels, or the potential for adverse effects on human health and the environment, vary from pollutant to pollutant [34]. Regulations governing automotive emissions are increasing in number and stringency. There is a constant need for technological innovation to reduce emissions levels as more vehicles are produced. In high performance platforms i.e. military tanks, ships, aircraft, fuel cells, turbo machineries, etc., catalytic converter to control the emissions of toxic compounds i.e. VOCs, needs to be small, lightweight and capable of performing at high fluid velocities. Current technology for emissions control consists primarily of ceramic-based catalytic converter either in pelleted or cellular form. In general the ceramic monolith has gained greater acceptance in high-flow velocity operation due to the low pressure drop inherent in its configuration. Although these catalytic converters are 95% effective once these reach the operating temperature, these are ineffective during the engine start up and provide low fluid-solid mass transfer rates. Furthermore, the physical properties of these ceramic substrates are not ideal since these are relatively fragile and liable to thermal shock fracture. All the previously mentioned experimental studies have shown great advantages with the use of

microfibrous materials. Therefore, this unique structure can be a potential mean to remove toxic substances from high performance systems by utilizing their distinctive properties. Hence, the intent of this research is to employ MFECs in a high volumetric system, which retains the operating conditions of the above mentioned exhaust schemes, in order to remove toxic VOCs at short contact time as well as investigate the reaction mechanism in order to model the transport rates in these materials.

Packed beds and wash-coated monoliths are intended commercially as catalytic reactors for the application in VOC abatement technique [11, 12, 35, 36]. However, packed beds result higher pressure drops although they have high fluid-solid mass transfer rate. This high pressure drop issue can be solved by wash-coated monoliths, but monoliths cause low fluid-solid mass transfer rates and non-uniform fluid distribution, which causes lower reactor effectiveness. Pleated MFEC can be more effective approach to eliminate these difficulties. Therefore, another important purpose of this study is to implement a comparative performance study – theoretical and experimental, among different heterogeneous contacting systems – packed beds of different particle sizes, monolith of different CPSI and different pleated MFEC. For this purpose, a performance evaluation parameter is required to introduce which will consider the performance aspects of reactor geometries.

Furthermore, as almost every process uses a porous media, e.g. fixed bed reactors, packed distillation columns, adsorbent beds, filters, heat pipes, etc., pressure drop is an extremely important criterion for reactor and filter designs. Therefore, pressure drop should be checked at the early stage in the design with the purpose of assessment its influence. Typically, the blower energy requirement is calculated in terms of the pressure drop per pass of the heterogeneous contacting system. In the literature, several equations are available for predicting the pressure

drop across a system. However, these equations are applicable only for a certain range of porosity, either for low porosities or for porosities approaching unity. Cahela and Tatarchuk [13, 37] have developed an equation for porous media permeability (PMP) that is directly applicable for MFEC. Moreover, with the aim of understanding the basic physical and chemical characteristics of MFEC and optimizing the effectiveness and performances, computational fluid dynamics (CFD) have been applied to predict pressure drops across the media [38] and to measure the increase in mass transfer rates due to the fibers [39]. Duggirala et. al [38] has shown that CFD can provide insights into the detailed fluid mechanics, as well as the global properties of the flow. Therefore, based on the previous studies, supplementary purpose of this research is to develop a semi-empirical pressure drop model for multi-elemental structural array of MFECs and employ CFD to understand the fluid flow characteristic inside the porous media.

I.2 Microfibrous Entrapped Catalysts/Sorbents (MFECs/MFESs)

I.2.1 Introduction:

Microfibrous entrapped catalysts/sorbents (MFECs/MFESs), which were developed by Auburn University for use in chemical and electrochemical application, are now commercially available at IntraMicron Inc., AL [13-17]. The media is a sinter-locked structure of fibers, with diameters typically ranging between 2 and 20 μm, which can entrap small particulates of catalysts or sorbents from 50 to 300 μm. The choice of fiber materials can be metals (e.g. copper, nickel, and stainless steel), glass or polymer, depending upon the process consideration. Fig.I.1 (a) and Fig.I.1(b) show typical micrographs of a metal microfiber media. MFEC is prepared by the conventional wet-lay paper making process. The properties of the fiber can also be tailored that is conditional to the process requirement. The surface area of MFEC can vary roughly from

1.5 m^2/g to about 1500 m^2/g, depending on the fraction of high surface area material. The typical volume loadings of the catalyst and of the fibers in MFEC are about 10 to 25%, and 1 to 5%, respectively, with rest being void.

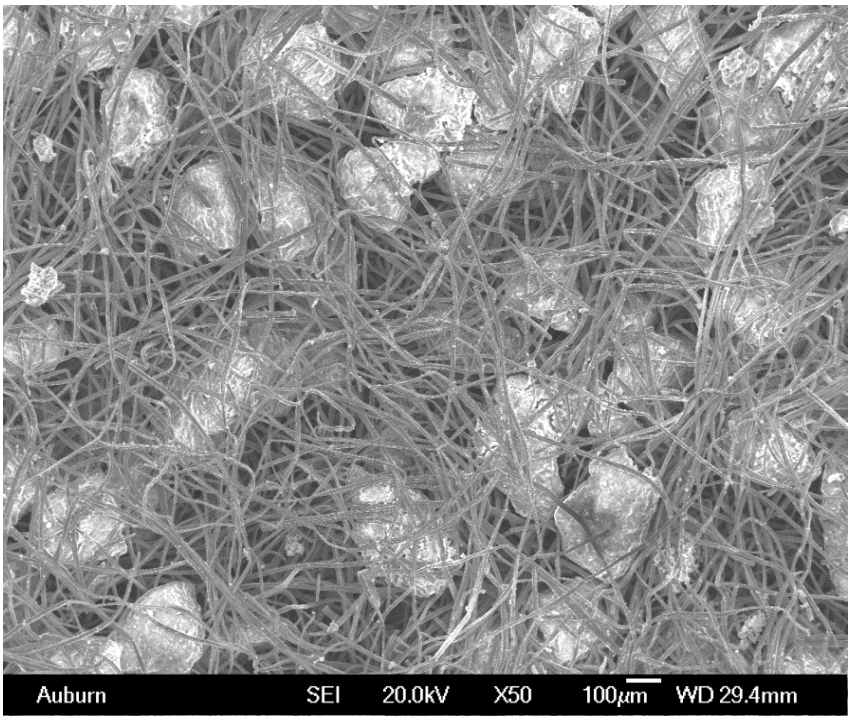

Figure I.1(a)

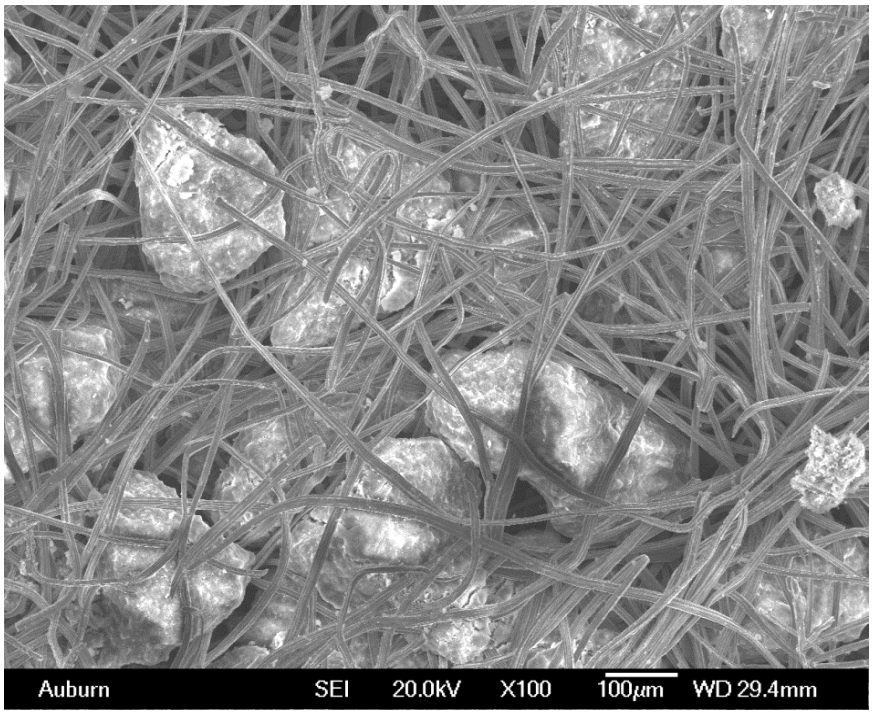

Figure I.1(b)

Figure I.1 (a) and (b): Micrographs of 150-250 μm γ-Al_2O_3 entrapped in 8 μm nickel fibers

Due to the extraordinary ability to entrap small catalyst particles, MFECs have exhibited a great promise to increase the intra-particle and the inter-particle mass transport rates. As MFECs are prepared by the wet lay process [16], microfibers and catalyst particles assemble themselves in a manner to form almost uniform structures; this uniformity eliminates "channeling" or "flow maldistribution". The high voidages in MFEC reduce pressure drop significantly. Another unique feature of MFEC is their flexibility of pleating, which helps to achieve higher conversion and lower pressure drop. Furthermore, due to the high aspect ratio (length to diameter) of fibers, MFEC decreases axial dispersion and improves radial dispersion, and thereby, creates a plug flow like condition.

I.2.2 Method of Preparation:

The method of microfibrous media preparation varies depending on the fiber materials and diameters that are used. The specific method of preparation of MFECs has been discussed elsewhere. A basic preparation procedure has been discussed below -

The common raw materials used in this preparation process are as follows:

1. Microfibers (metal, glass or polymer),
2. Catalyst support/adsorbent particles,
3. Cellulose,
4. Viscosity modifiers and miscellaneous

The whole process undergoes the following four basic steps:

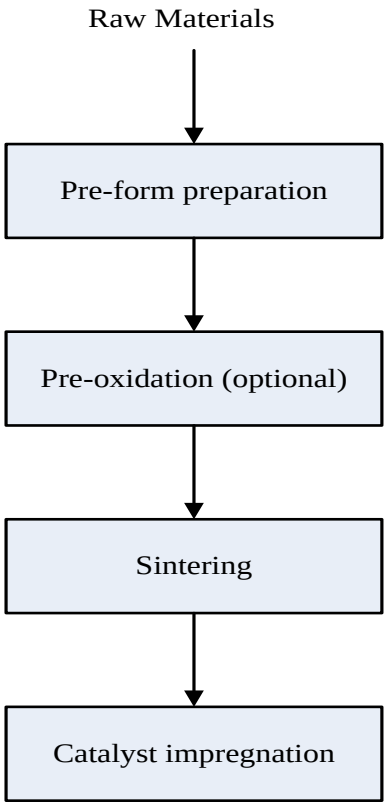

Figure I.2: Process flow diagram of MFEC preparation

I.2.2.1 Pre-form Preparation:

The first step for microfibrous media preparation involves pre-form preparation. In this step, required weights of microfiber and cellulose are dispersed in excess water using a blender to prepare homogeneous suspension. For well dispersion of the fibers, small amount of appropriate viscosity modifiers, for example, 0.75% (w/w) of water resistant compound, Hydroxy ethyl cellulose (HEC), can be used which undergoes hydrolysis process at pH~10 using sodium hydroxide. The resulting suspension is placed into the head box of the paper making equipment. Required amount of catalyst supports or sorbents are then added to the hand-sheet former while simultaneously stirring the suspension to ensure well dispersion of the particles into the fiber, and to form uniform structure. Finally, the excess water is drained out of the suspension. Hence, catalyst/sorbent particles are entrapped in the fiber matrix as the particles along with the fiber and cellulose settle on the bottom of the screen of the wet-lay equipment. These pre-forms are removed from the screen and dried at 373 K. Thus, the pre-form of MFEC is formed as a three-dimensional structure consisting of particles, fibers, and cellulose. Cellulose acts as temporary binders which provide wet and dry strength to the pre-form by hydrogen bonding.

I.2.2.2 Pre-oxidation:

This is an optional step. In this step, dried pre-form is oxidized in air diluted by N_2 gas (about 5% O_2 in N_2) at 773 K. The purpose of this step is to remove the cellulose and the associated carbon from the pre-forms. However, as most of the cellulose is removed during this step, the pre-forms become sensitive for handling.

I.2.2.3 Sintering:

The sheets from the pre-form preparation step or the pre-oxidized sheet goes through the sintering process at a suitable temperature depending on the microfiber materials. Sintering of metal fibers is done in an hydrogen enriched atmosphere at different temperatures depending on the metal, for examples, for copper at about 873 K to 1023 K, nickel at about 1173 K to 1273 K and stainless steel 1273 K to 1473 K; while ceramic and polymer fibers are sintered in air at 973 K to 1273 K and 423 K to 473 K respectively. During this process, fibers bond with each other and form the sinter-locked matrix. Although surface areas and pore volumes of several common catalyst supports like γ-alumina and silica gel are affected by the high temperature and/or hydrogen treatment during sintering process, these changes in properties are relatively insignificant which has been discussed elsewhere [31]. The overall preparation of MFECs has negligible effect on the degradation of most of the catalyst supports or adsorbents.

I.2.2.4 Catalyst Impregnation:

Depending on the process requirement, active materials are dispersed on high surface area support particles entrapped in fiber matrix. In this step, catalyst/active materials can be impregnated by conventional incipient wetness method, followed by calcination in air and reduction by hydrogen at required temperature.

I.3 Volatile Organic Compounds (VOCs):

Volatile organic compounds (VOCs) are solvents and other compounds that have boiling points in the range of 323-533 K at room temperature and atmospheric pressure, and contribute to the formation of photochemical smog. Some solvents, such as acetone, methylene chloride (in paint stripper), Freons (used as refrigerant), and other fluorinated/chlorinated compounds are VOCs, however, they do not contribute to the formation of smog in any significant manner. Therefore, although these are VOCs, Environmental Protection Agency (EPA) deems these to be exempt from the "VOC" classification. In other words, air pollution regulation that limit the use of "VOCs" exempt those compounds that have a negligible effect on the formation of photochemical smog [40]. Therefore, according to this definition, a wide variety of organic compounds, such as aliphatic, aromatic and chlorinated hydrocarbons, aldehydes, ketones, esters, organic acids, and alcohols can be considered as VOC. Hence, according to the definition and literature survey VOCs, those are encountered in indoor and outdoor air include formaldehyde, acetic acid, acetone, acetaldehyde, acrolein, benzene, toluene, xylene, ethanol, 2-Propanol, 2-Butanone, d-Limoene, trichlorofluoromethane, decane, ethyl actetate, 1,1,1-trichloroethane, tetrachloroethane, n-hexane, methyl tert-butyl ether, naphthalene, vinyl acetate, chloromethane, dichlorofluoromethane, and so on [41-43].

VOCs are an important class of indoor and outdoor air toxics due to their short- and long-term adverse health effect [44, 45]. These are recognized as major contributors to air pollution due to their toxicity to human health and their involvement in the formation of photochemical smog. These can cause eye, nose, and throat irritation; headache, loss of coordination, nausea; fatigue, dizziness; damage to liver, kidney, and central nerve system, etc. The key signs or

symptoms associated with exposure to VOCs include conjunctival irritation, allergic skin reaction, dyspnea, and decline in serum cholinesterase levels, and so on.

I.3.1 Sources of VOCs:

In urban, domestic, and public microenvironment, there are numerous sources of VOCs. VOCs largely originate from mobile and industrial sources. Environmental tobacco smoke and vehicular emissions are the potential sources of VOCs. These sources contribute largely to the VOC concentration in indoor and outdoor air due to the incomplete combustion of fuel. Another potential source of VOC is densely populated public places such as pubs, restaurants, and cinemas. Paints, varnishes, solvents, perfumes and preservatives are also responsible for VOC emission. Microbial objects are another source of VOC, although these emit lowest amounts than other sources. On the other hand, outdoor VOCs pollutants are emitted from industrial processes and automobile exhausts. There exists vast literature on VOC sources and comparative study of different kinds of VOC emission from different sources [42, 43, 45-47].

I.3.2 Catalytic Oxidation of VOC:

VOCs are dangerous for the environment, because of their high volatility and persistence in the air. Their ability to travel long distance from their emission point and to be transformed in the atmosphere into other compounds is even more dangerous for human, fauna, and flora. Due to the progressive increase of VOCs emissions, the information of their hazardous nature and the increasingly restrictive environmental regulations in the industrialized countries has induced the development of different methods for the elimination of VOC. These methods can be classified in two different groups: non-destructive method and destructive method. In non-destructive

methods, VOC (i.e. from gaseous emissions) are retained, without chemical transformation. Adsorption, absorption, and condensation are included in this group. In destructive method, VOCs transform into other compounds, inert or less dangerous. Thermal incineration and catalytic oxidation are included in this group [48]. Selection between different alternatives depends on the nature, flow rate, concentration of pollutants, outlet requirement, and other circumstances such as presence of solids or poisons for catalysts, etc.

The conventional approach for dealing high concentration VOC stream is thermal incineration, but incineration has high operating costs, as temperatures exceeding 1073 – 1473 K are required to achieve complete VOC destruction. Incomplete or poorly controlled combustion process produces undesirable by-products such as dioxins and nitrogen oxides in the incinerator flue gas. Several alternative VOC removal techniques are available and each technique has limitations for different organic compounds, concentrations, and emission sources [49]. For example, low-temperature condensation is energy intensive and limited to the behavior of evaporative solvents [50]; biochemical methods are selective and concentration sensitive [51]; adsorption-based technique are preferable for handling highly diluted VOCs [52] but simply transfer the environmental burden from the gas phase to the solid phase.

One of the most effective and economically feasible VOC removal techniques is catalytic combustion. In this process, pollutants in a gaseous stream are oxidized completely in the presence of a catalyst. The basic of catalytic oxidation reaction of an organic molecule is shown below:

$$HC + air\ (O_2) \rightarrow CO_2 + H_2O$$

It has the advantages of providing nearly total elimination of pollutants from the effluent stream even for low concentration with no generation of organic by-products at moderate temperatures (approximately 573 K), and low operational cost. This process can be operated below the lower flammability limits of fuel oxidizer mixtures. In addition, catalytic oxidation leads to lower thermal NO_x emissions. Therefore, research on VOC catalytic removal has been done numerously for last few decades considering the previously mentioned advantages and this research field continues to be very active. The development of catalyst for VOC removal has been widely reported in the literature [53-61].

I.4 Heterogeneous Contacting Systems:

Catalysts are classified as homogeneous if these are present in the same phase as the reagents. This normally means that catalysts are present as solutes in a liquid reaction mixture. Catalysts are heterogeneous if these are present in a different phase. Heterogeneous catalytic reaction systems, in which fluid reactants are passed over solid catalysts, are currently the most widely used catalytic processes in manufacturing. Heterogeneous catalytic reactors and adsorption systems are the vital features in many chemical processing and separation applications. As these have widespread applications in industry, improvements in design have significant effects on the performance and efficiency. Brief reviews on various heterogeneous contacting systems which are widely used in the industry, selection criteria of a reactor, and major factors affecting the performance of the contacting systems have been provided.

Various configurations of heterogeneous contacting systems are available in industry such as packed beds, fluidized beds, moving bed reaction, structured configurations like monoliths, catalytic foams, wire meshes, etc. Each of these configurations has specific

advantages and disadvantages. Packed bed and fluidized bed are tubular and are filled with solid catalyst particles. Monoliths, foams, and wire mesh reactors use catalyst as a form of wall-coatings. In general, these systems are classified as moving bed and fixed bed. Some of the major contacting systems have discussed in this section. Although there are different types of moving bed (recirculating bed, moving-packed bed, etc.) exist, only fluidized bed will be discussed here. Information on other kinds of reactors may be found elsewhere [62, 63].

I.4.1 Packed Bed:

Packed beds (also called fixed bed) are the most common and basic form of heterogeneous contacting system used in the industry. It is essentially a tubular reactor that is packed with solid structured or un-structured packing or catalyst particles. Typically particles have a size range from millimeter to centimeter. As packed beds are the most basic form of heterogeneous catalysts, there had been numerous research completed and still ongoing, with the fundamental characteristics are well established [62, 63]. A schematic diagram of a typical packed bed reactor is given below in Fig. I.3.

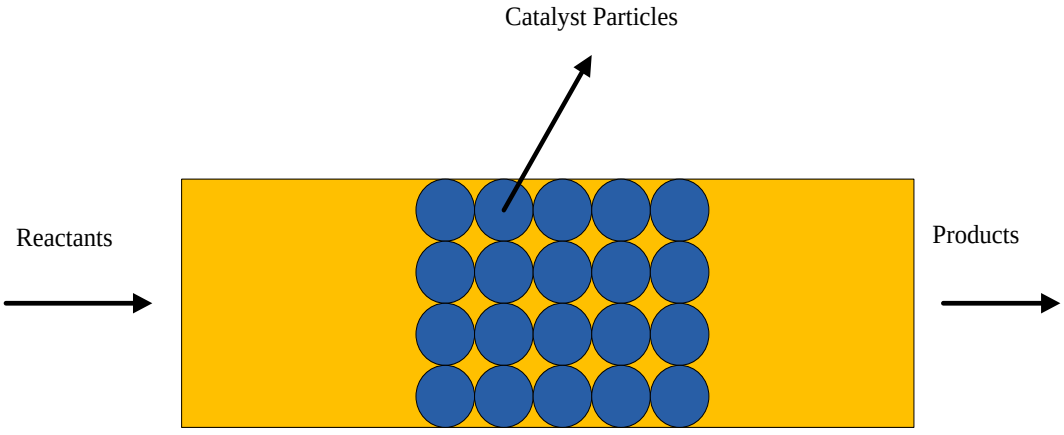

Figure I.3: Schematic diagram of packed bed

The construction of a packed bed reactor is very simple, but it has several disadvantages those make it inefficient e.g. flow maldistribution, axial diffusion, and intra-bed channeling. Although small particles in packed beds provide high intra-particle and inter-particle transport rates, these cause elutriation and plugging [62], and therefore, high pressure drop. Furthermore, as the packed beds have poor thermal conductivity, it is difficult to control the temperature of the bed; this causes undesirable temperature gradient across the system. Moreover, packed beds are not well suited for applications involving frequent regeneration and catalyst replacement since the units are difficult to service and to clean. Furthermore, as the channeling occurs, this result in ineffective use of parts of the reactor bed, creating dead volume inside the reactor. All these aspects of packed bed reactor make it an inefficient method of contacting and less suitable for applications.

I.4.2 Monolith:

Monoliths are structures that contain various types of interconnected or separated channels (straight, wavy or crimped) in a single block of material (e.g. honeycombs, foams or interconnected fibers). The channels of the most honeycomb monoliths normally have circular, square or triangular cross-sections. Monolith reactors were initially developed and used in the mid 1970s for the automotive industry to remove NO_x, CO and hydrocarbon through gas solid reaction. In the last three decade, monolith substrates have gained significance interest in automotive and stationary environmental pollution control applications [11, 64]. Details about the manufacturing process and industrial applications of monoliths can be found elsewhere [11, 65-68]. Fig.I.4 shows the general structure of a monolith. Monolithic reactors are composed of monoliths which are porous catalytic materials or catalysts are deposited in the channels of an inert monolithic support. Ceramic and metallic monoliths are mostly used in industry and in

research. These are prepared by extrusion and corrugation respectively. There are several parameters available for defining geometry. For example, square channel monoliths are defined by channel size (d_h) and either by wall thickness (t_w) or cells per square inch (CPSI). The amount of catalyst in the unit volume of reactor is determined by the monolith geometry if the monolith is extruded from a catalytic material and if the catalyst is wash-coated, then wash-coat thickness is the determined parameters. The performance of a monolith reactor is highly dependent on the prevailing flow pattern in the monolith channels. The desired flow pattern through monolith channels is segmented flow.

Monolith reactors have shown significant improvement over pellet-packed fixed bed reactors. The advantages of monolith reactor over packed bed are – lower pressure drop especially under high fluid throughput, higher specific external catalyst surface area, lower axial dispersion and back-mixing, reduction of fouling and plugging that extends the catalyst lifetime, easy to clean the particulates accumulated on the channel walls, scalable and so on. However, these have several disadvantages, for example, low radial heat transfer that creates difficulty to control temperature for thin wall ceramic monolith supports, non-uniform fluid distribution that causes lower reactor effectiveness, and higher cost in extruding and installation of large scale.

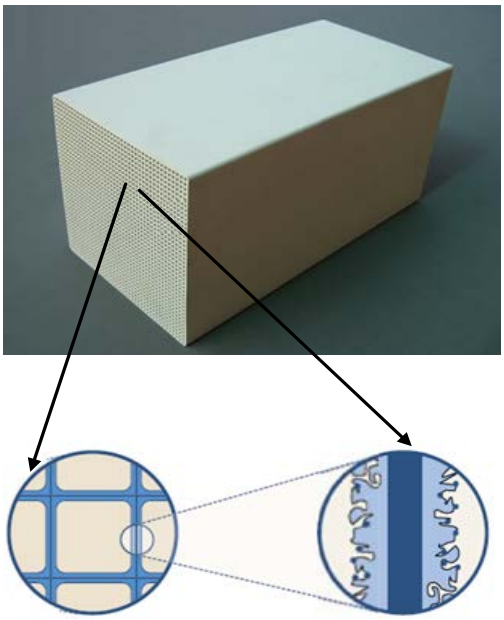

Figure I.4: Monolith structure

I.4.3 Catalytic Foam:

High-porous cellular materials (foam metals) represent a very promising type of structural materials for some fields of science and technology including catalysis. Catalytic metals have uniform cellular structure with anisotropy of mechanical and gas-dynamic properties. They consist of high voidage porous ceramic or metal alloy foams, wash-coated with catalyst support of required thickness. Subsequently, metal or metal oxide catalyst in impregnated over the wash-coated support.

The key advantage of catalytic foam is their high interconnectivity between the cell structures whereas in monolith substrates these are discrete cells. This interconnectivity enhances proper radial mixing. Catalyst foams are being used in air purification and filtration system. Richardson et al [68-72] have explained heat and mass transport phenomena, pressure drop across the media, and properties as well as application of catalyst foam.

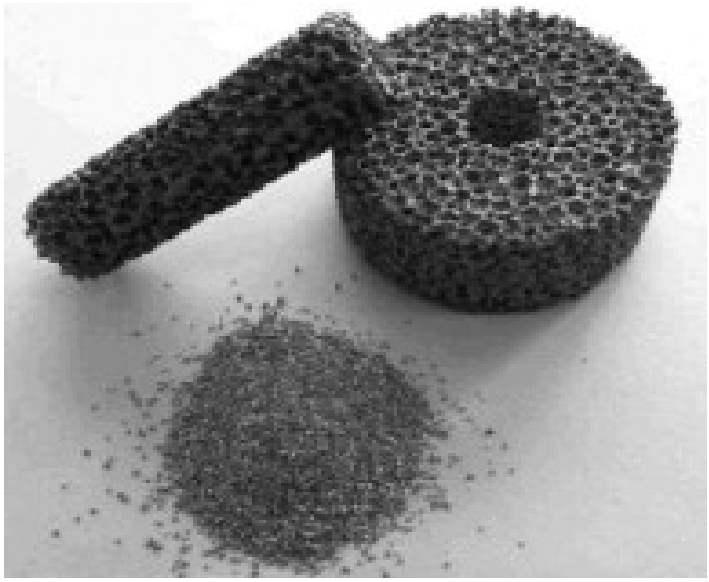

Figure I.5: Metal foam catalytic support

I.4.4 Wire-mesh Screen:

The wire-mesh screen reactor or honeycomb module is constructed from alternating corrugated sheets and flat wire mesh packed into a wire-mesh frame [69]. This type of reactor is a relatively new concept. The wire surface of each mesh is coated with high surface area catalyst particles to form a certain thickness of sintered but porous layer. The noble metals or metal oxides are impregnated by the wash-coating method on the surface of support particles. This type of wire mesh honeycomb (WMH) module design permits free radial flow because of the hole openings of the channel wall. This feature makes the WMH especially suitable for treating dust-laden exhausts, since even if the mouth of a channel is blocked by dust its rear part will remain effective. The wires also provide for direct electrical heating when required. Furthermore, the accumulation of wash-coat is greatly minimized. While this concept has great potential, it is still being researched and has not grown as a full-scale commercial product.

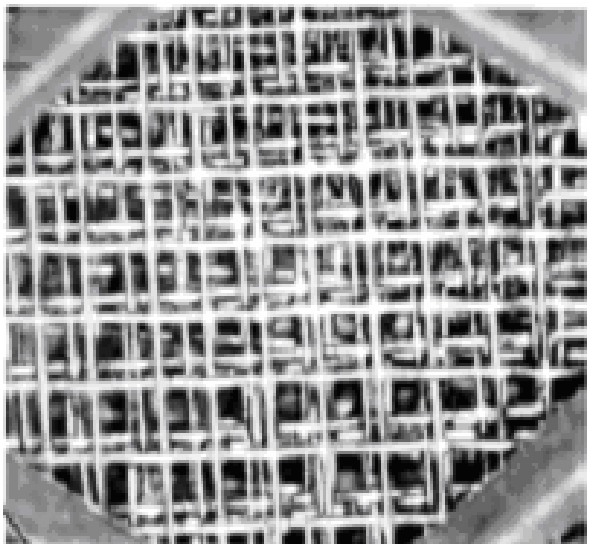

Figure I.6: Example of a wire mesh substrate assembly (reproduced from: www.precision-combustion.com)

I.4.5 Micro-structured Reactor:

Due to the excellent transport rates, improved productivity, temperature control and cost efficiency, micro-channel reactor has been using for the last few decades [70-73]. Recent advances in microfabrication technology offer the low cost replication of microchannel reactor. These can be prepared from various materials: stainless steel [74], glass fiber [75], silicon [76], and polymer [76]. In the simplest form, micro reactor devices consist of a network of micron-sized (typical dimensions are in the range 10 μm – 300 μm) channels etched into a solid substrate. These reactors enable high throughput catalyst screening, micro-sensors and lab-on-chip concepts. Loading of catalyst in this reactor by washcoating and impregnation process is similar to the monolith reactor. Although these reactors are best suited for high-end applications, their high initial costs prohibit the usage for day-to-day applications.

Figure I.7: A microchannel reactor (reproduced from www.hatch.com.au/News_Publications/Energy_Innovation)

I.4.6 Fluidized Bed:

Fluidized bed is one of the major forms of moving bed heterogeneous contacting systems. These reactors consist of fluidized catalyst particles suspended in a moving gas or liquid stream. A fluidized bed reactor has the ability to process large volumes of fluid. Mass and heat transport phenomena, and dispersion of particles of this reactor are explained in details by Kunni et. al. [77]. A schematic diagram of fluidized bed reactor is given below

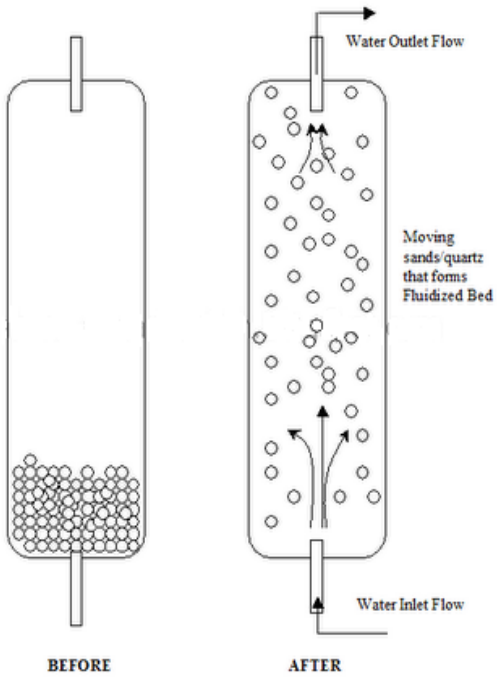

Figure I.8: A schematic diagram of fluidize bed (reproduced from www.allabout-aquariumfish.com)

These are well mixed which results in an even temperature distribution throughout the bed, thus avoiding hot spots. This type of reactor can handle large amounts of feed and solids and has a good temperature control. This reactor can also use smaller particles that reduce transport resistances. The major advantage of fluidized bed reactor is the elimination of reaction runaways that could cause meltdowns and even explosions. Furthermore, catalyst replacement and regeneration for this reactor is more flexible. Nevertheless, due to the expansion of the bed materials in the reactor will increase the reactor size, which thereby causes higher initial capital cost for reactor. Moreover, to fluidize the solid particles in the reactor requires higher fluid velocity, which results in higher energy costs. This high fluid velocity causes entrainment of solid particle into the fluid stream as well as erosion of catalyst particle.

I.5 Criteria to Design Reactor:

Criteria to design a reaction system depend onto the process consideration. In general most reaction systems attempt to achieve following criteria –

1. Increase conversion,
2. Decrease pressure drop,
3. Increase catalyst/sorbent life,
4. Avoid catalyst deactivation,
5. Increase selectivity,
6. Decrease weight of the sorbent or catalyst that is required,
7. Decrease weight and volume of the reactor, etc.

I.6 Factors Affecting Reactor System Performance:

I.6.1 Surface Reaction Rate:

Surface reaction of any catalytic reaction consists of multiple steps – adsorption of reactant onto the catalyst surface, reaction on the surface of the catalyst, and desorption of the products from the surface. When heterogeneous reactions are occurring at a steady state, the rates of the three reaction steps in series are equal to one another. However, one of the above mentioned the steps in the series can be rate determining step of the overall rate of reaction. Surface reaction rate could be of any order depending on the reactant compositions and exact mechanism. Surface reaction rate generally follows Arrhenius rate law [62, 63].

I.6.2 Intra-particle Mass Transfer Rate:

In most fluid solid catalytic reaction systems, catalysts are dispersed onto porous materials of high surface area. Therefore, the reactants diffuse from the pore mouth through the catalyst pores to the immediate vicinity of the internal catalytic surface and similarly products diffuse from the interior of the pellet to the pore mouth at the external surface. Both these two diffusion are considered as internal diffusion. This step can also be rate limiting step and this resistance is modeled using effectiveness factor and Thiele modulus. Effectiveness factor for various types of geometry are explained elsewhere [63].

I.6.3 Fluid-solid Interphase Mass Transfer Rate:

In heterogeneous catalytic reaction, external diffusion involves mass transfer of the reactants from the bulk fluid to the external surface of the catalyst pellets, and mass transfer of products from the external surface to the bulk fluid. These are the key steps and often become the rate controlling steps. Fluid solid interphase mass transfer rate largely depends on the diffusivity and the particle size. There are various correlations available in for estimating fluid phase mass transfer for various system geometries, Re and Sc ranges. Detailed reviews about the mass transfer correlations in packed beds [63, 78] and monoliths are given elsewhere [79, 80].

I.7 Characterization Techniques:

Characterization of a heterogeneous catalyst refers to the measurement of its “characteristics”. Those physical and chemical properties of the catalyst and assumed to be responsible for its performance in a given reaction. In order to understand the kinetics and mechanism of a catalytic/adsorbent reaction, the essential part is catalyst/adsorbent characterization. Catalyst characterization stimulates catalyst development process. It involves

measurements of critical parameters and properties. For characterization of catalyst/adsorbent, varieties of techniques are available. The selection of characterization technique is a vital factor, which certainly depends on the purpose of experiment, and the information provided by the technique. In the literature, different types of catalyst characterization techniques have been described [81, 82].

I.7.1 Particle Size Characterization:

Catalyst powders vary greatly in particle size depending on their origin. Particle size distribution is very important for the consistency of the catalyst performance from batch to batch. The particle size of catalyst/adsorbent particles dictates the intra-particle and fluid-particle interphase transport rates. There are several techniques available for particle size distribution, e.g. sieve analysis, air elutriation analysis, photo-analysis, optical counting methods, electro-resistance counting methods, sedimentation techniques, laser diffraction methods, acoustic spectroscopy, etc. A detail description on these techniques has been discussed elsewhere [82].

The least expensive and least labor intensive technique for separating particles by size is through the use of a conventional sieve. Sieves of various mesh sizes (ASTM D4513-85, 1988) can be used to determine particle size range noting the weight percentage of material that passes through one mesh size but is retained on the next finer screen. Sieves are stacked according to coarsest sieve on the top followed by finer screens. The stack of sieves is vibrated, allowing the finer particle to pass through coarser screens until retained by those screens finer in opening than the particle size of the material of interest. Each fraction is then weighed and a distribution determined. Size of a particle fraction is reported in terms of the mesh sizes between which it is retained or an average particle size of the sieves can be used.

I.7.2 Surface Area Measurement:

Surface area is one of the most fundamentally important properties of a catalyst/adsorbent support as it provides the information of available area for dispersion of impregnated species, and adsorption area for adsorbate molecules. This is an attribute that is used by catalyst manufacturers and users to monitor the activity and stability of catalysts. Measurement of surface area is based on the principles of physical adsorption/desorption of a particular molecular compound on the high surface area materials. The total surface area of a sample is calculated from the area covered by each molecule of the adsorbed materials and the quantity of adsorbed material to form a complete one molecule layer of thickness. There are different methods used to measure surface area and each method can yield different results. Most methods are based on the isothermal adsorption of gas molecules of known sizes. Nitrogen is the most commonly used gas in this case. In this process, gas molecules are condensed onto the unknown sample surface. By completely covering the surface and opening the pores of each particle with a condensed gas, surface area analyzer can characterize the surface. The amount of gas adsorbed and the resultant sample pressure are recorded. This data is subjected to a number of calculations to obtain the surface area. Either a single point or a multipoint method is used to calculate the surface area. In 1938, a widely accepted calculation was developed by Brunauer, Emmett and Teller (BET). A Quantachrome BET surface area measurement was used in this study to measure the total surface area of the high surface area supports and adsorbents.

I.7.3 Chemisorption Technique:

Catalyst/sorbents are reactive on specific surface locations which are known as active sites. Performance of a catalyst/sorbent solely depends on the number of surface active sites. Chemisorption is used primarily to evaluate quantitatively the number of active sites. This technique also reveals the information about surface energy, dispersion of active metal, and the size of the active particles. In chemisorption, the active sites form chemical bonds with certain gases, e.g., H_2, CO, O_2, NH_3, etc., depending on the metal of the catalysts . However, only single layer information can be realized based on these surface active sites. The numbers of active sites are determined by measuring the quantity of the chemisorbed gas. This monolayer volume of a catalyst quantifies the active metal surface area. Furthermore, based on the number of surface active sites metal dispersion can be calculated.

Isothermal chemisorption analyses are performed by two chemisorption technique: static chemisorption and pulse chemisorption. In this study, static chemisorption was employed which is convenient for obtaining isotherm from very low pressure to atmospheric pressure at essentially at temperature from near ambient to 1273 K. The adsorption isotherm is a plot of the quantity of molecule adsorbed by the adsorbent at different relative pressure at a constant temperature.

I.7.4 Pore Size Distribution:

Another fundamentally important property of catalyst support/sorbent is pore volume or pore size distribution. Pore size distribution can be determined either by isothermal gas adsorption porosimetry or by mercury intrusion. In gas adsorption porosimetry, N_2, Ar, CO_2, H_2 or krypton is used which is also based on the physisorption principle. Gas adsorption occurs at different temperatures depending on the nature of the gas. Different analysis techniques are used

to estimate surface area and pore volume of different types of porous material [83]. Gas porosimetry measures pores from 17 Å to about 4,000 Å in diameter (micro-pore and meso-pore range), whereas mercury porosimetry is applicable to pores from 0.006 μm up to 900 μm in diameter (meso-pore and macro-pore range).

In gas porosimetry technique, the amount of gas adsorbed is a function of the interaction between gas and solid (intrinsic), temperature (fixed), and pressure (controlled variable). Gas adsorption will measure pore size by recording isotherms from low pressures to saturation pressure.

I.7.5 Scanning Electron Microscopy:

A scanning electron microscopy (SEM) is a type of electron microscopes that images a sample by scanning it with a beam of electrons in a raster scan pattern. The SEM generates a beam of incident electrons in an electron column above the sample chamber. The electrons are produced by a thermal emission source, such as a heated tungsten filament, or by a field emission cathode. The energy of the incident electrons can be as low as 100 eV or as high as 100 keV depending on the evaluation objectives. The electrons are focused into a small beam by a series of electromagnetic lenses in the SEM column. The energy exchange between the electron beam and the sample results the emission of electrons and electromagnetic radiation, which can be detected to produce images of matter. The type of signals produced by a SEM include secondary electrons, back- scattered electrons, characteristic X-rays, light, specimen current and transmitted electrons. The analytical information that can be obtained from SEM is – image of fine surface morphology, image contrast as a function of elemental composition, surface topography, etc. The SEM images of microfibrous materials were obtained using a JEOL JSM 840 (20 kV) SEM. The

SEM images were recorded at magnification levels of 37 and 200 using an in-built digital camera.

I.7.6 X-ray Diffraction:

In 1913, English physicists Sir W.H. Bragg and his son W.L. Bragg observed a relationship that explained why the cleavage faces of crystals appear to reflect X-ray beams at certain angles of incidence. X-ray diffraction (XRD) is a non-destructive technique having a fast and simple sample preparation method. XRD measures the average spacing between layers or rows of atoms, the orientation of a single crystal or grain, the crystal structure of an unknown material, and the size, shape and internal stress of small crystalline regions.

One of the most important features of XRD is the phase identification. For phase identification, d-spacing is measured from the collected XRD data, and the integrated intensities. Afterwards, the experimental XRD data is compared with the known standards in JCPDS file.

I.7.7 Temperature Programmed Reduction:

Temperature-programmed reduction is a thermo-analytical technique for characterizing heterogeneous catalysts in order to find the most efficient reduction conditions. In this technique, an oxidized catalyst precursor is subjected to a programmed or controlled temperature rise along with a reducing gas mixture flowing over it. In brief, gas containing the reaction educts flows continuously through a small probe in the porous solid materials. At the beginning, the temperature is low, so all reaction rates are virtually zero. Temperature is then increases at a constant rate, so the reaction rate increases depending in the activity and the actual degree of reduction of the materials. This temperature increment continues until the material is completely

reduced. The concentration of the gaseous reaction products or the consumption of the reaction educts is measured. This method yields quantitative information on the reducibility of the oxide's surface, as well as the heterogeneity of the reducible surface. Reaction mechanism and operational details are explained by Lowell et. al [84].

I.8 Reaction Mechanism for Catalytic VOC Decomposition:

A general theory of the mechanism of the heterogeneous catalytic oxidation of low molecular weight vapors at trace concentrations in air does not exist. However, as with many catalytic reactions, certain observations have been consistently made that have led to general hypotheses about how the reaction takes place. The mechanism of complete catalytic oxidation depends on the type of catalyst used. Basically two types of conventional catalysts are used for oxidation reactions: metal oxides and noble metals (supported or unsupported). Both types of catalysts are used for VOC oxidation. Specifically, because oxygen is always present in large excess, the catalyst surface concentration of oxygen is always relatively high. This also means that oxygen concentration in gas phase is essentially constant, and the overall rate will usually be a function of the VOC concentration only.

I.8.1 Langmuir-Hinshelwood Mechanism:

One of the most frequently used approaches to establish rate expression is the Langmuir-Hinshelwood method, which is based on Langmuir adsorption, surface reaction between adsorbed intermediates, and desorption assuming that one of this step is intrinsically slow [63]. Langmuir-Hinshelwood mechanism requires the adsorption of each species at nearby sites and

subsequent reaction and desorption. The rate parameters must be evaluated experimentally for each new catalyst and various external conditions [85] which is shown in Eq. (I.1).

$$(-r_V) = \frac{k_s K_o K_V C_V C_o}{(1+K_o C_o+K_V C_V)^2} \quad \text{(I.1)}$$

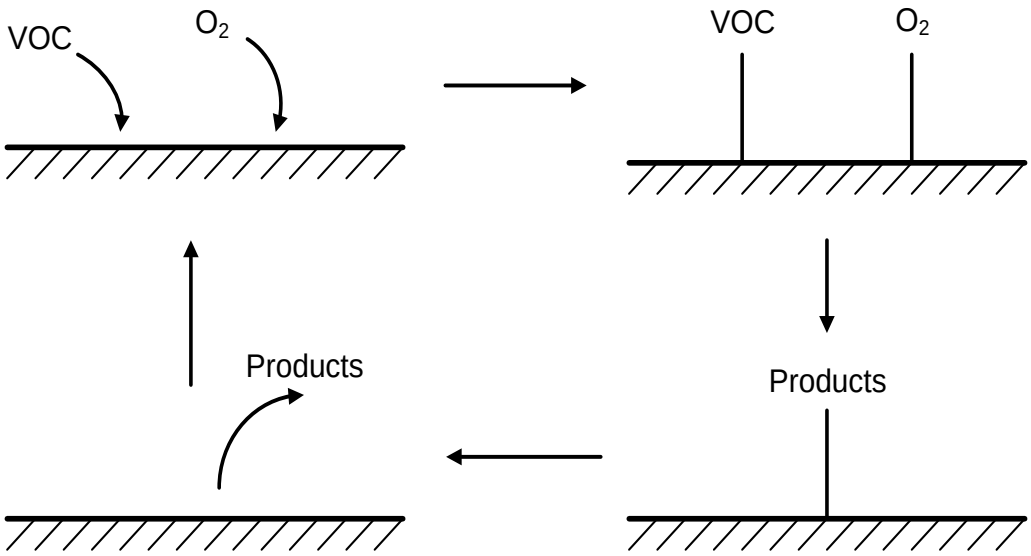

Figure I.9: Langmuir-Hinshelwood mechanism

I.8.2 Eley-Rideal Mechanism:

Gas phase oxygen participates in catalytic oxidation process. Various attempts to explain exactly how the process occurs usually include a redox cycle at the oxide surface with anionic oxygen from the surface (either chemisorbed or lattice oxygen) reacting with a chemisorbed or gas phase reactant. When the reactant is oxidized directly in the gas phase by an adsorbed oxygen species, is called Eley-Rideal mechanism, which was proposed by D.D. Eley and E.K. Rideal in 1938 [86]. For metal or nonreducible oxide catalysts, excess oxygen in the gas phase

means that the catalyst surface is well-covered with oxygen and that little if any VOC is adsorbed. Thus, the Eley-Rideal mechanism is expected to be important.

$$(-r_V) = \frac{k_s K_o C_V C_o}{1+K_V C_V} \quad \text{(I.2)}$$

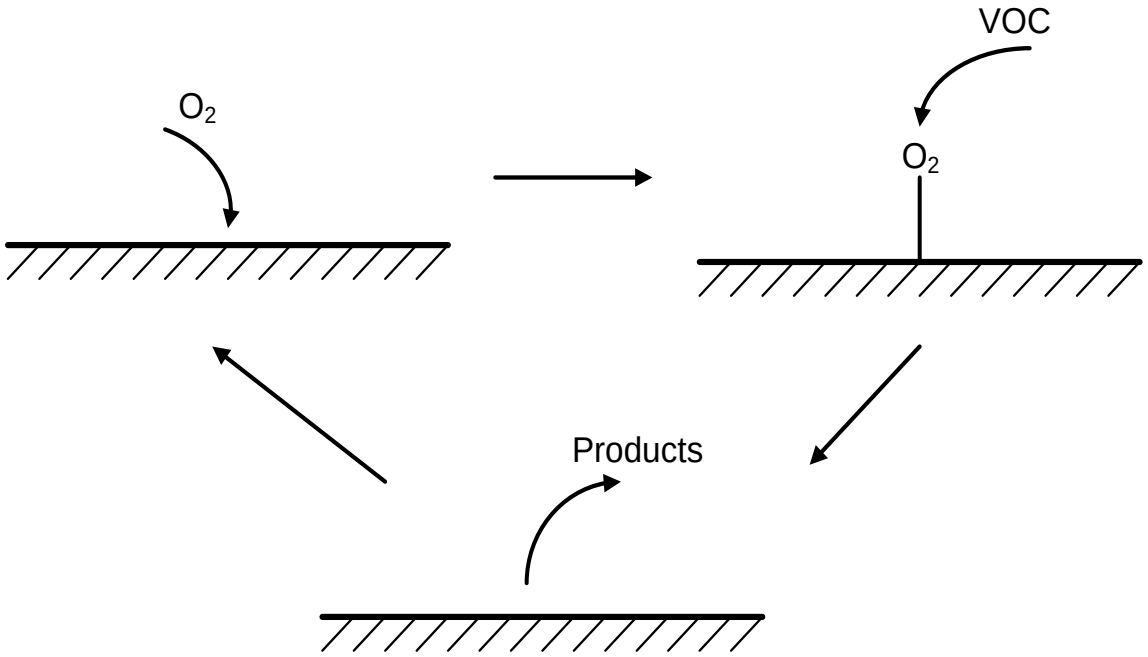

Figure I.10: Eley-Rideal mechanism

I.8.3 Mars-Van Krevelen Mechanism:

In 1954, P. Mars and D.W. Krevelen proposed a two-stage redox model for VOC oxidation on noble metal and metal oxides catalysts [87]. This mechanism explicitly requires a redox process in which oxygen is consumed from the catalyst surface by reaction with the VOC and then is replenished by oxygen from the vapor phase. This model postulates two redox steps:

a) Reduction of the oxidized catalyst by the VOC (V):

$$Cat - O + V \overset{k_V}{\rightarrow} Cat + CO_2$$

b) Oxidation of the catalyst by oxygen from the gas phase:

$$2Cat + \upsilon O_2 \overset{k_o}{\rightarrow} 2Cat - O$$

In this steady state operation, the rates oxidation and reduction steps must be equal considering the overall stoichiometry of the reaction (υ). The Mars-Van Krevelen model is the most frequently reported model for the catalytic combustion of VOC [56, 57, 88, 89]. For metal oxides containing readily reducible metals, this scheme is important. According to this model, the reaction rate is expressed by Eq.(I.3).

$$(-r_V) = \frac{k_s k_V k_o C_V C_o}{k_o C_o + \upsilon k_V C_V} \qquad \text{(I.3)}$$

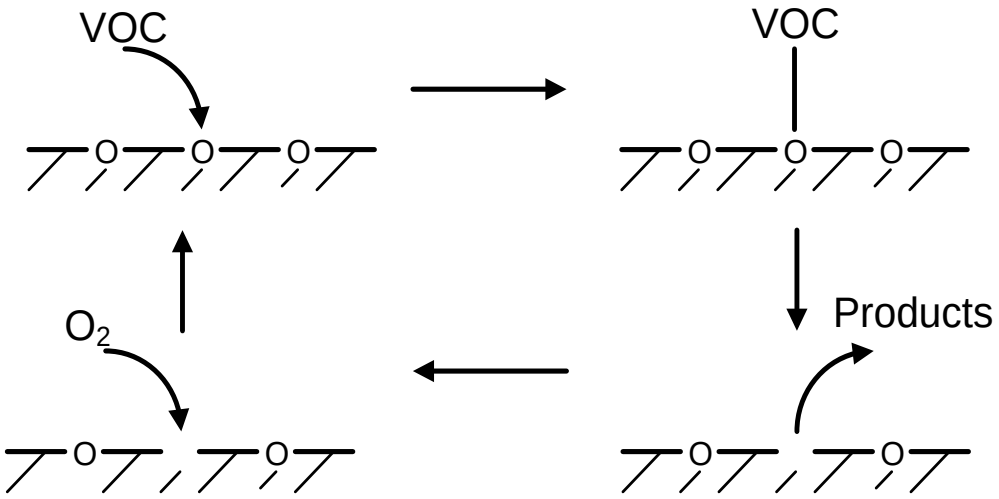

Figure I.11: Mars-Van Krevelen mechanism

I.9 Pressure Drop Model:

Transport phenomena in a porous medium arise in many fields of science and engineering. In the past several decades, flow in porous media has studied both experimentally and theoretically. Flow in porous media usually involves three scales: the pore scale, the representative elementary volume (REV) scale, and the domain scale. The REV is defined as a minimum element at which scale characteristics of a porous flow holds. The REV scale is much

larger than the pore scale but is much smaller than the domain scale. In classical studies, a flow in porous media is usually modeled by semi empirical models due to the complex structure of a porous medium based on the volume-averaging at the REV scale. Due to the complexity of the flows in porous media, analytical solutions are difficult to obtain except for very few problems. For general cases, only approximate solutions can be obtained numerically. Many numerical simulations have been conducted in the past using common schemes based on discretization of the semi empirical models [90, 91].

I.9.1 Darcy's Law:

In 1856, French hydraulic engineer Henry Darcy published an equation for a flow through porous media [92]. It relates the volumetric flow rate and induced pressure difference in a flow channel which states that the force required moving a fluid through a porous media is directly proportional to the media thickness (L), the superficial velocity through the media (v_o), and the permeability constant of the media (K_m). Equation (1) shows the general form of Darcy's law.

$$\Delta(P + \rho g h) = \frac{\mu L}{K_m} v_o \tag{I.4}$$

The forces acting on the fluid are pressure (P) and a potential force, which is created on a height of fluid (h) by the acceleration of gravity (g). The viscosity and density is denoted by μ and ρ respectively. The term $\mu L/K_m$ is known as the Darcy's constant. For gases at very low and very high velocities the Darcy's law linear relationship is invalid [93]. The reason behind this deviation is that for very high gas velocities, Darcy's law neglects the inertial effects of the flow,

and for very low velocities, fluid flow no longer induced by the pressure difference but by molecular diffusion and streaming.

I.9.2 Ergun Equation:

There are several approaches for measuring pressure drop of fluid flow through a packed bed. The most successful is the Ergun Equation, which describes flow in both the laminar and turbulent regimes. The Ergun equation, derived by the Turkish chemical engineer Sabri Ergun in 1952, is commonly used to calculate the pressure drop through catalyst packed beds, where friction factor is expressed as a function of the Reynolds number [94]. This equation assumes the packed column as a compact irregular bundle of tubes. Darcy's law can describe the general behavior of viscous flow through a homogeneous porous medium. In order to estimate the pressure drop across a porous medium, it is assumed that the general porous media is an assembly of channels of various cross sections with a fixed length. The viscous energy loss at low gas flow rates is given by the Blake (1922) [95] and Kozeny theory (1927) [96]. In Kozeny's theory the hydraulic radius of the porous media is inserted into the Hagen-Poiseuille formula for laminar flow inside a pipe. When the gas flow rate increases, the effect of inertia becomes prominent. The theory of Burke and Plummer (1928) [97] describes the kinetic energy loss at high flow rates. For highly turbulent flow in tubes with any appreciable roughness, the friction factor is a function of the roughness only, and is independent of the Reynolds number. The general expression of the pressure drop for flow through a fixed bed, as suggested by Reynolds, may be presented as the sum of viscous and inertial contributions. The Ergun equation incorporates these two contributions in a semi empirical form [98-100].

$$\frac{\Delta P}{L} = 150\frac{\mu(1-\varepsilon)^2 v_o}{\varepsilon^3 D_p^2} + 1.75\frac{(1-\varepsilon)\rho v_o^2}{\varepsilon^3 D_p} \quad \text{(I.5)}$$

Although there have been arguments that the coefficients in the Ergun equation are not constants, these depend on the Reynolds number, porosity, and particle shape [101, 102]. Furthermore, this equation is only applicable for media having porosity less than 0.5 and performs well for uniformly sized particles.

I.9.3 Brinkman Equation:

An alternative to Darcy's law is Brinkman's equation. In 1949, Henri Coenraad Brinkman omitted the inertial term from Darcy's Equation and replaced by a term, which is analogous to the Laplacian term that appears in the Navier-Stokes equation [103, 104]. This term raises the order of the interior equation to permit application of the continuity of velocity and stress boundary conditions. This equation introduces a correction to Darcy's law to account for viscous shear effects and the changes in viscosity that arises due to the introduction of the solid porous matrix. The application of this equation for porous media has been discussed elsewhere [105]. Durlofsky et. al [106] has shown that this equation described accurately the flow in porous media for volume fraction below 0.05.

$$\frac{\Delta P}{L} = 18\frac{1-\varepsilon}{\varepsilon^2}\left[1 + 2.75\left(\frac{1-\varepsilon}{\varepsilon}\right)\right]\frac{\mu v}{D^2} + 0.69\frac{1-\varepsilon}{\varepsilon^4}\frac{\rho v^2}{D} \quad \text{(I.6)}$$

I.9.4 Forchheimer-Extended Darcy:

In 1901, Forchheimer generalized Darcy's law in a nonlinear fashion. High operational velocities through porous media often resulted in non-linear deviations from Darcy's law due to

inertial effects on the flow of a Newtonian fluid in rigid porous media [107]. Therefore, the modified equation includes an extension term for pressure changes in terms of second power of velocity. Mathematical technique of two scale homogenization has been exploited to derive this model from the Navier-Stokes equation [108-110]. This model is also known as Hazen-Dupuit-Darcy model.

$$\frac{\Delta P}{L} = \frac{\mu}{\alpha} v + \frac{\rho c_F}{\alpha^{1/2}} v^2 \qquad \text{(I.7)}$$

Where α is the porous media permeability and c_F is the Forchheimer or inertia coefficient. This model fails unexpectedly when the fluid has temperature-dependent viscosity and when the flow channel is heated or cooled. Historically the model has been derived from experiments conducted under isothermal flow condition. However, Narasimhan and Lage [111] has shown the limitations of this model.

I.10 Computational Fluid Dynamics:

Computational Fluid Dynamics (CFD) is becoming a critical part of the design process for more and more companies. CFD is structured on the fundamental governing equations of fluid dynamics – the continuity, momentum and energy equations. CFD mainly deals with the numerical solution of the mass and momentum (Navier-Stokes) equations for problems involving fluid flow [112-114]. Moreover, heat and mass transfer conservation equations can also be integrated into the CFD algorithm in order to find solutions for problems involving heat transport, mass transport and reactions. The simulation software predicts not only the fluid flow behavior, but also the transfer of heat, mass, phase change, chemical reaction, mechanical movement, and stress or deformation of related solid structures.

The role of CFD in preliminary design has a corollary in basic research. Assuming that a given CFD solution to a basic flow contains all of the important physics, and then this CFD solution is a numerical tool. In turn, this numerical tool can be used to carry out *numerical* experiments to help study the fundamental characteristics of the flow. These numerical experiments are directly analogous to actual laboratory experiments. Most chemical processes involve reaction, heat transfer, loss transfer and heat generation in fluid flow. Fluid flows involved in these process units are very complex and difficult to measure, and often heat and mass transfer occurs between multiphase flows. Trouble-shooting as well as developments in process efficiency requires solution to dependent variables at multiple data points in the fluid flow field and time, which are often unavailable. Given these experimental difficulties, CFD methods can prove to be powerful design and analysis tools for chemical engineering applications. It can be applied to examine the influence of various parameters on flow behavior in different equipment designs, or to compare performance of a given design under different operating conditions. It conveniently allows for examining various concepts in a virtual setting, without actually building a physical model. Scale up related issues can also be easily eliminated as process equipment at its full-scale can be analyzed using CFD.

CFD which is mainly originated in the aerospace industry is a powerful design tool to model the complex flow around moving objects [113]. The usage of the present day CFD is not confined to design fluid flow anymore; this tool has spread into almost every application which involves fluid flow. As CFD can handle heat and mass transport of the species, recently its application has extended in chemical process like combustion, mixing, catalytic reaction, etc [115-121] . All these above references are the examples of CFD application in chemical processes. Calis et. al [115] have applied CFD to estimate pressure drop across the novel

structured packed bed. Nijemeisland et. al and Dixon et. al [116-118] have used CFD to determine optimum catalytic design for steam reforming application. Duggirala et. al [38] has applied CFD to predict pressure drop in microfibours porous media. In this study, CFD is used to analyze the pressure drop and velocity profile across pleated MFEC.

I.10.1 Discretization Technique:

The efficient and reliable solution of the algebraic equations systems that arise from the discretization of partial differential equations (PDEs) lies at the heart of almost all CFD software. CFD involves discretization of partial differential equations and solving them numerically. It is mainly applied to problems where it is difficult to find an exact solution to the partial differential equations describing the problem. The principle idea of CFD methods is to replace a governing equation by an equivalent and approximate set of algebraic equations. The various methods of discretization and solution of numerical equations used in CFD are described in detail elsewhere [112-114, 122, 123]. There are mainly three methods used for discretization technique:

1. Finite difference method (FDM)
2. Finite element method (FEM)
3. Finite volume method (FVM)

In finite difference method, this is the oldest discretization technique; each derivative of PDE is replaced by an equivalent finite difference approximation. In this method, governing equations are discretized only at selected points in the domain. These points are called nodes and the solution obtained only at these points, the solution between the nodes is interpolated by simply connecting the nodes with straight lines. This basis of a FDM is the Taylor series expansion of a function. To develop finite difference expressions for the various partial

derivatives, Taylor series expansions are used and depending on the required level order of accuracy corresponding higher term in Taylor series are neglected. These discretized finite difference equations are solved using any of the various implicit or explicit methods to obtain solution at various locations in the domain called nodes. The boundary conditions for a given problem dictate the solution, and therefore the proper treatment of boundary conditions within the framework of a particular finite-difference technique is vitally important. The numerical solution provided by this technique, usually contains two kinds of errors: discretization error and round-off error.

Finite element method (FEM) is a numerical method for solving a differential or integral equation. It has been applied to a number of physical problems, where the governing differential equations are available. The method essentially consists of assuming the piecewise continuous function for the solution and obtaining the parameters of the functions in a manner that reduces the error in the solution. In the FEM, a distributed physical system to be analyzed is divided into a number (often large) of discrete elements. The complete system may be complex and irregularly shaped, but the individual elements are easy to analyze. Two popular FEM formulations are Galerkin formulation and Ritz formulation. In Galerkin formulation, the primary variable is approximated by a continuous function inside the element. In Ritz formulation, the differential equation is converted into an integral form using calculus of variation [124].

In FVM, the governing equations are discretized and solved at selected regions in the domain called volumes [122]. "Finite volume" refers to the small volumes surrounding each node point on a mesh. The distributions of each of the flow variables inside the control volumes can be constant, linear or higher order variations. This method uses the integral form of the

conservation equations. In this method, the divergence theorem is employed to convert volume integrals in the partial differential equations that contain a divergence term to surface integrals. This method unlike the FDM does not require structured grids for its solution. It is widely used in many computational fluid dynamics packages.

I.10.2 Turbulence Flow Model:

Turbulent flows are characterized by fluctuating velocity fields. These velocity fluctuations mix transported quantities such as momentum, energy, and species concentration, and that cause the transported quantities to fluctuate as well. ANSYS FLUENT provides the following turbulence models: *Spalart-Allmaras* model, *k-ϵ* models, *k-ω* models, Transition *k-kl-ω* model, Transition *SST* model, v^2-*f* model, Reynolds stress models, Detached Eddy Simulation (DES) model, and Large Eddy Simulation (LES) model. The choice of turbulence model depends on the physics encompassed in the flow, the established practice for a specific class of problem, the level of accuracy required, the available computational resources, and the time available for the simulation. To make an appropriate choice, it is necessary to understand the capabilities and limitations of the various options.

The standard k-ϵ model, the simplest "complete model" of turbulence, are the two equation model in which the solution of two separate transport equations allows the turbulent velocity and length scales to be determined independently. The standard *k-ϵ* model [125] is a semi-empirical model based on model transport equations for turbulent kinetic energy and its dissipation rate. The model transport equation for kinetic energy is derived from the exact equation, while the model transport equation for dissipation rate was obtained using physical

reasoning and bears little resemblance to its mathematically exact counterpart. The assumptions for this model are fully turbulent flow and negligible effects of molecular viscosity.

The shear stress transport (SST) k-ω model was developed by Menter to effectively blend the robust and accurate formulation of the k-ω model in the near-wall region with the free-stream independence of the k-ϵ model in the far field. To achieve this, the k-ϵ model is converted into a k-ω formulation. The standard k-ω model and the transformed k-ϵ model are both multiplied by a blending function and both models are added together. The blending function is designed to be one in the near-wall region, which activates the standard k-ω model, and zero away from the surface, which activates the transformed k-ϵ model. The SST model incorporates a damped cross-diffusion derivative term in the ω equation.

I.10.3 Porous Media Model:

Porous media model can be used for a wide variety of single phase and multiphase problems, including flow through packed beds, filter media, perforated plates, flow distributors, and tube banks. The porous media model incorporates an empirically determined flow resistance in a “porous” region. In essence porous media is nothing more than an added momentum sink in the governing equations that has two parts: a viscous loss term, and an inertial loss term. The viscous and inertial resistance coefficients are generally based on the superficial velocity of the fluid in the porous media. This momentum sink contributes to the pressure gradient in the porous cell, creating a pressure drop that is proportional to the fluid velocity in the cell. To suppress the effect of turbulence in a porous region, it is necessary to set the turbulent contribution to be viscosity equal to zero. Therefore, the effect of transported inlet turbulence quantities through the media on fluid mixing, and momentum is ignored. Furthermore, there is no generation of

turbulence inside the media. Pressure drop modeling across porous media relies on the orientation to the flow directions [126-131]. Moreover, PRESTO is the preferable pressure interpolation scheme than second order scheme.

I.10.4 Limitation of CFD:

Like other techniques, CFD has certain limitations. CFD solutions rely upon physical models of real world processes e.g. turbulence, compressibility, chemistry, multiphase flow, etc. And therefore, the solutions can be as accurate as the physical models on which they are based. Also, representing some of exact physics of the real world flows with precision can become computationally expensive. Direct numerical simulation of turbulent flow, modeling of multiphase flows and solution of reactive flows with multiple reactions running in series and parallel, are the possible examples of this [132]. For turbulent fluid motion, the complication is that it requires a spatial grid that needs to be fine enough to capture smallest length scales throughout the domain. Therefore, extensive computational sources are required even for slightest complexity. This is overcome in most commercial software by using time averaged equations and modeling the resulting turbulent correlation terms. This and a variety of other turbulence models are also available but they can lead to significant inaccuracies under certain circumstances and the user needs to be cautious in applying them.

The sources of error can be from numerical errors which are caused by the finite difference approximations, and modeling errors where the true physics is not known or is too complex to model. Furthermore, unknown boundary conditions, such as inlet pressure or temperature profiles, can cause erroneous result. In addition, unknown geometry such as tip clearances or leading edge shapes, and assumption of steady state flow, can be potential sources

of errors. Numerical errors arise from the finite difference approximations that are inevitable in any numerical method. Therefore, the results obtained using CFD cannot be trusted unless the error calculations are done. A detailed account of the convergence, code verification and error estimation is presented elsewhere [112-114]. In spite of these inherent drawbacks, the results of CFD are amazingly accurate for a very large number of applications.

Chapter II

Fiber selection & Optimum Structural Design

II.1 Introduction:

Current engineering practice often uses sintered or fused grains of microscopic materials in order to produce high surface area that facilitates the chemical process. Auburn University have taken an attempt that led to the discovery of “second generation” materials, which further capitalize on the exciting structure-property foundation relationships of microfibrous materials by entrapping small grains of catalyst, electro-catalyst, bio-support, and/or sorbent within the small pore structure of the fibrous network. A detail description of this material has been provided in Section I.2. As stated before, the aim of this project is to establish a “small and light weight” MFEC configuration which will have improved performance in terms of pressure drop and catalytic activity at high face velocities than the commercial monolith which are originally intended for this condition.

Pressure drop is an extremely important criterion for reactor and filter designs. It should be checked at the early stage in the design with the purpose of assessment its influence. Fiber dimension plays a vital role in pressure drop at a certain fluid velocity across a reactor. Karwa et al. [133] has investigated the effect of fiber dimension on the pressure drop across fibrous media at low fluid velocity. Furthermore, multi-element structural array has shown a strong influence on pressure drop across a pleated filter [134]. Sothen et al. [134] provides an innovative idea of utilizing the housing in order to achieve maximum removal efficiency having low pressure drop across the filters. Based on these previous researches, the foremost steps of this project were to select the fiber dimension of the MFEC and to construct a multi-element structured array in order

to achieve low pressure drop across the reactor as well as high face velocity in the system. The results of these steps will assist to proceed for further investigation.

II.2 Experimental Details:

II.2.1 Materials:

Nickel fibers of metal purity (>99%, Ni-200) with nominal diameter of 4 μm, 8 μm and 12 μm, and length of 3 mm to 6 mm were obtained from IntraMicron, Inc., AL. These fibers are ribbon-shaped. A blotter paper made of a mixture of hardwood and softwood cellulose fibers was used. Air, hydrogen and nitrogen used in this experiment, were obtained from Airgas Inc.

II.2.2 Media Preparation:

Microfibrous entrapped catalyst was prepared by the old-fashioned wet lay paper making technique. 13.5 g of nickel fibers and 2.7 g of cellulose were dispersed in high viscosity water. The viscosity of the water was modified by the addition of 0.8% (w/w) hydroxy ethyl cellulose (HEC) followed by hydrolysis of HEC at pH~10 using sodium hydroxide. After the addition of the fibers and cellulose to the modified water, the mixture was stirred in a blunt propeller to disperse the fibers. To ensure proper dispersion of the fibers, initially the stirring was done at low RPM when most of the fibers were dispersed, and the mixture was then stirred at high RPM to disperse the few nickel fibers still in bundles. The viscosity modifier of water and two stage-mixing helped to disperse the fibers without excessive reduction in their aspect ratio. The dispersion of fibers and cellulose were then placed on the 20.32 cm × 20.32 cm hand sheet former. The suspension was stirred vigorously. The excess water inside the sheet was drained,

and thereby, the preform of MFEC was formed. Cellulose acts as a binder for the nickel fibers that provide wet and dry strength to the preform due to the hydrogen bonding between cellulose fibers. The preform was then dried at 373 K for 2 h. Afterwards, this perform was oxidized at 723 K where most of the cellulose disappeared. At this stage, the media required extra care for handling as it contained fibers only. Subsequently, the media was sintered at 1173 K for 40 min using hydrogen. In this stage, fibers were bonded to each other and prepared a sinter-locked structure. Thus MFEC was prepared. To have the same thickness for all MFEC sheets, a hydraulic press was used to compress the samples. The samples were placed between two 25.4 cm × 25.4 cm × 0.15 cm tight thickness tolerance steel plates with washers used as spacers to define the final thickness of the nickel MFECs. The final thickness of MFEC was measured accurately at 1 kPa.

II.2.3 High Volumetric Test Rig:

Lab scale and schematic diagram of the high volumetric test rig are depicted by Figs.II.1 and II.2. The test set up consists of a high pressure radial blower of 40 hp (Fan Equipment Company Inc.). The blower has a maximum frequency of 60 Hz and temperature of 481 K. The radial blower withdraws air from atmosphere. The system is a closed recycle loop made up by stainless steel tube of 1 mm thickness. The whole system consists of two different dimensional tubes – 200 mm (top section) and 150 mm (bottom section). Therefore, cones are used at the transition point of large and small diameter sections. Fragments of each section are connected with one another by pull ring. All joints are sealed with U-shaped silicon gasket. Pull ring along with the gasket produce no noticeable leaks. The closed recycle loop generates heat by frictional loss. The whole system is well insulated by glass wool to reduce heat loss. Ring heaters are used

as additional heating supply. These additional heaters stimulate the temperature increment process at high face velocity and provide required heat to obtain desired temperature at low face velocity. Heaters as well as purging air are used to control the system temperature, which can be raised to as high as 473 K. Purging air is controlled by an exhaust valve. The temperatures at various points of the system are measured by J-type thermocouples (Omega). A variable speed drive is used to control the system speed. Information of the system speed is acquired by the differential pressure gauge across a bare section of the test rig, which is verified by pitot tube and blower pressure curve.

Main reactor section, which is constructed by stainless steel, has a dimension of 12.7 cm × 12.7 cm × 23 cm as shown in Fig.II.3 and Fig.II.4. As the cross section of the remaining parts of the test rig is circular, two “square to round” connectors are used between the reactor and rest of the rig. Each of the connectors is 33 cm long. Reactor is fastened by nut and bolt fixtures with the auxiliary connectors. Super-resilient silicon foam of 0.9525 cm thickness is placed between to these two sections to avoid leakage.

Figure II.1: High volumetric test recycle loop

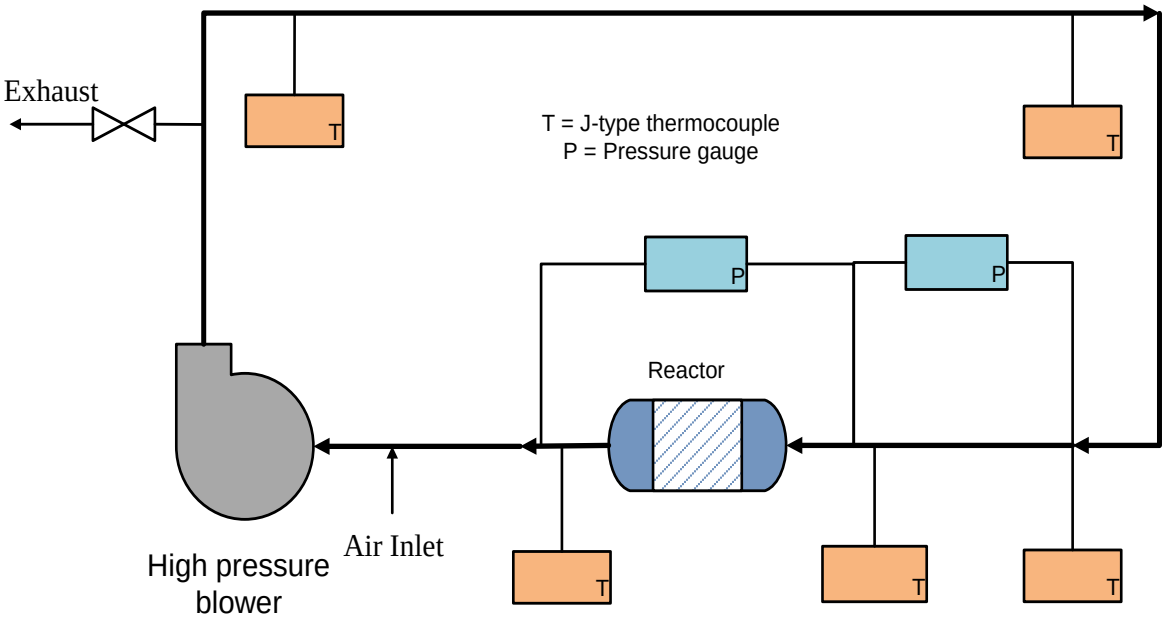

Figure II.2: Schematic diagram of the experimental set up

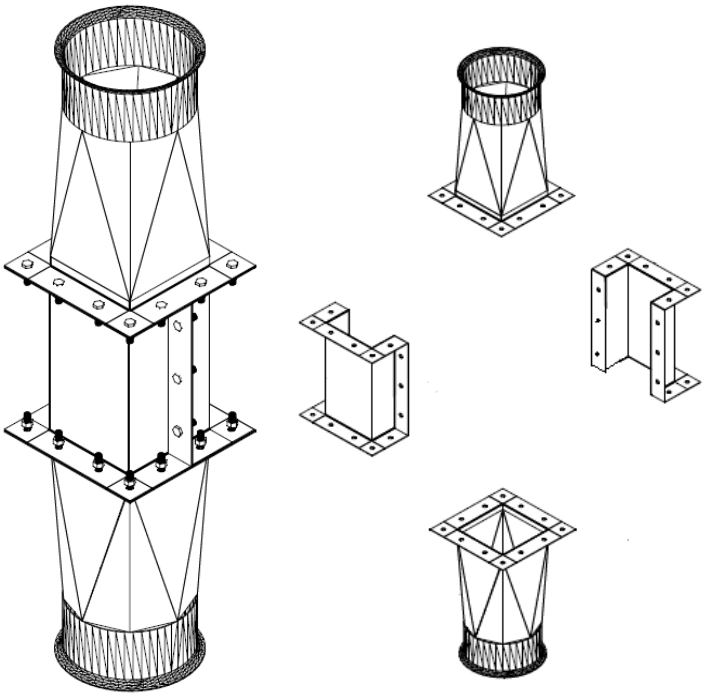

Figure II.3: Mechanical drawing of the reactor section

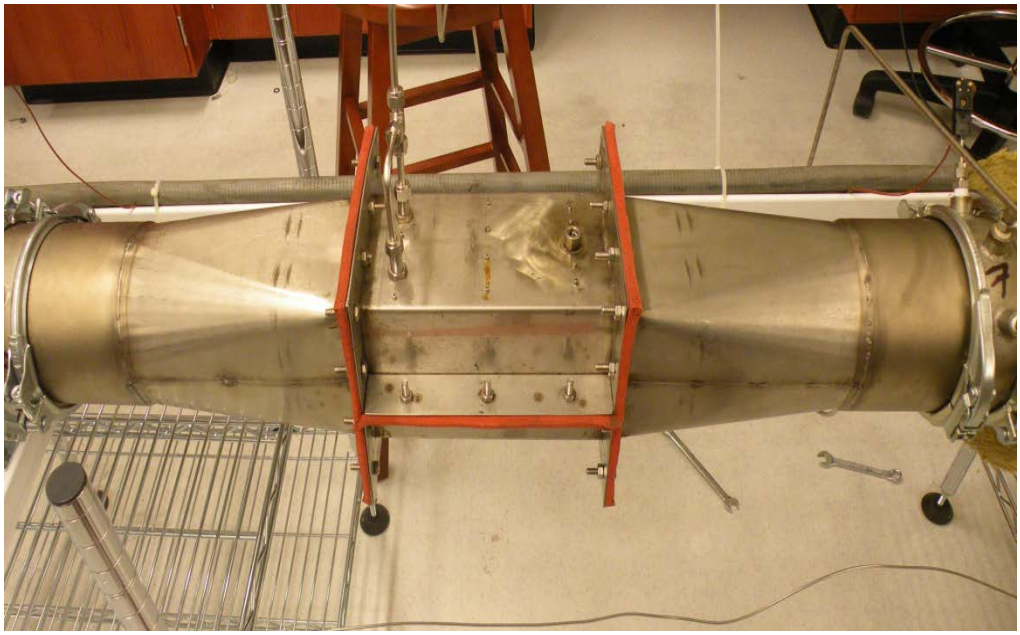

Figure II.4: Reactor section

II.2.4 Formation of Multi-elemental Structured Array:

MFECs that have been formed in section II.2.2 are placed in the reactor in different elemental structured formation. In this study, three different configurations have been used – Flat, V, and W, which correspond to numbers of pleat 1, 2, and 4, respectively. Due to the constriction of space, the numbers of pleat have been limited to 4. Fig.II.5 shows the schematic diagram of these three structures. As the system speed is very high, the media are placed between expanded metal sheet (SS) and corrosion resistant woven wire cloth, as a “sandwich” format. These protective metal sheets ensure the sustainability of the media at high face velocity.

For constructing V and W shapes, the sandwiched materials are placed in aluminum U-channel of 1.905 cm base. Fig. II.6 shows the W-shaped structure. The edges and the space between the media and U-channels are sealed by silicon sealant to eliminate all leakage in the structure. The structural array is placed in the square section well sealed by silicon sealant and silicon foam.

Flat Structure

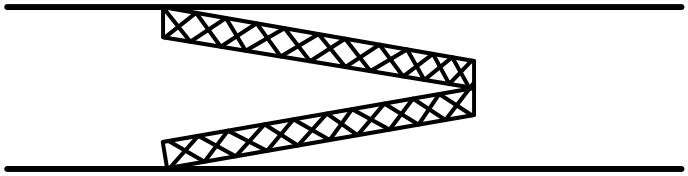

V-Structure

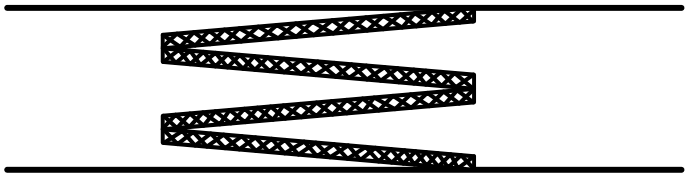

W-Structure

Figure II.5: Multi-elemental structured arrays that have been tested

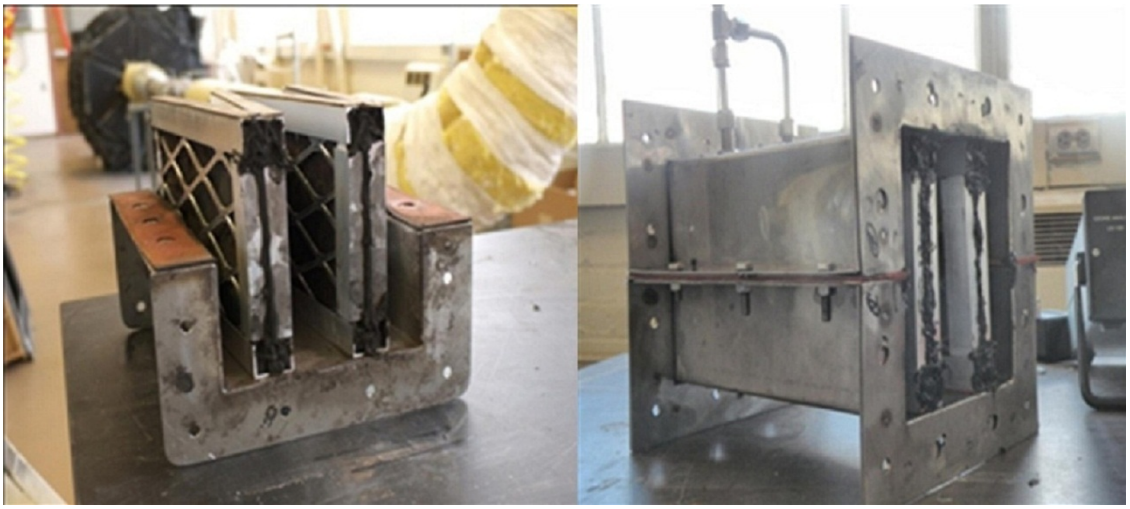

Figure II.6: MFEC VOC converter (W-shaped structure)

II.3 Flow Mechanism in Multi-elemental Structured Array:

Air flows through the accessible areas of the permeable media placed between the U-channel. Fig.II.7 shows the flow direction through the structures. The upstream flow is assumed to be uniform. The air velocity increases at the front of the reactor due to the contraction created by the edges of the structural array i.e. V and W. The air is channeled around the edge and diverges as it reaches the face of the media. While the air approaches the media face, it is channeled around the inlet facing mesh screen. In the media, the air is assumed to flow in an identical path for all the elements of the structure. The flow is contracted due to the pleat tip blockage. The air travels through the media and converges as it exits from the media and enters into the downstream array. The exit from the reactor causes a further increase in area and velocity decreases. The air finally uniformly redistributes in the downstream duct.

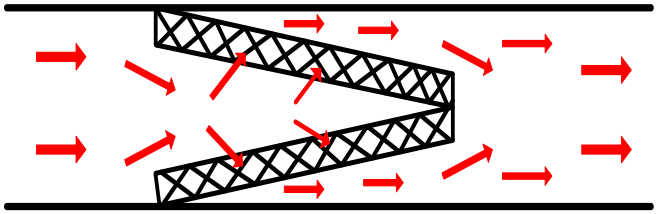

Flow through V-structure

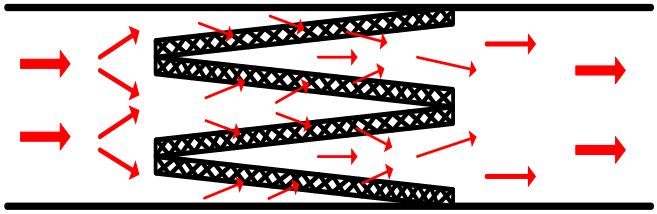

Flow through W-structure

Figure II.7: Fluid flow direction in V- shaped and in W- shaped structures

II.4 Results and Discussion:

II.4.1 Effects of Fiber Dimension:

Fig.II.8 shows the effect of fiber dimension on the pressure drop across the reactor. As evident from the plot, as the fiber dimension decreases, pressure drop across the reactor increases. Instead of proceeding towards further complicated structure, i.e. V or W, these experiments have been conducted on flat structure. According to this figure, pressure drop followed a quadratic relation with face velocity where the relationship includes viscous loss and inertial loss. For a certain temperature, this relation follows similar trend for all dimensional fiber. However, at a certain face velocity, pressure drop for small dimensional fiber media is higher than that for large dimensional fiber media. According to the pressure drop models mentioned in section I.8, pressure drop is inversely related to the diameter of the object that is

placed in fluid flow. Small dimensional fiber enhances the viscous loss and the inertial loss at a certain fluid velocity which intensifies the pressure drop across the media as well. Furthermore, this plot provides the information of maximum obtainable face velocity by a certain dimensional fiber MFEC. The result inferred that larger dimensional fiber was able to achieve higher face velocity than the smaller dimensional fiber. Therefore, media prepared by 12 μm Ni fiber should be preferable for media preparation. However, during media preparation, 12 μm Ni fibers were not able to provide well dispersed media. It formed fiber bundles in media followed by a non-uniform structure and enhanced higher particle loss from the media as shown in Fig.II.9. Hence, according to the result and above discussions, 8 μm Ni fibers are well-suited for the media preparation which can be used for further experiment.

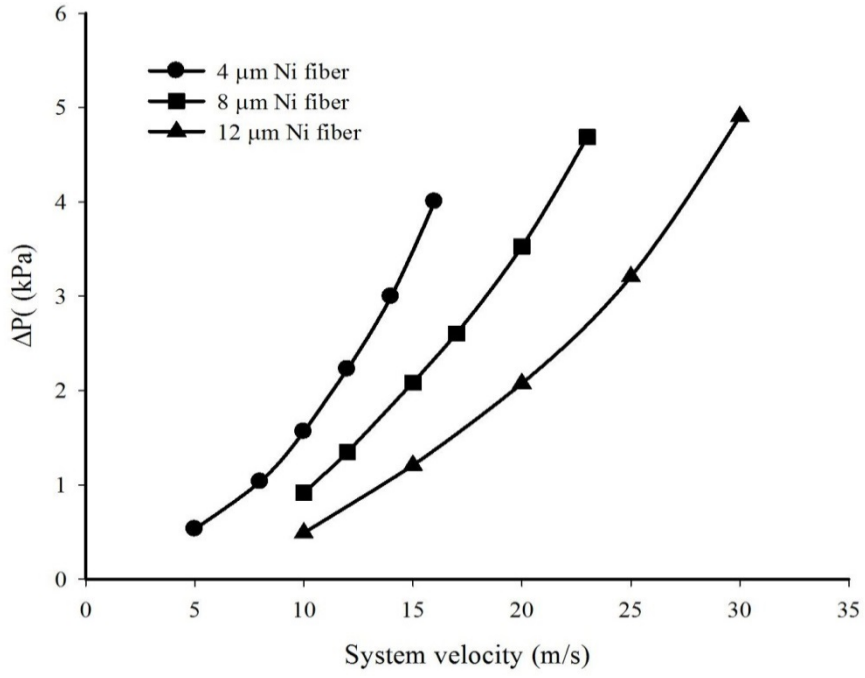

Figure II.8: Effect of fiber dimension on pressure drop versus system velocity for flat structure (T = 423 K)

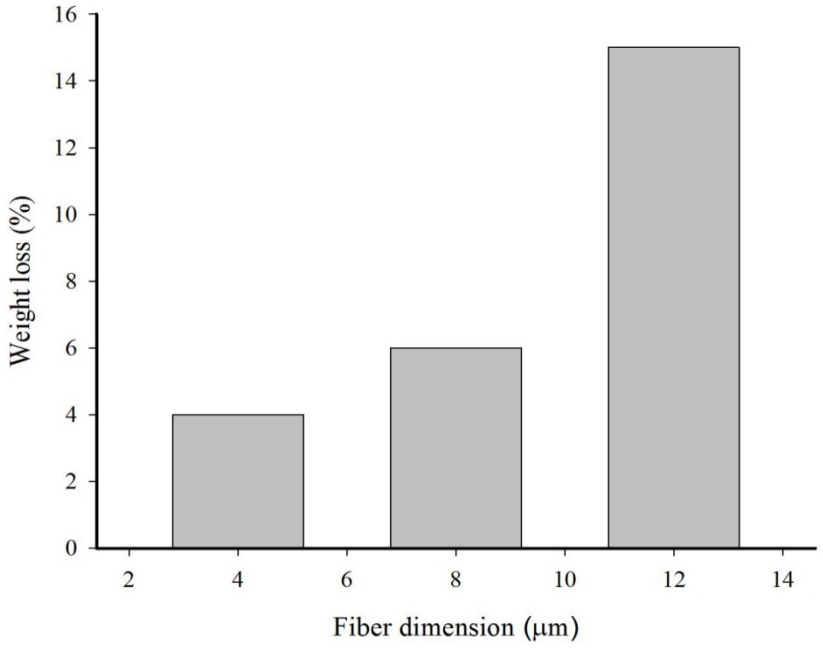

Figure II.9: Percentage of particle loss from different dimensional fiber MFEC

II.4.2 Effects of Multi-element Structured Array:

Fig.II.10 shows the effect of different pleated structures on the pressure drop that occurred in MFEC at various face velocities. In each experiment, the system temperature, the fiber dimension, the fiber loading in each sheet, and the thickness of the sheet were maintained at 473 K, 8 μm, 13.5 g, and 2.1 mm, respectively. The only change was the pleat numbers, i.e., 1, 2, and 4. The system was operated at 95% frequency of the maximum frequency for operational safety. As evident from the plot, the pleat number significantly affected the pressure drop and the system velocity. The W-shaped structure exhibited the lowest pressure drop for a fixed face velocity than other structures and resulted the maximum achievable velocity by the system. These results can be attributed to the reduction of the face velocities by the pleated MFEC. The velocity was reduced by the pleat factor (*PF*) term [32] as shown in Eq. (II.1). The pleat number

for MFEC could be increased by more than 4, but with further increase in pleating the inertial losses of pressure drop would increase drastically, which could in return negate the advantages of pleating.

$$PF = \frac{Total\ face\ area\ of\ MFEC\ media}{Total\ cross\ sectional\ area\ of\ the\ reactor} \quad \text{(II.1)}$$

This substantial reduction in velocity allows a structure to essentially eliminate or considerably hinder the effect of face velocity, media thickness, and media constants. This attributed to the reduction in pressure drop as pressure drop follows a quadratic relation with face velocity. Although slot resistances created by the other two structures are lower than that of W-structure, other fixed resistances were so large that minor difference in slot resistances was not able to compensate. Moreover, the slot resistance was not significantly high due to the width of the U-channel. Furthermore, W structure provides available fluid flow area more than the other two structures. Due to the dimensional limitation of the reactor section, more than 4 elemental arrays were not able to be placed.

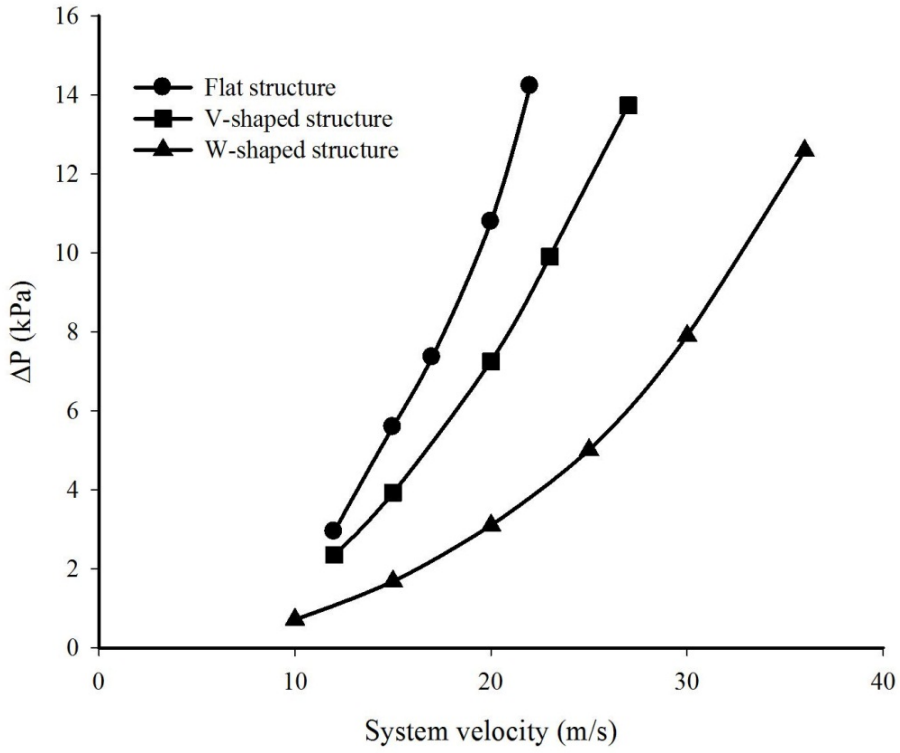

Figure II.10: Pressure drop versus system velocity for different pleated structures having same media thickness (T = 473 K)

The results shown in Figs. II.8 and II.10 indicate that the MFEC with optimum fiber dimension and optimum pleat number tended to benefit the most from low pressure drops and high system velocities. Therefore, before proceeding to further experimental studies on catalytic VOC oxidation, it is essential to conduct pressure drop measurement testing. The W-shaped structure MFEC, prepared by using 8 μm Ni fibers, was the ultimate configuration considering the pressure drop occurring across the reactor and velocity obtained by the system. Fig. II.10 shows the pressure drop occurring in the W-shaped structure MFEC for various face velocities at three different temperatures. As evident in Fig. II.11, pressure drops follow a quadratic relation with gas velocities that consists of viscous loss and inertial loss. The temperature increase reduced the pressure drop at a certain face velocity as density and viscosity of the air inside the

system changed with the temperature. Viscous loss and inertial loss inside the MFEC and inertial pressure losses at the entrance and exit of the pleated MFEC are closely related to the density and viscosity of the air.

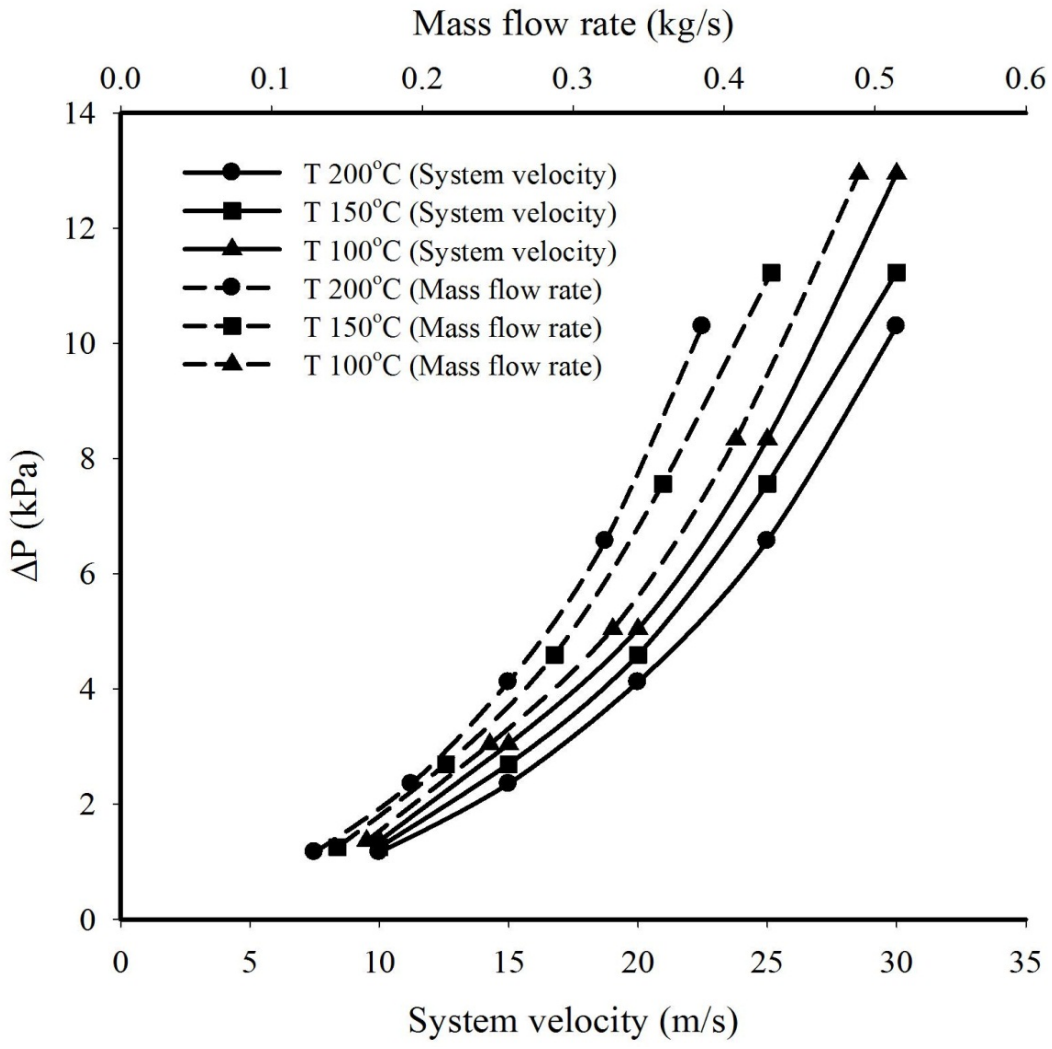

Figure II.11: Experimental pressure drop measurements for MFEC with W-shaped structure at different temperatures

Total pressure drop occurring in the reactor was the summation of pressure drop caused by the entrance loss and exit loss, slot resistant, due to the fibers, and due to the particles. As the

structural array of MFEC was prepared by metal screening and aluminum U-channel, a significant amount of pressure drop was caused by the slot resistance. Fig. II.12 shows the pressure drops caused by the media with the slot and by the slot only. As evident from the plot, pressure drop due to slot resistance also follows the quadratic relation with system velocity. Other than slot resistance, another factor, that affects primarily the pressure drop, is the particles entrapped into the fiber. The major portion of pressure drop is caused by the catalyst particles. Approximately 42% – 59% pressure drop across the media was because of catalyst/support particles entrapped into it according Fig. II.13.

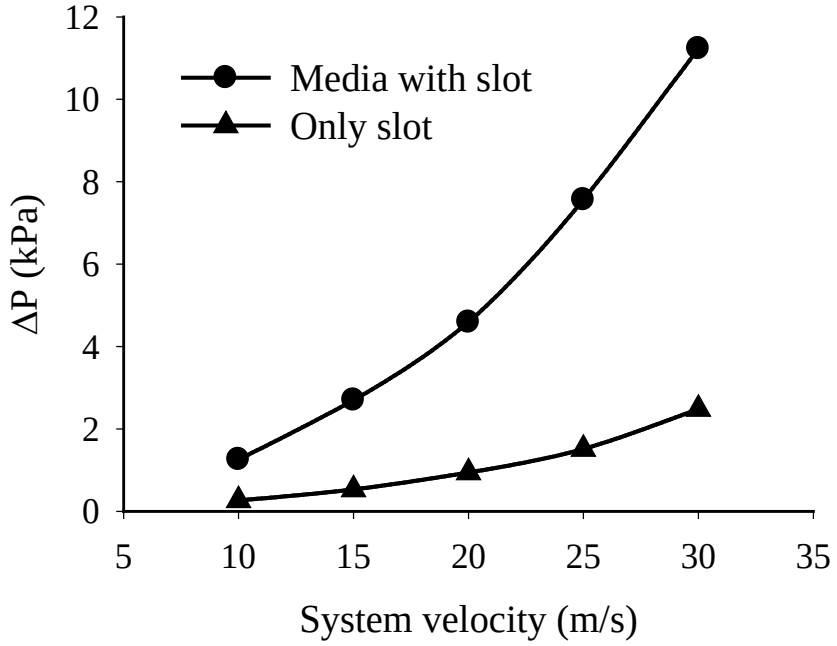

Figure II.12: Pressure drop caused by slot resistance at T = 423 K

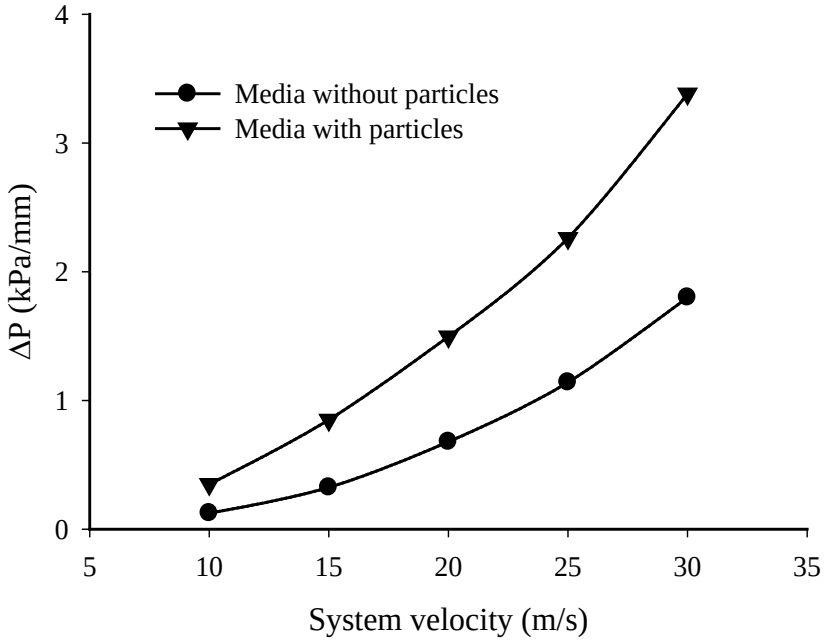

Figure II.13: Pressure drop caused by entrapped particles and microfibers at T = 423 K

II.5 Conclusion:

Fiber dimension has shown significant effect on the pressure drop across of the system. Although large dimensional Ni fibers has enhanced lower pressure drop, media prepared by these fibers were not well dispersed which thereby had caused significant amount of particle loss from the media. On the contrary, small dimensional fiber has increased the pressure drop abruptly although particle loss from these fibers media was low. Therefore, as an optimum fiber dimension for preparing media, 8 μm Ni fiber is preferable than 4 μm and 12 μm Ni fiber. Furthermore, multi-element structured array has substantial impact on the pressure drop as well as on the face velocity. Addition of the element in the structure has reduced pressure drop which facilitated to obtain higher system velocity. W structure has prevailed over the flat structure and the V structure in terms of available fluid flow area, pressure drop, and fluid velocity. This study

has determined the optimum fiber dimension and structural design. The pressure drop occurring in the optimized pleated structure followed quadratic relation with velocity regardless to the system temperature. Furthermore, the entrapped particles in the microfibers of MFEC primarily affected the pressure drop other than slot resistance and entrance and exit loss. The established design was intended for further investigation on catalytic oxidation of VOC at high face velocity. This optimized structure was also intended for experimental comparison among different reactor geometries, i.e., packed beds and wash-coated monoliths.

Chapter III

Catalyst Screening for VOC Removal

III.1 Introduction:

Volatile organic compounds (VOCs) are not only major contributors to air pollution because of their toxicity, malodorous, mutagenic, and carcinogenic nature, but also main precursors of ozone and smog formation [48]. These have remarkable impact on the air quality. VOCs are highly volatile and persistence in air, and have the ability to travel long distance from their emission points and to be transferred to the other compounds in the atmosphere. Due to the progressive increase in VOC concentrations, different methods for VOC elimination have been introduced [47].

The conventional approach for handling high concentration of VOC is thermal incineration, however this technique has high operating cost, as temperatures exceeding 800°C to 1200°C are required to achieve complete VOC destruction [55]. Catalytic oxidation is becoming of increasing importance to control the emissions of VOCs [135]. A brief discussion has been provided in Section I.3.2 on the advantages of catalytic oxidations for VOC abatement. The development of noble metal catalysts and transition metal oxides for catalytic oxidation of VOCs has been widely reported in the literature [57-61]. The commercial catalysts, which are used for the oxidation of VOCs, can be classified into three categories: supported noble metals (mainly Pt and Pd); metal oxides (supported or not); and mixtures of noble metals and metal oxides [136-140].

In this study, n-hexane has been chosen as a model VOC. n-Hexane is one of the paraffinic VOCs difficult to oxidize. Considering the advantages and disadvantages of noble metal and transition metal oxides, the oxidation of n-hexane has been carried out over M_xO_y/γ-

Al_2O_3 (M = Pd, Mn, Ce, and Co). The effects of different catalysts on the decomposition of n-hexane have been investigated. Studies have been carried out at a concentration of 500 ppmv.

III.2 Experimental Details:

III.2.1 Media Preparation:

MFEC was prepared in similar manner with same amount of fibers and cellulose as described in Section II.2.2. But in this step, γ-Al_2O_3 particles (150-250 μm) are entrapped into the fiber. The properties of γ-Al_2O_3 are provided in Table III.1. In this case, 25 g of particles are added to the suspension in the sheet former. Therefore, a three dimensional structure consisting of fibers, cellulose and particle, was formed. Protective layers were also prepared in the same manner which consists of nickel fibers and cellulose only. The schematic diagram of the preform is shown in Fig. III.1. The preform was then dried at 373 K for 2 hr. The alumina particles in MFEC were impregnated by $Pd(NO_3)_2$, $Mn(NO_3)_2$, $Co_3(NO_3)_2$ and $Ce(NO_3)_2$ solution using incipient wetness method in order to obtain desired amount of metal on support. Finally, the impregnated MFEC samples were dried at 373 K and calcined at 748 K for Pd, 673 K for Mn, 648 K for Co, and 748 K for Ce. The bed properties of MFEC that is used in this study are listed in Table III.2.

Table III.1: Properties of the γ-Al_2O_3 particles

Properties	
Surface area (m^2/g)	247
Pore Volume (m^3/kg)	1.15×10^{-3}
Apparent specific gravity	3.58
Void fraction	0.818
Particle density (kg/m^3)	650

Table III.2: Bed properties of MFEC used in the bench scale experiment

Nominal fiber diameter (μm)	8
Particle diameter (mm)	0.19
Catalyst (vol.%)	11.1
Metal (vol.%.)	2.2
Void (vol.%)	86.7

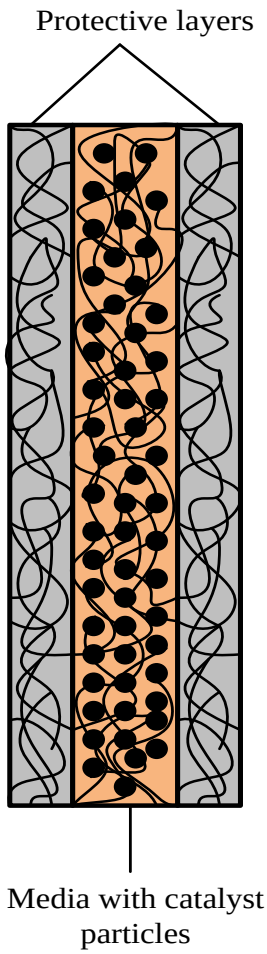

Figure III.1: Schematic diagram of the preform of MFEC

III.2.2 Experimental Set Up:

A schematic description of the experimental set up used in this study is shown in Fig.III.2. The setup can be separated into three sections – gas mixing section, test section, and analytical section. In the gas mixing section, two compressed air streams were used and both of these two steams passed through flow meters. One of the air streams was saturated with hexane by passing it through a bubbler containing liquid hexane, immersed in an ice bath. The ice bath was used to maintain a constant liquid hexane temperature which helped to obtain a steady gas phase concentration throughout the experiment. Required concentrations of hexane challenge

were generated by diluting the hexane saturated air stream with the fresh air supplied from the second flow meter. The two streams were mixed in a glass chamber to minimize the fluctuation in challenge gas concentration. The mixed stream went through the mass flow controller to obtain a desired total flow rate entering the reactor tube.

The test section had a temperature controlled oven which maintained a constant temperature of 473 K. The reactor tube had a length of 305.8 mm and diameter of 25 mm which was placed horizontally. The catalyst bed was placed in the middle of the glass tube. The pressure drop across the reactor bed assumed to be negligible and as the outlet of the tube is vented to the atmosphere, the entire bed could be said to operate at atmospheric pressure. The analytical section had two MiniRAE Lite detectors (RAE Systems Inc.) to measure the hexane concentration in the inlet and outlet streams. The detectors were calibrated with a 100 ppm isobutylene calibration gas obtained from RAE system Inc.

The tests were performed by passing the hexane challenge gas into the reactor tube and measuring the inlet and outlet concentration periodically. Each experiment ran for 120 min for all the tested catalysts in order to obtain steady state concentration at the outlet. The experimental conditions are shown in Table III.3.

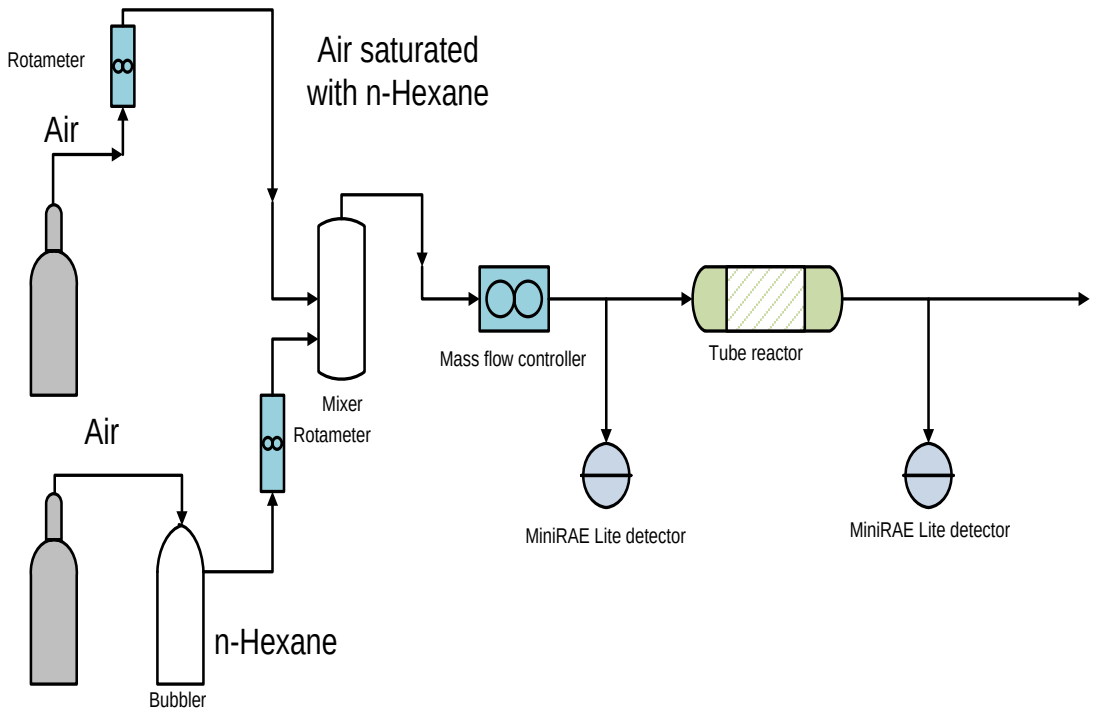

Figure III.2: Schematic description of the experimental apparatus

Table III.3: Operating conditions of the bench scale experiments

Temperature (K)	473
Pressure (kPa)	101.3
Inlet concentration, C_{in} (ppmv)	100, 500

III.3 Results and Discussions:

Fig.III.2 shows the conversion of n-hexane using noble metal (Pd), transition metal (Mn, Ce, and Co), and mixture of these two metals (Pd-Mn and Pd-Ce) as catalysts. In each experiment for different catalysts, the operating conditions i.e., temperature, pressure, mass flow rate, and concentration, of the inlet streams were kept same. For preparing mixed oxide catalysts

(Pd-Mn and Pd-Ce), mixed aqueous solution of $Pd(NO_3)_2$ and $Mn(NO_3)_2/Ce(NO_3)_2$ was prepared. According to the plot, noble metal oxide (PdO) modified by transition metal (Mn, and Ce) exhibited higher conversion than noble metal and transition metal separately. PdO modified by these reducible oxides improved the oxygen storage capacity of the catalysts, redox properties, and enhanced the catalytic activity at low temperature.

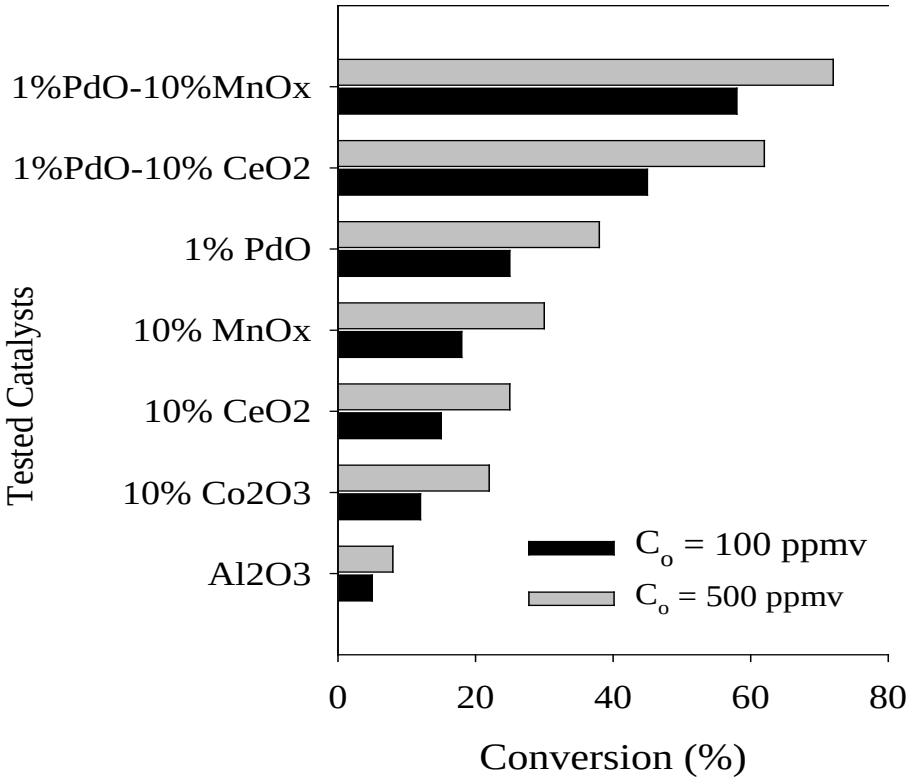

Figure III.3: n-Hexane conversion using different metal oxide catalysts

In this work, preferable catalyst for VOC decomposition was screened although the operating conditions were not similar to the condition in high volumetric test recycle loop as mentioned in Section II.2.3. As alkanes are very difficult to decompose at low temperature (< 473 K), n-hexane has been employed as a representative of VOC. While performing VOC decomposition in high volumetric test rig, other types of VOC i.e., alcohol, aromatic, alkane, and

alkene, was considered. Furthermore, for catalyst preparation MFECs have been used instead of using the support particles only. The reason was to match with the actual bed system.

III.4 Conclusion:

Catalytic decomposition of n-hexane was performed using noble metal, transition metal oxides and mixture of both noble metal and transition metals as catalysts. The order of the catalytic activity of tested catalysts were: mixed metal oxide (noble metal and transition metal) > noble metal oxide > transition metal oxide. The reducible oxides in mixed catalysts enhanced the oxygen storage capacity of catalysts, which thereby increased the catalytic activity. This experimental work has been intended to identify the preferable catalysts that can be used to decompose VOC at high face velocity in high volumetric test rig, although the operational face velocity was not the same as the challenge conditions, i.e., velocity.

Chapter IV

Catalytic Material with Enhanced Contacting Efficiency for VOC Removal at Ultra-short Contact Time

IV.1. Introduction

Application of catalytic reaction in cases requiring high mass flow rates results in microsecond contact times. While having minimal reactor weight and volume, achieving high conversion requires a high contacting efficiency catalytic material where *heterogeneous contacting efficiency* (η_{HCE}) of the catalytic material relies on the logarithmic removal of reactant concentrations per unit of the pressure drop. Packed bed reactors and wash-coated monoliths are intended commercially as catalytic reactors for those applications [11, 12, 35, 36]. However, packed beds result higher pressure drops, and monoliths cause low fluid-solid mass transfer rates, and non-uniform fluid distribution that causes lower reactor effectiveness. Therefore, to achieve high η_{HCE} materials, researchers are paying more attention to the micro-structured and micro-engineered systems that provide small characteristic dimensions and higher external surface area.

Microfibrous entrapped catalyst (MFEC) is an interesting and unique composite material that could provide an innovative approach for creating more effective lightweight heterogeneous contacting systems [13-17]. MFEC prepared by the traditional wet lay paper making process, can entrap particles as small as 50 μm into sinter locked three dimensional fiber (2-20 μm) matrices. Microfibrous entrapped ZnO/SiO_2 adsorbent has exhibited improved performance (2-3 folds) over packed bed in gas phase desulfurization of hydrogen reformate streams [20, 21, 24, 27]. Moreover, Chang et. Al [27] has viewed MFEC as a remarkable material for preferential catalytic oxidation and low temperature oxidations of CO in hydrogen reformate streams.

Furthermore, microfibrous entrapped activated carbon beds and Ni/Al_2O_3 catalysts have shown significant benefits in volatile organic compound (VOC) adsorption [29, 30] and in toluene hydrogenation for trickle bed reactors [31]. Sheng et al [33] has observed remarkable improvement in temperature distribution as well as product selectivity in Fischer-Tropsch Synthesis due to the presence of metal fibers in MFECs. Furthermore, pleated MFEC when used for single pass removal of ozone has shown better performance than packed beds and commercial monolith [32]. Furthermore, pleated microfibrous media has shown enhanced performance in air filtration system by removing harmful airborne contaminants [141]. Pleated MFEC leads to higher reactions rates and lower pressure drops due to smaller characteristic dimensions as compared to the other heterogeneous contacting systems.

Volatile organic compounds (VOCs) include varieties of organic compounds, e.g., aliphatic, aromatic, aldehyde, ketone, ester, organic acid, chlorinated hydrocarbon, etc., that have high enough vapor pressure under normal condition to evaporate into the air and contribute to the formation of photochemical smog. VOCs are an important class of indoor and outdoor air toxins due to the short- and long-term adverse health effects. The progressive increase of VOC emissions, the information of the hazardous nature, and the resulting increasingly more restrictive environmental regulations in the industrialized countries, have induced the development of different methods for the elimination of VOC [48] i.e., thermal incineration, catalytic oxidation, bio-filtration, ultraviolet oxidation, etc.. Among all of the available techniques, catalytic oxidation is the most effective and economically feasible method for VOC removal [55]. Catalytic oxidation can operate with dilute VOCs effluent stream (< 1%) and at much lower temperatures. Catalysts typically used for VOC removal are noble metals e.g., platinum (Pt) or palladium (Pd), due to the stability and higher activity. Many catalytic processes

have been commercialized and successfully operated by using noble metal catalysts [54, 136-139]. In this work, Pd-Ce/γ-Al_2O_3, and Pd-Mn/γ-Al_2O_3 based pleated MFECs have been used as catalysts for VOC removal.

In this study, catalytic VOC removal involving high mass flow rates was used to demonstrate and to understand the advantages of pleated MFEC structures. Additionally, the influence of low intra-layer residence time and reaction kinetics was investigated in the velocity controlled region. Ethanol, toluene, and n-hexane were chosen as the representatives of VOCs.

IV.2 Experimental Details

IV.2.1 Media Preparation

MFEC was prepared in the similar fashion as mentioned in Section III.2. In this case, amount of Ni fiber and γ-Al_2O_3 was 12.5 g and 30 g, respectively. The properties MFEC bed has been shown in Table IV.1. Palladium nitrate ($Pd(NO_3)_2.2H_2O$), and manganese nitrate ($Mn(NO_3)_2.4H_2O$) were obtained from Alfa Aesar, and cerium nitrate ($Ce(NO_3)_2.6H_2O$) were obtained from Sigma Aldrich. During catalyst preparation, the $Pd(NO_3)_2$ solution, $Ce(NO_3)_2$ solution, and $Mn(NO_3)_2$ solution were used to wet impregnate the γ-Al_2O_3 particles in microfibrous media. For preparing Pd-Ce catalyst, 0.1 M $Pd(NO_3)_2$ solution and 0.78 M $Ce(NO_3)_2$ solution had been mixed together for preparing the Pd-Ce catalyst, whereas for preparing the Pd-Mn catalyst, 0.1 M $Pd(NO_3)_2$ solution and 1.98 M $Mn(NO_3)_2$ solution had been mixed. Pd is used widely in VOC abatement due to its stability and higher activity. Finally, the impregnated MFEC samples were dried at 373 K and calcined at 748 K for 4 h. MFEC sheets with PdO-CeO_2/γ-Al_2O_3, and PdO-MnO_x/γ-Al_2O_3 were thus prepared.

Table IV.1: MFEC cases and bed properties used for VOC removal in high volumetric test rig

Numbers of pleat	1 and 4
Particle diameter, d_p (mm)	0.19
Catalyst (vol.%)	11.1
Metal (vol.%)	2.2
Void (vol.%)	86.7

The amounts of the Pd, Ce, and Mn, in the catalysts were determined by inductively coupled plasma-atomic emission spectroscopy (ICP-AES) (Hazen Research Inc.), which is shown in Table IV.2.

Table IV.2: Metal content of the tested catalysts

Sample	**Metal Content**		
	Pd (wt.%)	**Ce (wt.%)**	**Mn (wt.%)**
Pd-Ce	2.97	8.93	
Pd-Mn	3.59	-	7.57

IV.2.2 VOC Insertion to the High Volumetric Test Recycle Loop:

Compressed air was used to vaporize liquid ethanol, toluene, and n-hexane and then mixed with the air stream from the blower to obtain the desired challenge gas concentration (100 ppmv) at the inlet of the reactor. In this case, a vaporizer (Fig. IV.1) was used where liquid VOCs were supplied by a peristaltic pump from the top and compressed air was passed through it from the bottom. MiniRAE Lite (RAE Systems) was used to measure the VOC concentration at the inlet and outlet of the reactor. The PLC controller was used to control the VOCs

concentration at the inlet stream. J-type thermocouples (Omega) were used to measure the temperatures. The experiments were conducted at different temperatures those were in the range from 373 K to 473 K. The operating conditions are shown in Table IV.3. Fig IV.2 shows the schematic diagram of the test set up after the injection of VOCs.

Figure IV.1: VOC vaporizer

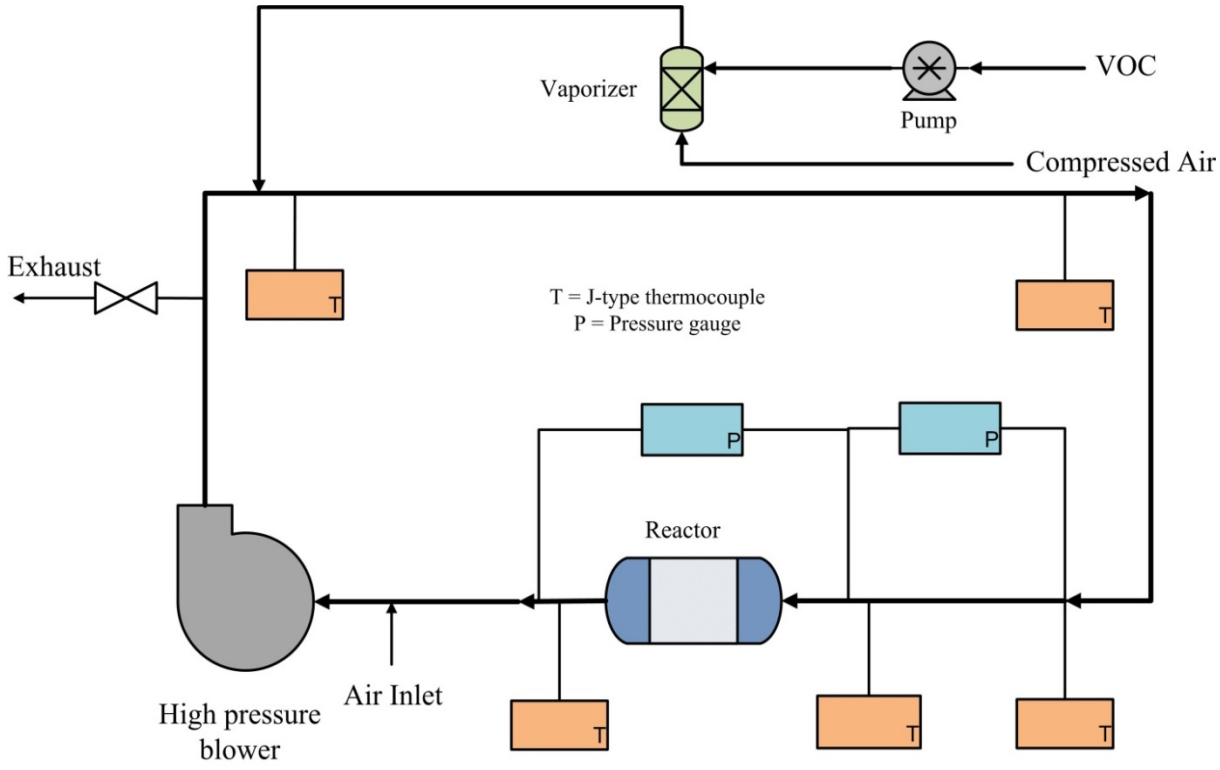

Figure IV.2: Schematic diagram of the test recycle loop with VOC insertion

Table IV.3: Operating conditions used in the high volumetric test rig

Temperature (K)	373 - 473
Pressure (kPa)	101.3
Inlet concentration (ppmv)	100

IV.3 Results and Discussion:

High face velocities resulted in low intra-layer residence time or in higher GHSV, as shown in Table IV.4. Furthermore, small characteristic dimension of the MFECs enhanced the laminar behavior even though the system velocities were significantly high. Fig. IV.3 – IV.8 show the conversions of ethanol, toluene, and n-hexane at high face velocities using flat-shaped

and W-shaped structure MFECs at 473 K. According to the figures, due to pleating of MFECs, conversion was increased. This can be attributed to the low effective velocities inside the media. Due to pleating, actual velocity was reduced by the factor of pleat number. Therefore, effective velocity was reduced, in other words, intra-layer residence time was increased which improved the conversion. For each VOC, Pd-Ce/Al_2O_3, and Pd-Mn/Al_2O_3 have been used. These results were valid for both types of catalyst. As W-shaped structure MFEC exhibited higher conversion than flat shaped MFEC, the structure was considered for further investigation.

Table IV.4: Flow conditions inside the pleated media

System velocity, v_o (m/s)	3-30
GHSV (h^{-1}) ($\times 10^6$)	1.3 - 52.2
Reynolds number, Re	2.84-114

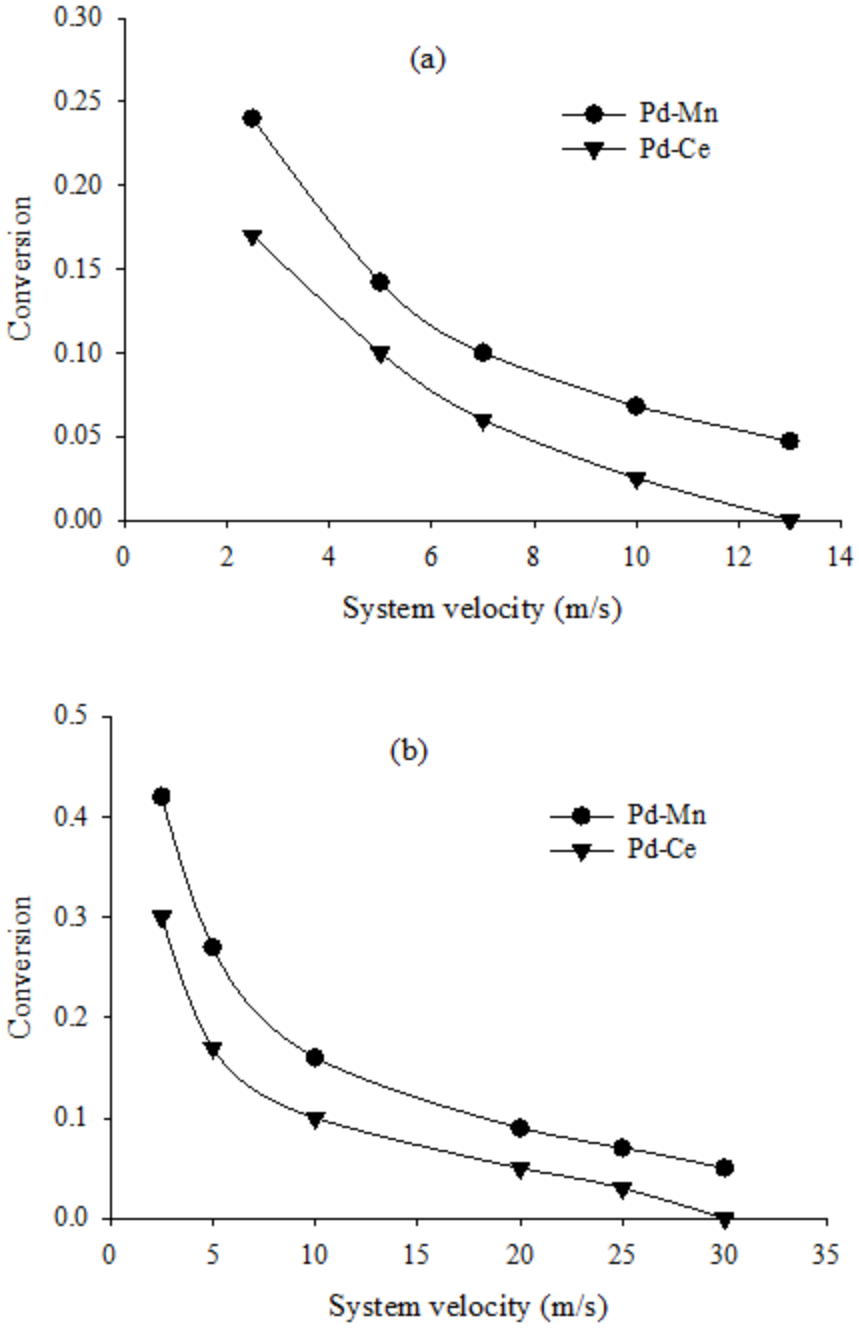

Figure IV.3: Ethanol conversion using Pd-Mn/Al_2O_3 and Pd-Ce/Al_2O_3 catalysts (a) in flat shaped MFEC; (b) in W-shaped MFEC

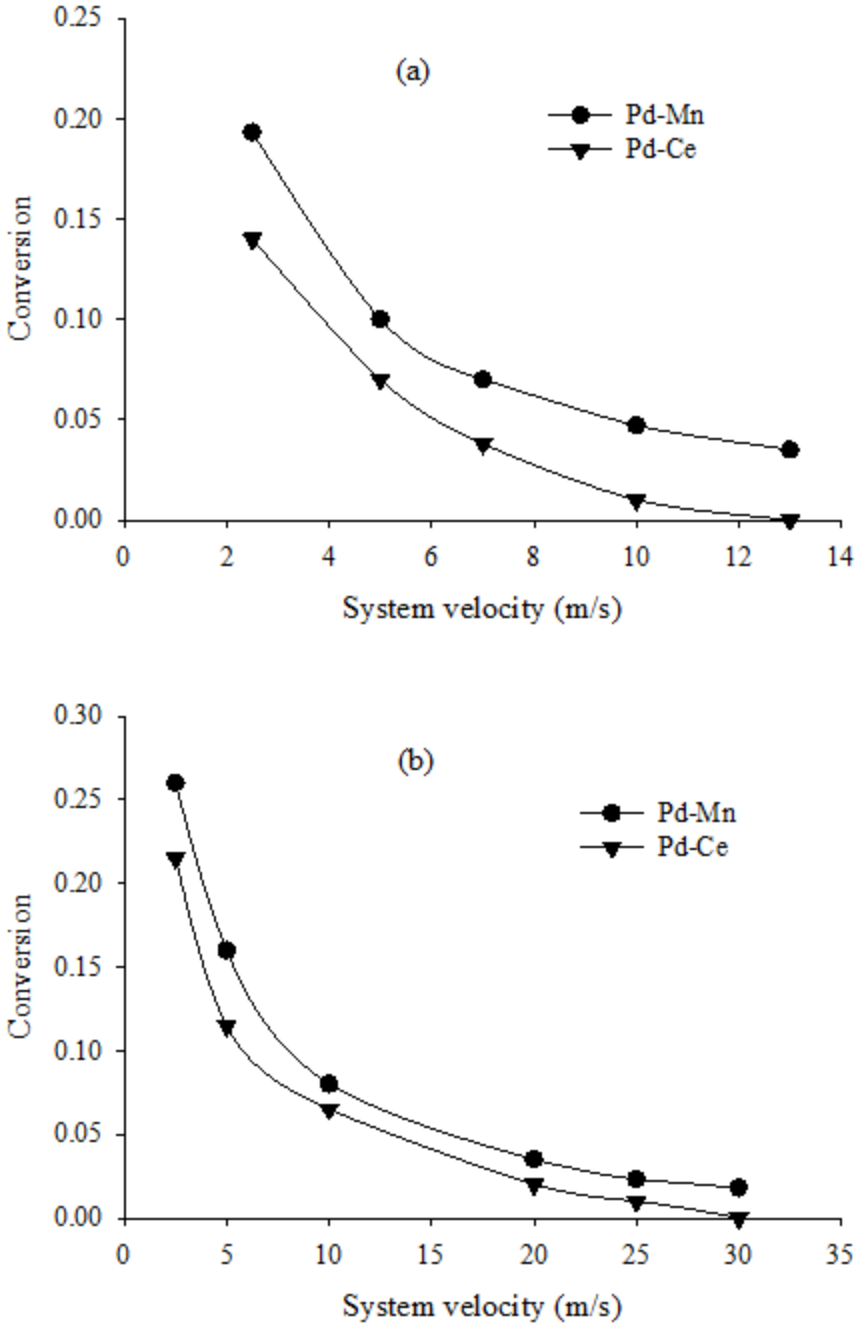

Figure IV.4: Toluene conversion using Pd-Mn/Al_2O_3 and Pd-Ce/Al_2O_3 catalysts (a) in flat shaped MFEC; (b) in W-shaped MFEC

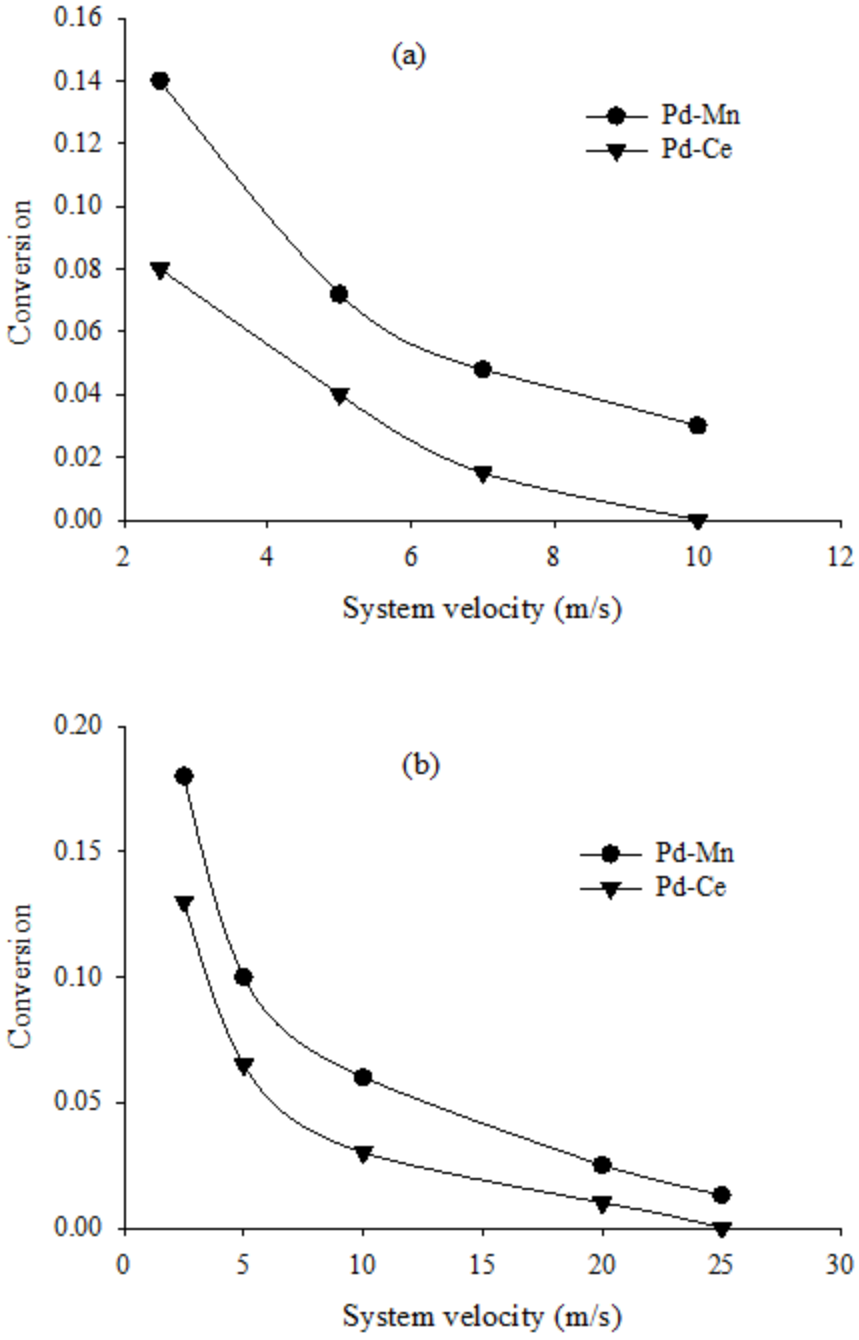

Figure IV.5: n-Hexane conversion using Pd-Mn/Al_2O_3 and Pd-Ce/Al_2O_3 catalysts (a) in flat shaped MFEC; (b) in W-shaped MFEC

Fig. IV.6 – IV.8 show the conversions of VOCs using W-shaped structure at different temperatures. The high gas velocities indicate the short contacting reaction. Regardless to the catalysts and the temperatures, the conversion decreased when the velocities increased. This is due to the higher GHSV or lower intra-layer residence time inside the media. As evident from the above mentioned plots, the residence time had very significant effect on conversion. At medium and low face velocities, comparatively low VOC removals were obtained. These low conversions can be attributed to the fact that the overall reaction rates were limited by surface reactions as the compounds diffuse through the pore mouth of the catalyst rapidly. Furthermore, the system temperature (< 473 K) was not high enough for these VOCs to undergo complete removal due to the limitations in the design of the present test apparatus.

The VOC removal can be explained according to the Mars-Van Krevelen mechanism which is an oxidation-reduction process [56, 87, 88]. A detailed discussion on the Mars-Van Krevelen mechanism is presented in Section I.8.3. The VOC to be oxidized reduced the catalyst, which was oxidized by the oxygen from the air. This two-stage model is explained by a slow catalyst reduction controlled by surface reaction between the VOC and metal oxides, followed by fast re-oxidation of surface vacancies. Due to the low intra-layer residence times, the VOCs did not have enough time to reduce the metal oxide whereas the reaction between these two compounds is the rate limiting step. In order to achieve higher conversion at these residence times, the system requires higher temperature which was not obtainable due to structural limitation.

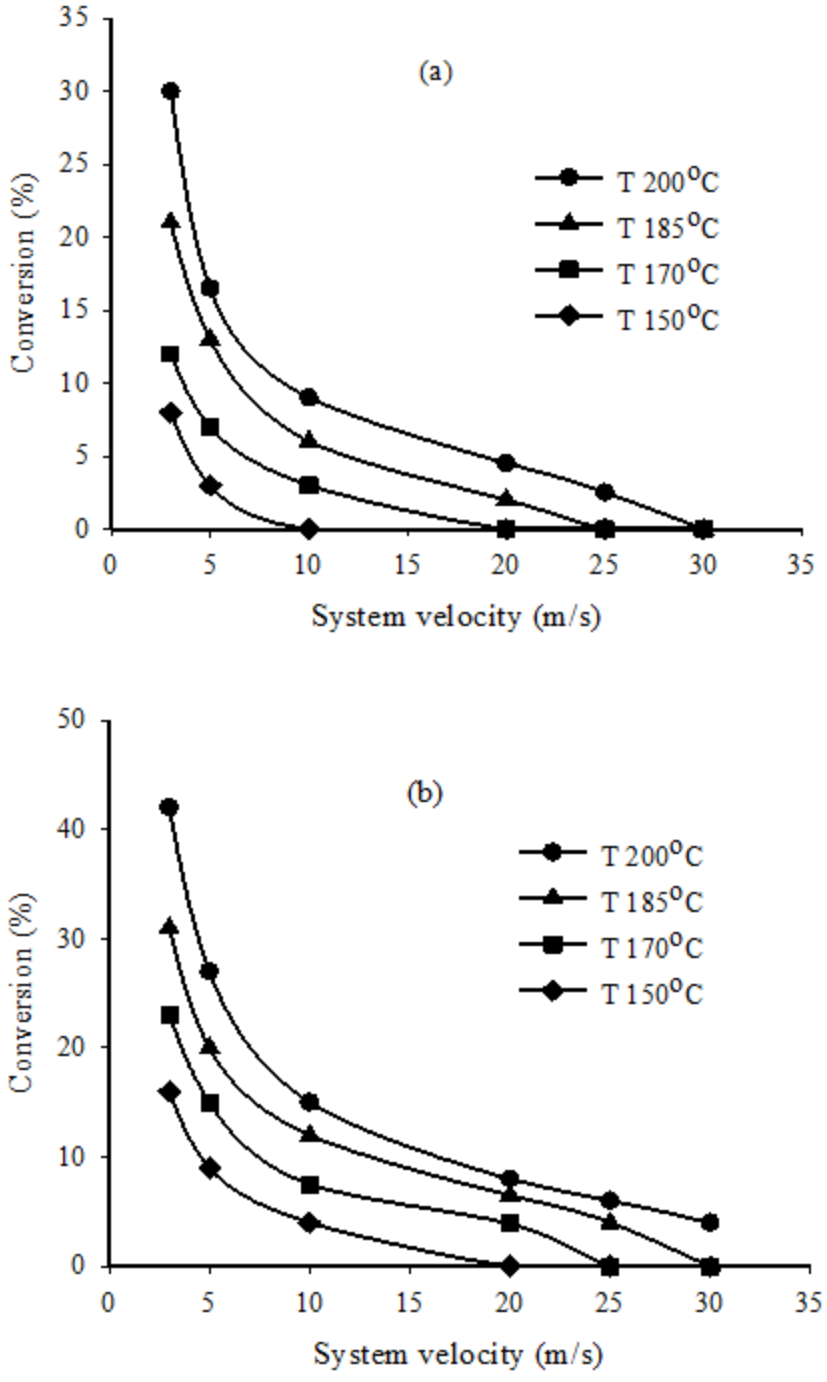

Figure IV.6: Ethanol conversion at different temperatures using different catalysts (a) Pd-Ce/Al_2O_3; (b) Pd-Mn/Al_2O_3

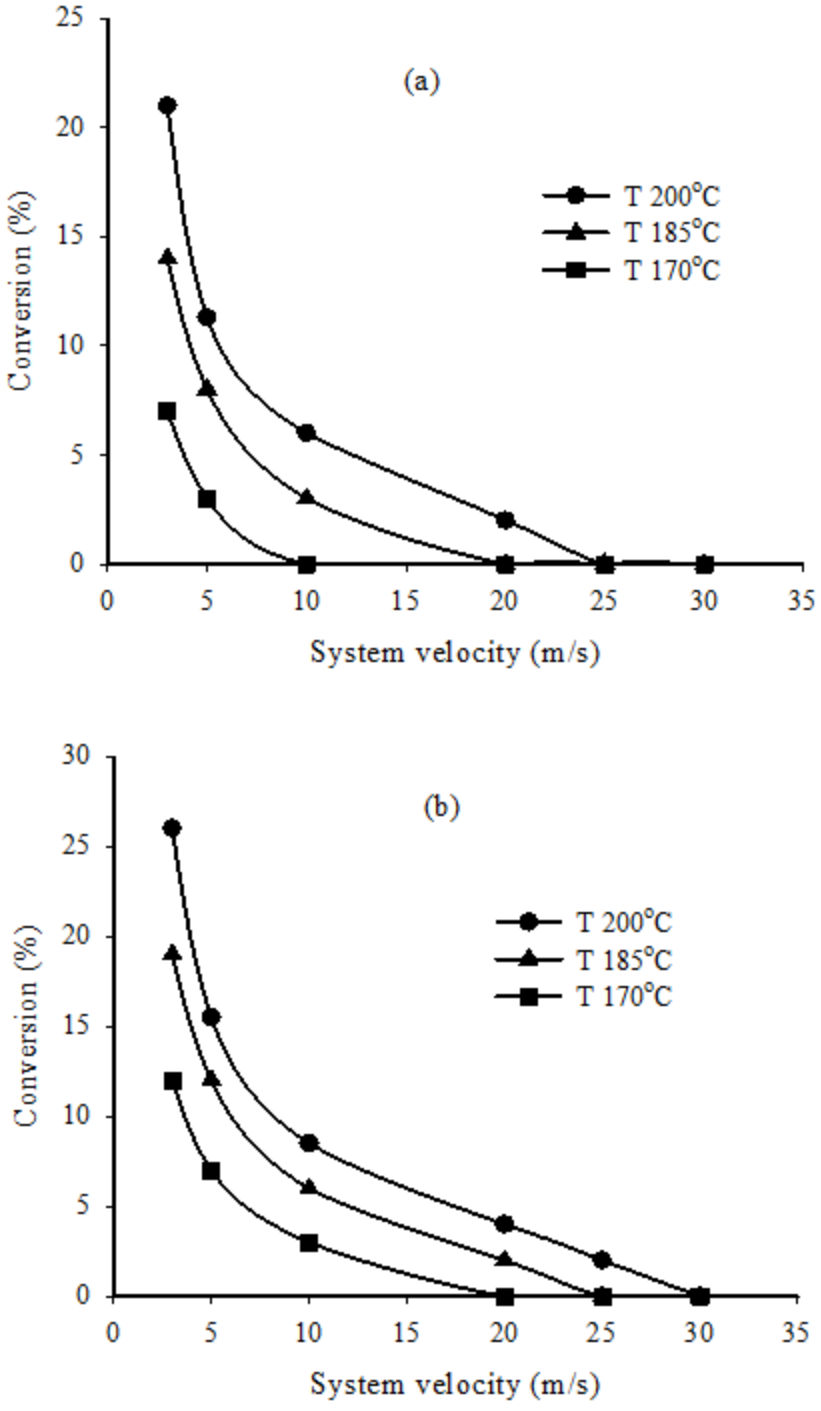

Figure IV.7: Toluene conversion at different temperatures using different catalysts (a) Pd-Ce/Al_2O_3; (b) Pd-Mn/Al_2O_3

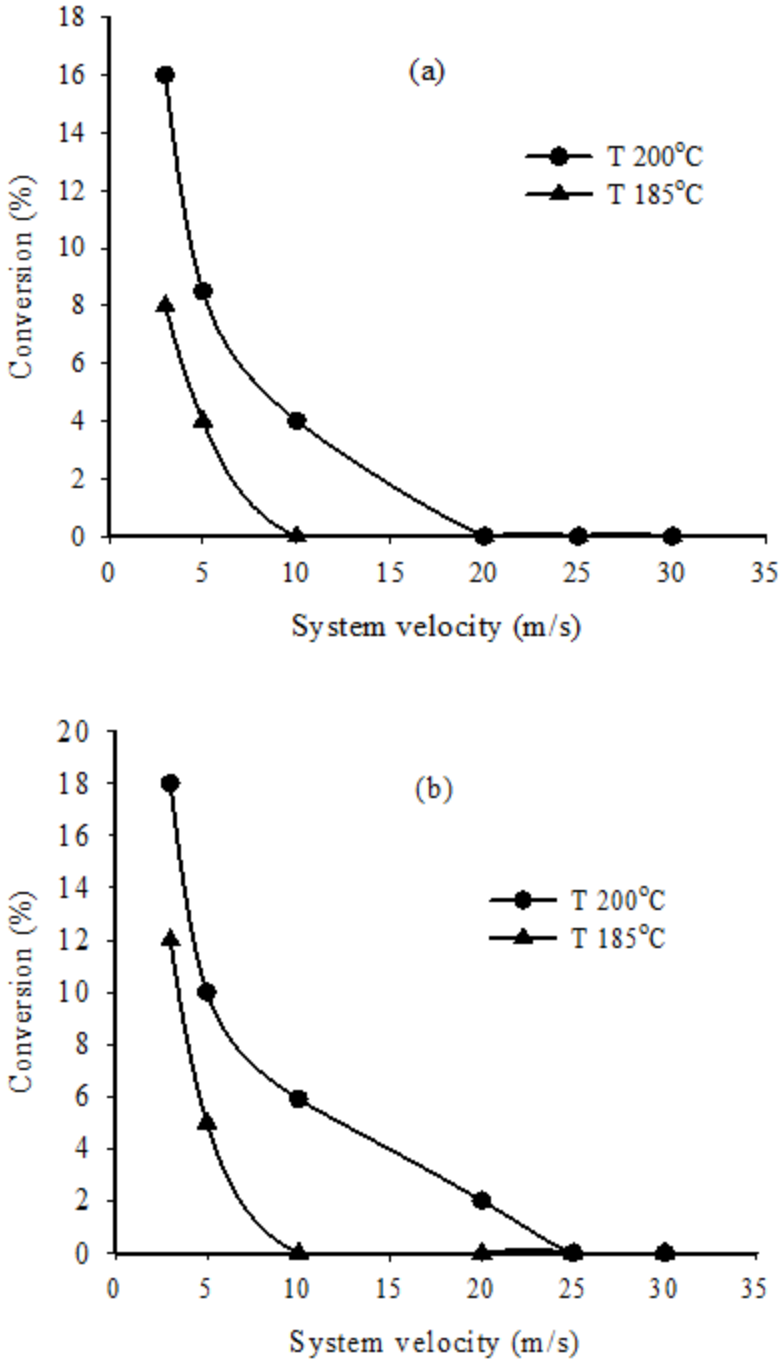

Figure IV.8: n-Hexane conversion at different temperatures using different catalysts (a) Pd-Ce/Al_2O_3; (b) Pd-Mn/Al_2O_3

For all VOCs, no significant removal was observed with the PdO supported Al_2O_3. While PdO was modified by CeO_2 and MnO_x, the PdO activity increased rapidly and the VOCs start decomposing even at high gas velocities at the same temperature. According to the Mars-Van Krevelen mechanism, when the VOC is oxidized at the surface, the oxidant is often a surface lattice oxygen atom, thus creating a surface oxygen vacancy. VOC removal over PdO catalyst supported on non-reducible oxides (e.g., Al_2O_3) is a structure sensitive reaction, involving the activation of oxygen on the noble metal. However, when PdO catalyst is modified by reducible oxides (e.g., CeO_2, MnO_x), catalytic activity depends on both the oxygen activation on the active metal and the capacity of the oxide for providing active lattice oxygen. MnO_x and CeO_2 provide high oxygen storage capacity by taking up oxygen under oxidizing conditions and releasing it under the reducing conditions [88, 142-146]. Therefore, PdO modified by reducible oxides improved the oxygen storage capacity of the catalyst, redox properties, and enhanced the catalytic activity at low temperatures. Furthermore, the catalytic reactivity of the VOCs decreased in the following order: ethanol > toluene > n-hexane. In general, the ease for decomposing VOC by precious metal catalysts follows the general order of alcohols > aldehydes > aromatics > ketones > alkenes > alkanes [138, 147, 148]. However, in this study, the product was investigated in terms of reactant removal only rather than identifying the products and their concentrations. Therefore, the sequential reaction mechanism might occur depending on the type of VOC formed at the outlet.

$$R - H + Cat - O \rightarrow R - OH + Cat^*$$

$$R - OH + Cat - O \rightarrow R - CHO + Cat^* + H_2O$$

$$Cat^* + O_2 \rightarrow Cat - O$$

$$R - CHO + Cat - O \rightarrow R - COOH + Cat^*$$

$$Cat^* + R - OH \rightarrow R - H + Cat - O$$

$$R - H + Cat - O \rightarrow R - Cat - O^*$$

$$R - Cat - O^* + O_2 \rightarrow CO_2 + R - H + Cat - O$$

$$R - H + Cat - O \rightarrow R - Cat^* + H_2O$$

$$R - Cat^* + O_2 \rightarrow R - OH + Cat - O$$

$$R - Cat - O^* + O_2 \rightarrow CO + R - H + Cat - O$$

An important goal of this work was to investigate the performance of pleated MFEC at high face velocities for catalytic applications. Many performance aspects such as pressure drop, chemical conversion, amount of catalyst utilization, cost of construction, catalyst life, etc., would be involved in evaluating the overall performance of a reactor system [39]. Since it is difficult to define a single term that can judge all these aspects, only few selected parameters were examined here: chemical conversion and pressure drop per unit length of reactor bed. A similar approach was employed by Kołodziej and Łokewska [49] for evaluating the performance of structured reactors with short channels.

As the characteristic length of a given system decreases, the mass transport (i.e., chemical conversion) and momentum transport (i.e., pressure drop) increases. While the former is desirable, the latter is not since the system will need to be operated at higher pressures. For a given material, there should be an optimum characteristic length which gives the best performance. Hence, *heterogeneous contacting efficiency* (η_{HCE}), a dimensionless number, is defined as the product of mass efficiency (i.e., conversion achieved) to flow efficiency (i.e., inverse of pressure drop), per unit surface area of the catalyst (a measure of catalyst utilization).

The mass efficiency (η_{mass}) is defined as the log reduction of VOC concentration achieved per unit surface area of the catalyst, as shown in Eq. IV.1.

$$\eta_{mass} = \frac{\log\left(\frac{C_{in}}{C_{out}}\right)}{n_p(\pi D_p^2)} \tag{IV.1}$$

The flow efficiency (η_{flow}) is defined as the inverse dimensionless pressure drop across the material.

$$\eta_{flow} = \frac{\frac{1}{2}\rho \upsilon_o^2 n_p(\pi D_p^2)}{\Delta P} \tag{IV.2}$$

So, the overall η_{HCE} is defined as the product of η_{mass} and η_{flow} which is independent of the amount of catalyst, according to Eq. IV.3. The higher the η_{HCE} value, the better the performance of the structured reactor, as it indicates higher conversion with lower pressure drop.

$$\eta_{HCE} = \eta_{mass} \times \eta_{flow} = \frac{1}{2}\frac{\log\left(\frac{C_{in}}{C_{out}}\right)}{\Delta P}\rho \upsilon_o^2 \tag{IV.3}$$

Fig. IV.9 shows the comparisons of η_{HCE} versus superficial velocity for various pleated MFEC and different VOCs at the same inlet conditions. In each experiment, system temperature, catalyst loading, and media thickness were kept the same for different pleated configurations. It is evident from the plot that an increase in pleat number increased the η_{HCE} value. With an increase in the *PF*, the effective velocities in MFEC were cut down by an equivalent factor and the pressure drop decreased accordingly. For the same reason, the residence times as well as the associated conversions increased with the increase in *PF*. This clearly demonstrates that the high *PF* value of MFEC designs can provide higher conversions with lower pressure drop.

Furthermore, for higher reactive compound e.g. ethanol, the value of η_{HCE} is comparatively higher than less reactive compounds.

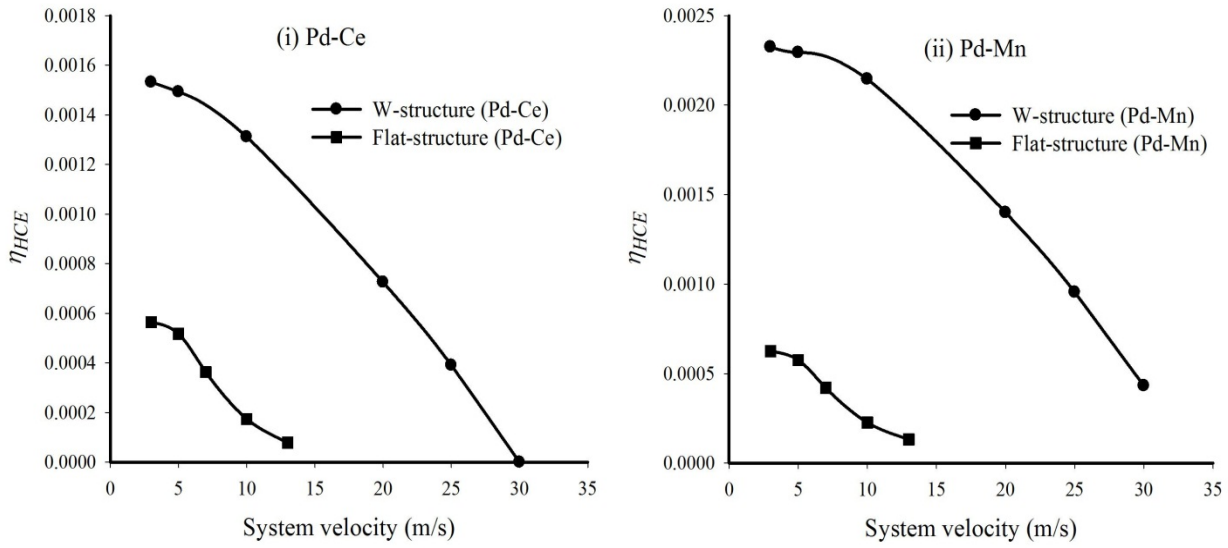

(a) Ethanol

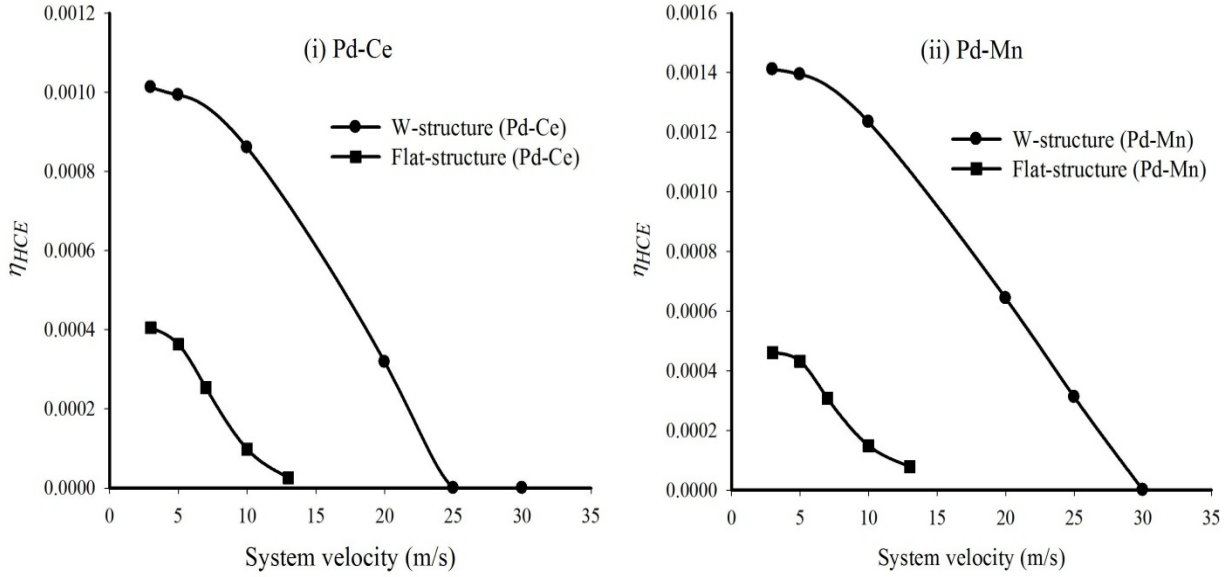

(b) Toluene

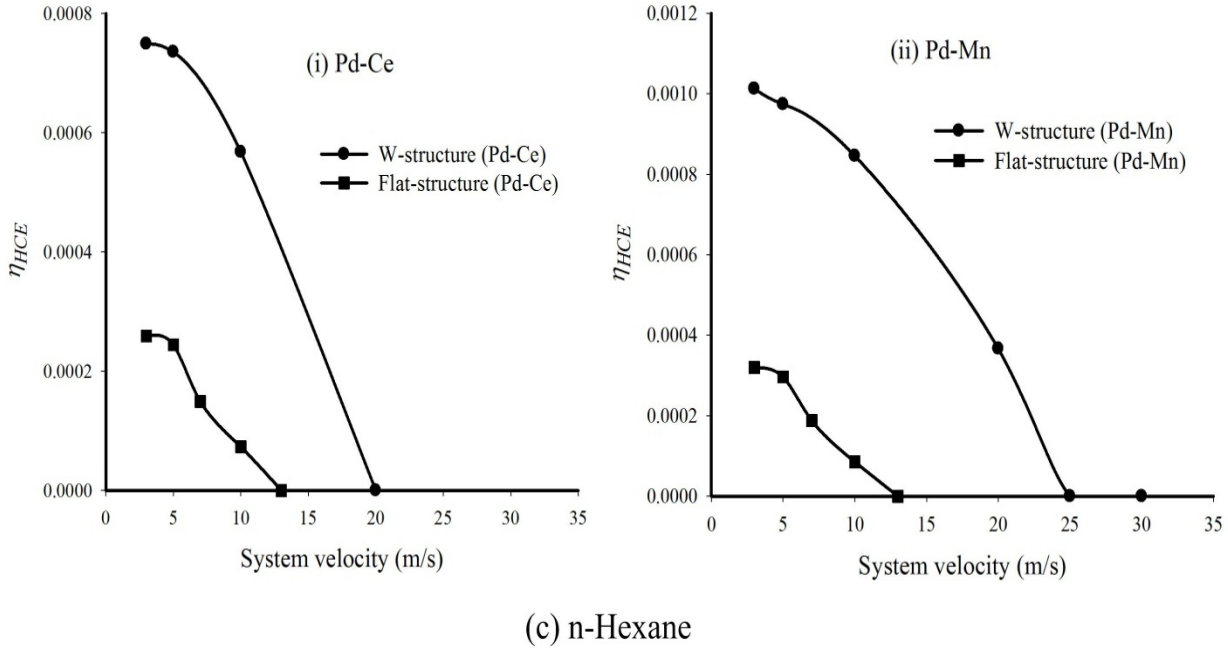

Figure IV.9: η_{HCE} versus system velocity for different pleated MFEC structures (Flat and W-shaped structure); (a) Ethanol; (b) Toluene; and (c) n-Hexane (T = 473 K)

In these experiments, MFEC reactor operation was not in the inter-phase mass transfer controlled regime, and hence, there is further scope for improving the reactant conversion in MFEC by increasing the catalytic activity. The bed composition and properties (*PF*, voidage, catalyst loading, etc.) of MFEC structure also requires further optimization in order to derive their full benefit.

IV.4 Conclusion:

A novel catalytic structure with enhanced heterogeneous contacting efficiency was developed for VOCs removal where the process involved high gas velocities. These high gas velocities indicated to the low intra-layer residence times. The results demonstrated that pleated MFEC had caused a decrease in the effective velocity (inside MFEC media). This decreased

effective velocity resulted in lower pressure drop and also higher residence time or, in other words higher conversions. This dual advantage achieved with pleating MFEC media leads to higher η_{HCE} values. Furthermore, the low intra-layer residence time inside the MFEC reduced the VOC removal and caused the surface reaction rate to be the limiting factor for overall reaction rate. These VOCs removal can be explained by the Mars-Van Krevelen mechanism which is an oxidation-reduction process. The results also verified high oxygen storage capacities of reducible oxides while noble metal oxide modified by these oxides showed better performance. Pleated MFEC showed promising performance in this study as it provided a large surface/volume ratio for the entrapped catalyst. This attribute facilitates the weight and volume demand of the air handling system in a limiting space. As the bed properties of microfibrous materials can easily be tailored to the requirement of specific applications, the study was further focused on the comparison of pleated MFEC with other conventional heterogeneous contacting systems, e.g., wash-coated monoliths and packed bed catalyst particulates.

Chapter V

Experimental, Theoretical, and Computational Comparison of Pressure Drop Occurring in a Pleated Catalyst Structure

V.1 Introduction:

As almost every process uses porous media, e.g. fixed bed reactors, packed distillation columns, adsorbent beds, filters, heat pipes, etc., pressure drop is an extremely important criterion for reactor and filter designs. Pressure drop should be checked at the early stage in the design with the purpose of assessment its influence in order to have high contacting efficiency through the catalyst media [149]. Typically, the blower energy requirement and heterogeneous contacting efficiency are calculated in terms of the pressure drop. Therefore, it is essential to study the pressure drop mechanism and to investigate the associated losses, i.e., frictional loss and form drag loss for MFECs. In literature, several equations are available for predicting the pressure drop across a system. However, these equations are applicable only for a certain range of porosity, either for low porosities or for porosities approaching unity. Cahela and Tatarchuk [13, 37] have developed an equation for porous media permeability (PMP) by combining the frictional losses estimated by Hagen-Poiseuille equation, and the form drag losses estimated from the Stokes' law. This PMP equation is directly applicable for MFEC. Karwa et al. [133] have introduced an empirical correction factor for the heterogeneity created by large diameter particles entrapped in small dimensional fibers. In this study, this PMP equation has been modified by two variables in order to make it applicable for pleated MFEC at high fluid velocity. Due to the dimensional difference in fiber and particle in MFEC, the above mentioned correction factor have been introduced into the PMP equation. Furthermore, a pleat factor term (*PF*) has been incorporated in the PMP equation for the pleated geometry.

The underlying mechanisms behind the enhanced reactivity of the microfibrous media are not fully understood. With the aim of understanding the basic physical and chemical characteristics of MFEC and optimizing the effectiveness and performances, computational fluid dynamics (CFD) have been applied to predict pressure drops across the media [38] and to measure the increase in mass transfer rates due to the fibers [19]. Duggirala et al. [38] has shown that CFD can provide insights into the detailed fluid mechanics, as well as the global properties of the flow. Based on the previous research [38], CFD has been employed in this study, on pleated MFEC, which possesses high void fraction, to understand the flow characteristics of a system and to analyze the pressure drop across the media. Hence, this research is focused on making the comparisons of the pressure drop among theoretical and computational modeling with experimental data.

V.2 Pressure Drop Modeling:

V.2.1 Theoretical and Semi-Empirical Analysis using Porous Media Permeability Equation:

In literature, there are few widely used models available for estimating pressure drops across the void structure [94-97, 100, 103]. The Ergun equation is commonly used to calculate the pressure drop across a packed bed [99, 150]. According to the Ergun equation, total pressure drop across the bed is the summation of viscous loss and inertial loss, where first term corresponds to the Blake-Kozeny equation for laminar flow [95, 96] and second term corresponds to the Burke-Plummer equation for turbulent flow [97]. The Ergun equation has been shown to be valid for solid fractions from 0.4 to 0.6 [151, 152]. Another popular pressure drop model for a fluidized bed is the Brinkman equation, which is valid for a solid fraction from

0.05 to 0.2 [103]. The Davies model is an empirical formula for pressure drop across a filter media, which is applicable for solid fraction from 0.006 to 0.3 [153]. For high porosity materials, these equations are incompatible as they do not take into account form drag losses, which are the dominant contribution to the pressure drop for flow through high porosity materials.

Microfibrous media has a high porosity that is greater than 0.8. A porous material permeability (PMP) equation was developed by using the combination of the Blake-Kozeny equation and the Stokes' law for the viscous pressure losses and the combination of the Burke-Plummer equation and the form drag losses of a sphere in turbulent flow for the inertial pressure losses [13, 37]. This equation can be used to predict the pressure drop in a multiparticulate beds with voidage as high as 0.99. The total pressure drop for a mixture of solid particles and fibers of any shape is shown in Eq. V.1. The detailed derivation and explanation of this equation and the significance of each term have been discussed in the above mentioned references. However, the particles entrapped in MFEC are irregularly shaped. Therefore, drag co-efficient (C_D) in inertial loss term requires modification, which is based on the assumption of a spherical particle. The analysis of drag force on a particle in a flowing system generally uses a relationship between the drag coefficient and the particle Reynolds number. For Reynolds number greater than 100, turbulent slip prevails and surface condition of the particle has a dominant effect on the drag coefficient. Therefore, the drag coefficient is correlated to the Reynolds number and the sphericity according to Eq.V.2 [154]. This equation is applicable for particles of sphericity from 0.2 to 1 in either Newtonian or non-Newtonian fluids, and for Reynolds number from 0.001 to 10000.

$$\frac{\Delta P}{L} =$$

$$72\frac{\tau^2}{cos^2\theta}\frac{\mu v_0}{g_c}\frac{(1-\varepsilon)^2}{\varepsilon^3}\times\left[\left(\sum\frac{x_i}{\varphi_i D_i}\right)^2+x_{FD}\sum\frac{x_i}{(\varphi_i D_i)^2}\right]+6\frac{\tau^3}{cos^3\theta}\frac{\rho v_0^2}{2g_c}\frac{(1-\varepsilon)}{\varepsilon^3}\sum\frac{x_i}{\varphi_i D_i}\left[C_f+\right.$$

$$\left.C_{FD}\varepsilon\right] \quad \text{(V.1)}$$

$$C_D=\frac{30}{Re}+\frac{67.289}{e^{5.03\varphi}} \quad \text{(V.2)}$$

As mentioned before, MFEC can be easily pleated. Therefore, pleat factor (*PF*), a term frequently used with MFEC system, is defined by Eq. V.3. As a result of pleating, gas velocity decreases in the MFEC. Hence, Kalluri et al. [32] has incorporated the *PF* term in the PMP equation to correct the actual velocity inside the media which decreases velocity by the magnitude of pleat factor.

$$PF=\frac{Total\ face\ area\ of\ MFEC\ media}{Total\ cross\ sectional\ area\ of\ the\ reactor} \quad \text{(V.3)}$$

$$\frac{\Delta P}{L} =$$

$$72\frac{\tau^2}{cos^2\theta}\frac{\mu v_0}{g_c}\frac{(1-\varepsilon)^2}{\varepsilon^3}\times\left[\left(\sum\frac{x_i}{\varphi_i D_i}\right)^2+x_{FD}\sum\frac{x_i}{(\varphi_i D_i)^2}\right]\times\frac{1}{PF}+$$

$$6\frac{\tau^3}{cos^3\theta}\frac{\rho v_0^2}{2g_c}\frac{(1-\varepsilon)}{\varepsilon^3}\sum\frac{x_i}{\varphi_i D_i}\left[C_f+C_{FD}\varepsilon\right]\times\frac{1}{PF^2} \quad \text{(V.4)}$$

For pressure drop estimation by a model, two components of different diameters can be combined by the simple mixing rule of volume weighted average or surface-volume ratio weighted average [152, 155]. However, traditional mixing equations lead to large errors if there are significant differences in the dimension of the components. For the MFEC structures, diameter ratio of the fibers and the particles varied from 1:16 to 1:32. If the particle with the

diameter ratio is 1:5 and smaller particles are less than 30%, even the Blake-Kozney equation failed to estimate the pressure drop for a packed bed [151]. Therefore, pressure drop for these MFEC structures cannot be estimated by using traditional mixing equations. The PMP equation according to Eq. V.4, overestimated the pressure drop. Karwa et al. [133] has introduced an empirical correction factor to PMP equation as shown in Eq. V.5, which reduced the error in estimation. This correction factor is a function of solid fraction and diameter of the particles, and is independent of fiber diameter or ratio of fiber volume to particle volume. A detailed explanation has been discussed in the above reference. This correction factor is valid for high voidage ($\varepsilon \leq 0.99$) and for a wide range of particle size (50 – 600 μm). Therefore, the pressure drop of pleated MFEC can be calculated by Eq. V.4 and by the correction factor (Eq.V.5) as shown in Eq. V.6. The root mean square (*RMS*) error shown in Table V.4 was calculated using Eq. V.7. If the MFEC is composed of several layers, total pressure drop will be the simple summation of pressure drop created by each layer according to Eq. V.8. Furthermore, for pleated geometrical system, the entrance and exit losses require to be considered due to sudden contraction and expansion of flow while entering and leaving the pleated formation. These losses cannot be ignored for high velocity systems as these are considered as inertial losses and vary with the square of the velocity. Both of these entrance and exit losses can be generalized by Eq.V.9 where the term K_L depends on the ratio of the areas corresponding to their position.

$$Cr = \left(1.651x_p^2 - 1.357x_p + 1\right)\left[1 - 0.1x_p\left(\frac{\varphi_p D_p}{\left(\varphi_p D_p\right)_{average\ particle\ size}} - 1\right)\right] \quad \text{(V.5)}$$

$$\left(\frac{\Delta P}{L}\right)_{With\ Cr} = Cr \times \left(\frac{\Delta P}{L}\right)_{PMP\ Model} \quad \text{(V.6)}$$

$$RMS\ error = \sqrt{\frac{\sum\left(\Delta P_{model} - \Delta P_{experimental}\right)^2}{n}} \quad \text{(V.7)}$$

$$(\Delta P_{Total})_{layered\ MFEC} = \sum_{i=1}^{i=n} (\Delta P)_i \quad \text{(V.8)}$$

$$(\Delta P)_{entrance\ or\ exit\ loss} = K_L \frac{1}{2} \rho v_o^2 \quad \text{(V.9)}$$

The pleat numbers of MFEC structures and bed properties are enlisted in Table V.1. Nickel fibers used for MFEC are infinitely long cylinders with ridges on surface as shown in Fig. V.1. The shape factor for infinitely long cylinder is 1.5 and this was multiplied by 0.7 to consider the surface roughness due to the ridges on the fibers.

Table V.1: Operating conditions, parameters and bed properties used in the experiment and modeling

Operating Conditions	
Temperature (K)	473
Pressure (kPa)	101.3
Parameters	
μ (kg/m*s)	2.54×10^{-5}
ρ (kg/m^3)	0.74
Bed properties	
Numbers of pleat	1, 2, and 4
Nominal fiber diameter (μm)	8
Particle diameter (mm)	0.19
Catalyst particle sphericity, (φ_p)	0.7
Fiber sphericity, (φ_i)	1.05 (=1.5 × 0.7)

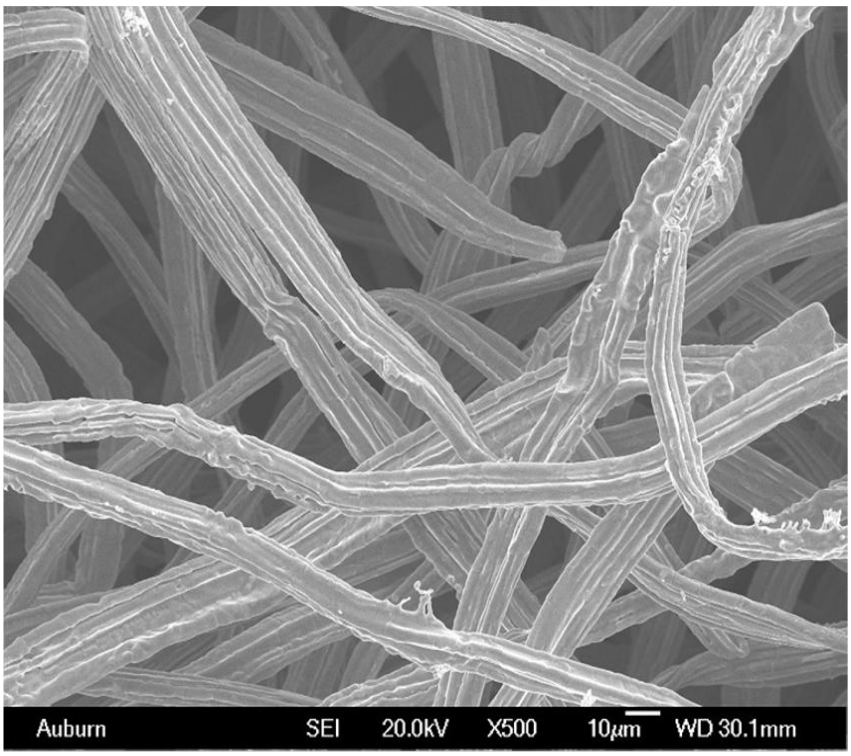

Figure V.1: SEM image of 8 µm unsintered nickel fibers

V.2.2 CFD Simulation using ANSYS FLUENT:

Computational fluid dynamics (CFD) is a powerful design tool to model complex flows around the stationary and the moving objects [113, 114]. Duggirala et al. [38] has explained in details of the pressure drop modeling in microfibrous media using CFD. ANSYS FLUENT is a state-of-the-art computer program for modeling fluid flow, heat transfer, and chemical reactions in complex geometry. It provides comprehensive modeling capabilities for a wide range of incompressible and compressible, laminar and turbulent, steady state and transient fluid flow problems. Due to the high face velocity of the system, turbulence flow model is required to be considered. For turbulence modeling in ANSYS FLUENT, standard k-ϵ and shear stress turbulence (SST) k-ω models were applied. Standard k-ϵ is the simplest complete model in which the solution of two separate transport equations allows the turbulence velocity and the length

scale to be determined independently, whereas SST k-ω is the accurate formulation of the near wall region with a free stream independence of k-ϵ in the far field region. As the turbulence model largely depends on the treatment near wall, a combination of two-layer model of enhanced wall functions is used for the near wall fine mesh. However, owing to the small dimension of fibers and particles size, Reynolds number inside the porous media is not large enough to consider as turbulent flow. Therefore, the effect of turbulence is required to be suppressed by enabling laminar zone in porous media. Pressure based solver along with the SIMPLE segregated algorithm and PRESTO as pressure interpolation scheme are appropriate for flow within the porous media structure [156]. Similarly, cell zone condition requires different treatments for the porous media, which refers to the inputs of orientation of porous media to the flow direction as the media cannot be considered as isotropic; inertial resistance factor; porous media permeability; and porosity of the media. Pressure drop across the porous media is modeled by Eq. V.10. The media properties in Eq. V.10 (α and C_2) were derived from the experimental pressure and velocity data for flat structured MFEC. Fig. V.2 shows 2D schematic diagram of pleated MFEC (numbers of pleat 2 and 4) prepared by PATRAN, which is a powerful tool to design complex geometry and mesh creation was conducted by using quadratic cell. All other boundary conditions, determined by the experimental conditions, used in ANSYS FLUENT are listed in Table V.2.

$$\frac{\Delta P}{L} = -\left(\frac{\mu}{\alpha} v_o + C_2 \frac{1}{2} \rho v_o^2\right) \tag{V.10}$$

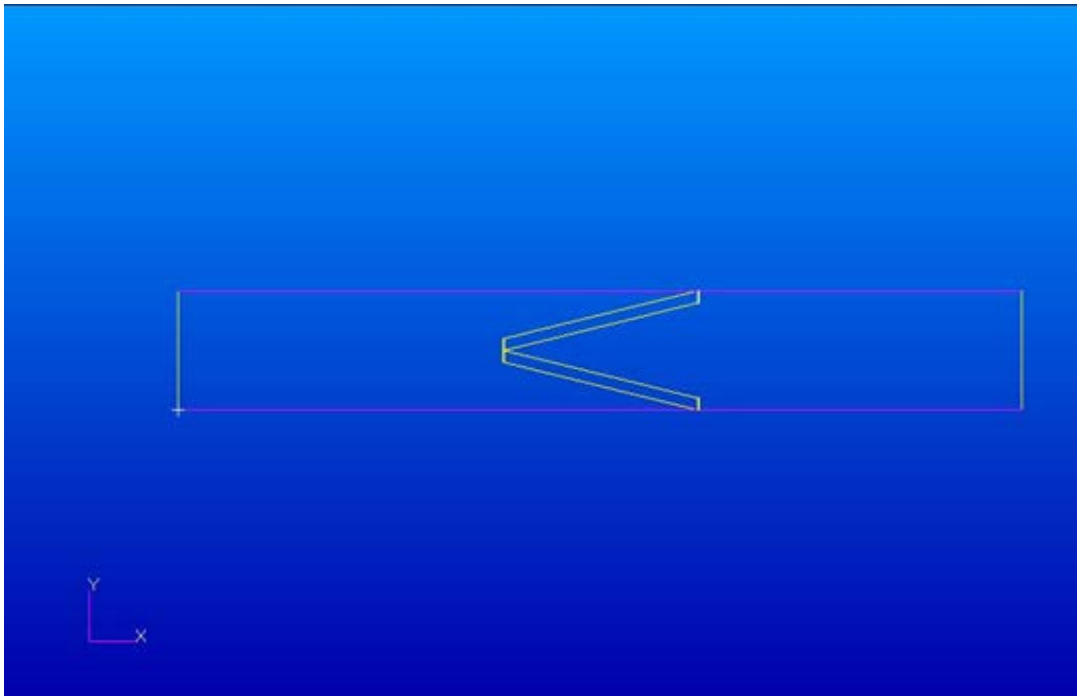

(a)

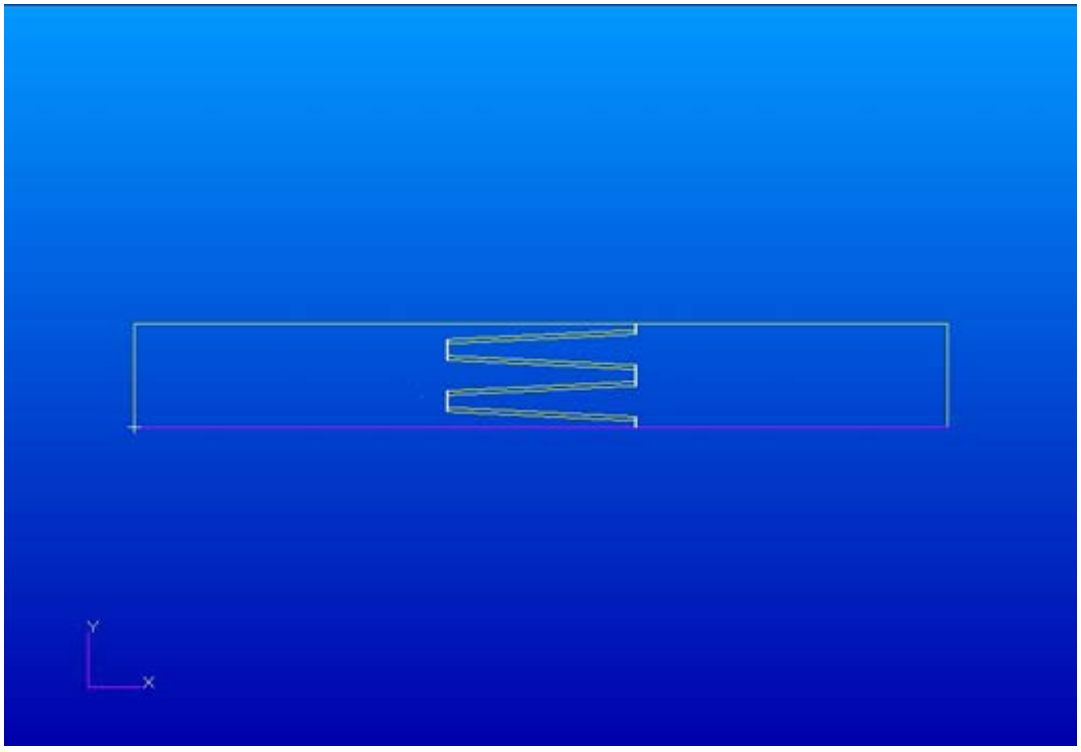

(b)

Figure V.2: Schematic diagram of pleated MFEC reactor using PATRAN (Numbers of pleat 2 and 4)

Table V.2: Applied boundary conditions and parameters for pressure drop modeling in ANSYS FLUENT

Zone	**Boundary Conditions**
Inlet	Velocity-inlet
Top and bottom wall	Wall
Pleat tip	Wall
Outlet	Pressure-outlet
Relaxation parameters	
Pressure (Pa)	0.3
Momentum (kg.m/s)	0.7
Body forces (N)	1.0
Convergence criteria	10^{-6}
Turbulent intensity (%)	4
Hydraulic diameter (in)	5

V.3 Experimental Details:

The preparation technique of MFEC is discussed in Section II.2 and in Section III.2. In this case, some of the preform was composed only with fiber and cellulose. Furthermore, the detail procedure of measuring the pressure drop is discussed in Section II.2. In this study, the thickness of the media was measured using thickness measuring device, as shown in Fig. V.3. A 2.54 cm diameter of MFEC sample was collected from the main media sheet and was placed underneath the pressing bench. The weight on the sample was increased continuously and the thickness was measured simultaneously.

Figure V.3: Thickness measuring device

V.4 Results and Discussions:

Fig. V.4 shows the effect of applied force and velocity equivalent to the applied force on media thickness for different dimensions of fiber media containing same amount of particles and fiber weight, and fiber only. For each sample, applied weight was increased continuously. As the nickel fibers are malleable in nature, the voidage of media decreases due to compression, which thereby reduces the media thickness. According to Eq. V.4, thickness of the media plays a significant role in pressure drop measurement. From this plot, it can be inferred that thickness of the media in pleated structure varied with velocity because of the pressure corresponding to the

high face velocity exerted on it. Hence, the media in pleated structures was compressed and the voidage changed. Fig.V.4 helped to measure the thickness at various applied pressures corresponding to the face velocities ran into the system. This measured thickness was applied in modified PMP equation to calculate pressure drop. As evident from the graph, the rate of thickness reduction was higher initially which declined gradually with the increase in applied force and it followed the same trend regardless of the fiber dimensions. However, further increase in applied force would not have change the thickness of the media.

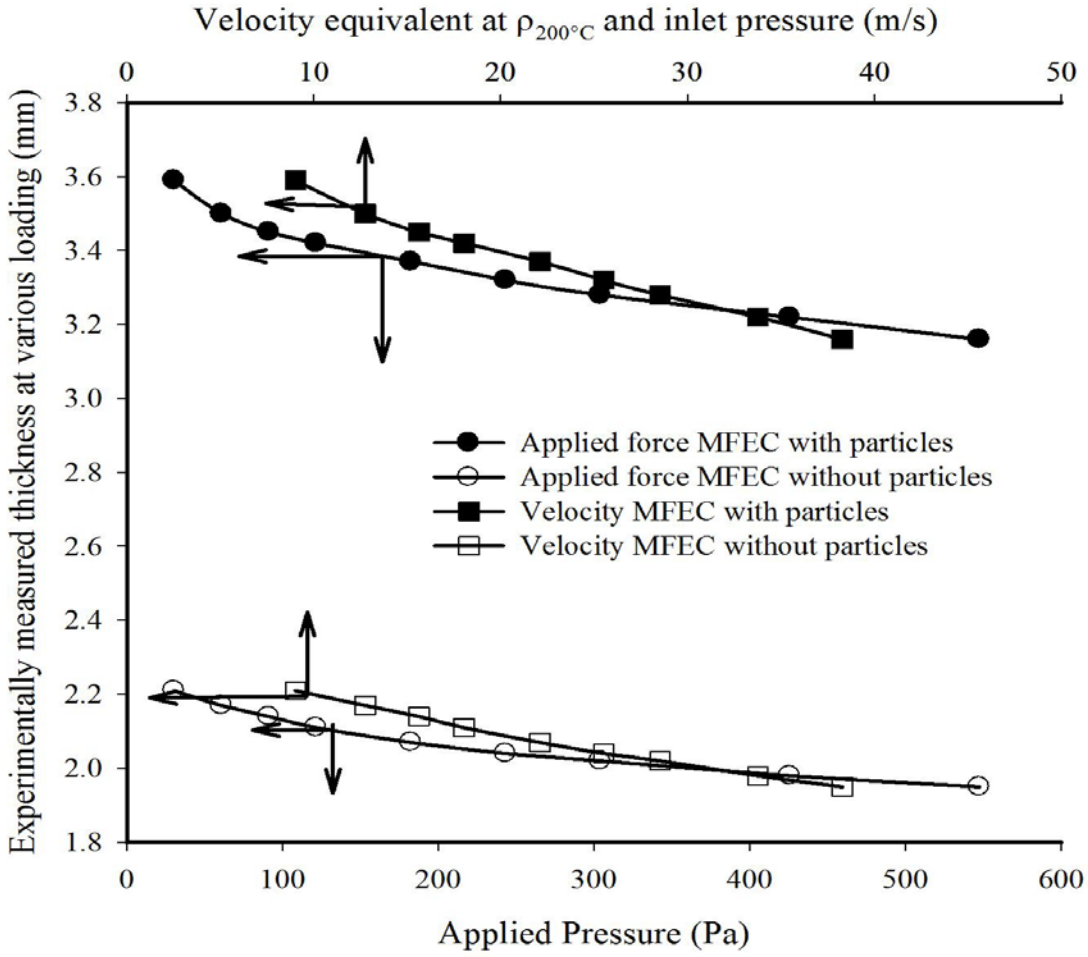

Figure V.4: Media compressibility at various gas velocities and applied pressure

V.4.1 Comparison among Modified Porous Media Permeability Equation, Computational Simulation and Experimental Findings:

Fig. V.6 and V.7 show the comparisons of the pressure drops calculated by modified PMP equations (Eq. V.4 and Eq. V.6, respectively) and those obtained from the experiments at 473 K for pleated MFEC (numbers of pleat 1, 2, and 4) designs, where the samples were prepared by the fibers only and particles entrapped into the fibers, respectively. Each MFEC sheet had same amount of fibers, particles, and thickness. The pressure drops due to packaging (Fig. V.5) were subtracted from the experimentally obtained pressure drops for all cases in order to measure those by the media only. For both types of media cases, the model predictions showed a reasonable agreement with the experimental values for number of pleat 1. The effect of dimensional heterogeneity created by the fibers and entrapped particles, induced higher pressure drop due to employing traditional mixing rule. This effect was suppressed by the introduction of a correction factor (*Cr*) in Eq.V.4. Table V.4 exhibits the effect of incorporating the correction factor in pleated PMP equation for numbers of pleat 1, 2, and 4. Each of the catalyst particles supported media had protective layers on both sides so that at high face velocity, the media would not lose any particles since the system is related to catalytic reaction occurring at short contact time. MFECs were able to provide an improved contacting efficiency as compared to the packed bed and commercial monolith regarding ozone and VOC decomposition at high gas velocities [32, 149]. During the sintering process of MFEC, the nickel fibers of these protective layers created bonds with those of supported media owing to the removal of cellulose. Pressure drops calculated by Eq. V.8 are the summation of pressure drop created by the supported media and the protective layers separately using Eq. V.6. For numbers of pleat 2 and 4, experimental values are higher than that of model predictions especially at high face velocities. Due to sudden

contraction and sudden expansion at the entrance and at the exit of the pleated formation, vortices form at their adjacent region and thereby, velocity incorporated in Eq.V.9 is not as accurate as predicted. These deviations were not taken into account during entrance and exit losses calculations. These pressure losses are not accounted by the inclusion of the PF term in the model equation, and are expected to increase proportionally with the square of the fluid velocity. This clarifies the increase in pressure drop between the experimental findings and the model predictions for numbers of pleat 2 and 4 with the increased velocity. In addition, the complex media formation may not give exact velocity magnitude and flow path angle inside the pleated media. This also attributed to the pressure drop difference between the theoretical modeling and experimental result.

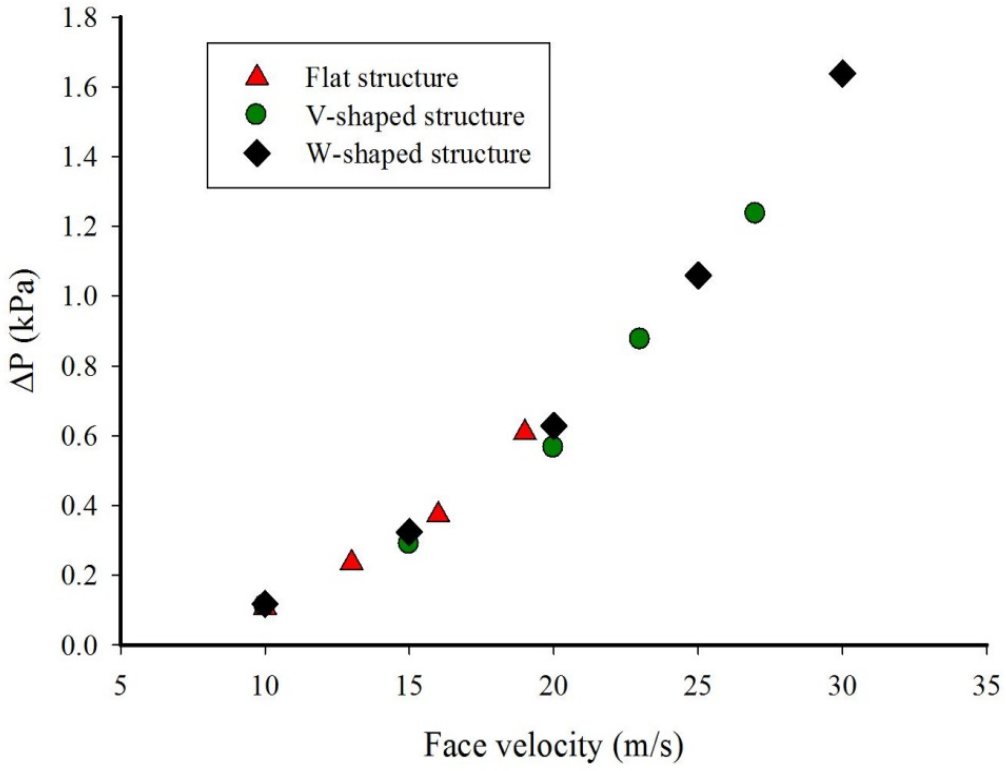

Figure V.5: Pressure drop due to packaging at various face velocities

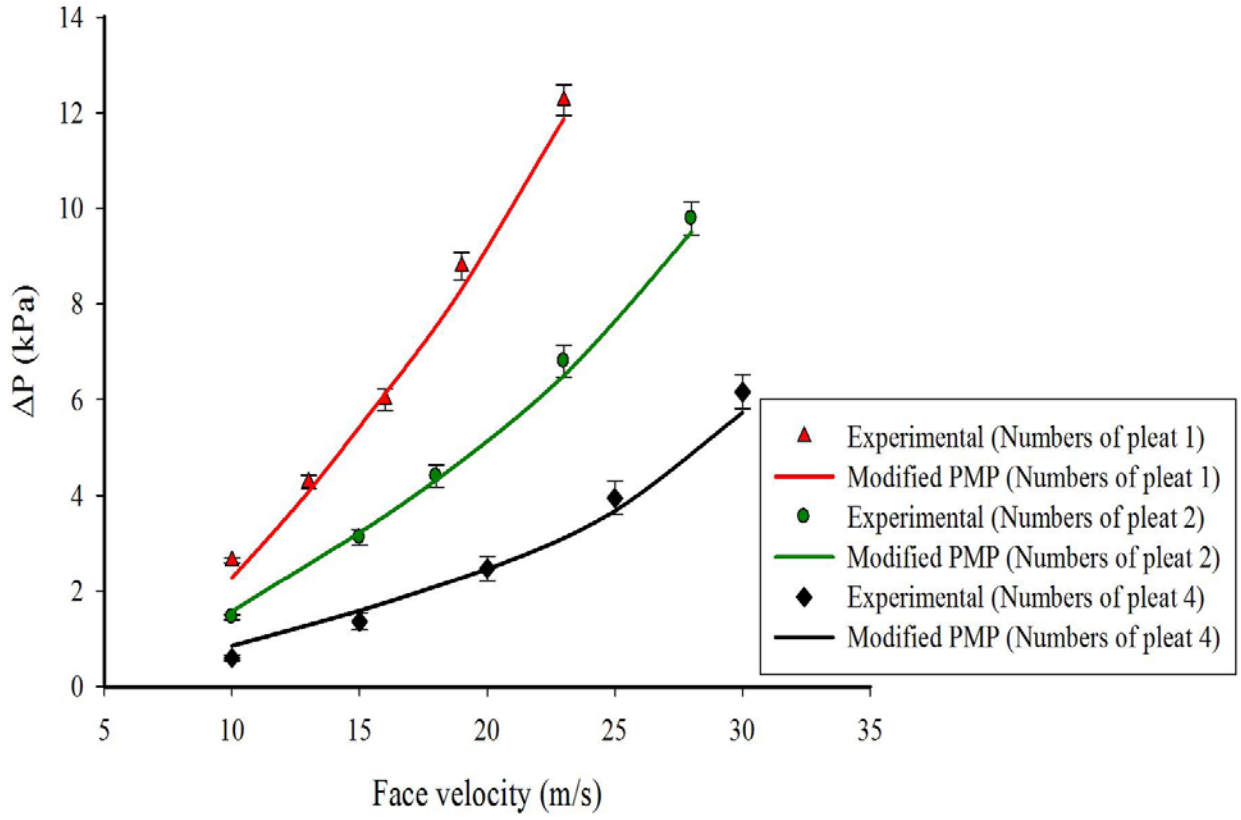

Figure V.6: Comparisons of face velocity versus pressure drop for microfibrous media (fibers only) with different pleated configurations: Experimental findings versus semi-empirical porous permeability calculations ((Flow path angle 30°)

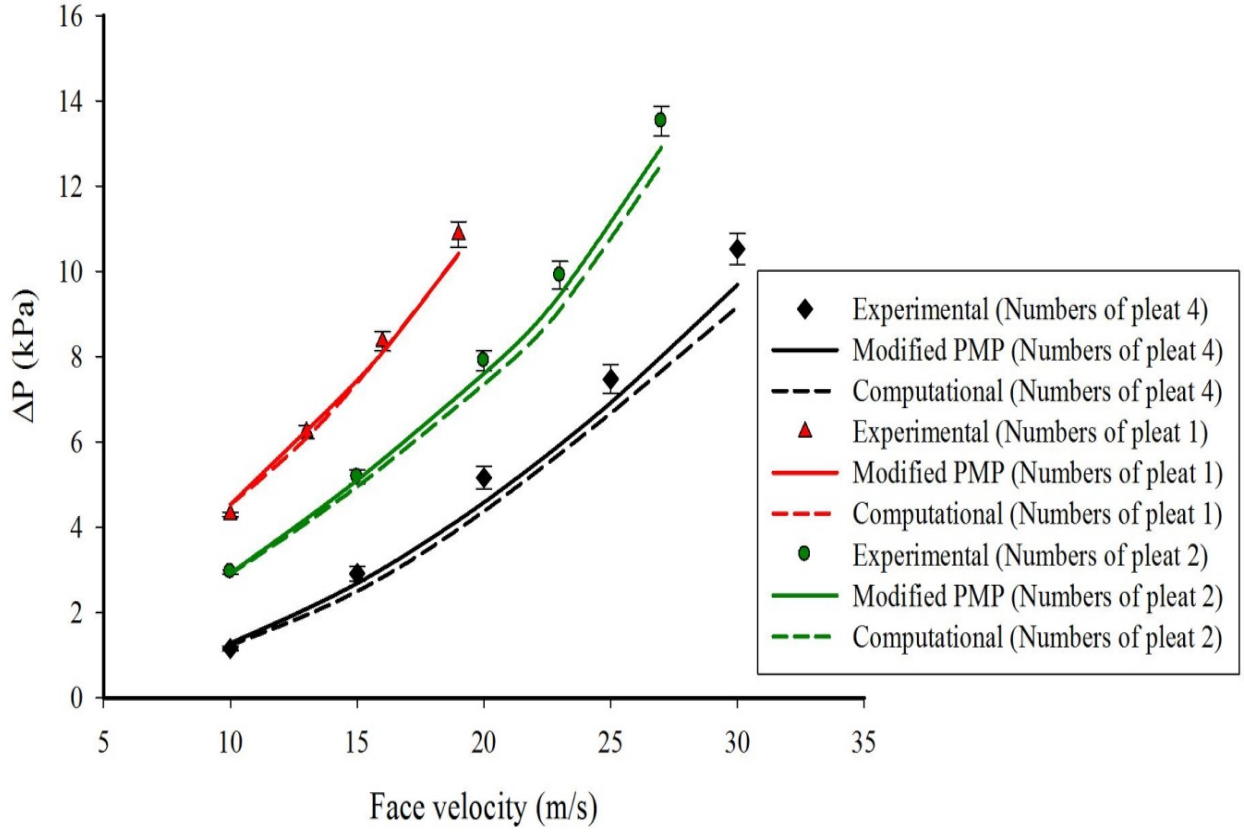

Figure V.7: Comparisons of face velocity versus pressure drop for MFEC with different pleated configurations: CFD simulations versus semi-empirical porous permeability calculations versus experimental findings (Flow path angle 30°)

Pressure drop predicted by CFD using turbulent model across the system at different face velocities for three different pleat configurations were compared with those measured experimentally. Due to the preparation procedure, the media were identical formation. As the pressure drop depends on the properties of the media, experimentally obtained data for flat structure was employed to calculate the media properties (α and C_2) of MFEC. These values were further employed for pleated structures while performing simulations. For each case, the

thickness of the media was kept constant and that was 3.6 mm. As the flow inside the media was laminar due to small characteristic dimension, the turbulence effect was suppressed inside the media during simulation. Fig. V.7 shows that model prediction exhibited reasonable agreement with the experimental measurement especially at low face velocity. The difference in pressure drop predicted by CFD and obtained from experiment at high face velocities, can be attributed for irregular particle shape, the volume blockage that is physically present, change in the media thickness (due to malleable nature) at high face velocities, medium grid formation. Furthermore, the computational model considered protective layers and supported MFEC as a single media. All these provide reasonable explanation of the differences between model predictions and experimental results. The inlet velocity and pressure of the system remained approximately same until the flow reached to the pleat tip. The pressure decreased gradually as air flowed within the porous media and there was a drastic change in pressure between the flow approaching the porous media and inside the porous media. Moreover, the sudden expansion created by the flow leaving the pleated media, caused negative pressure region adjacent to the media outlet. As evident from Fig. V.8(a) and Fig. V.8(d), the extension of vortex that enhanced the reduction of pressure abruptly created a negative pressure zone for certain distance after the media outlet. This negative pressure zone was verified experimentally as well.

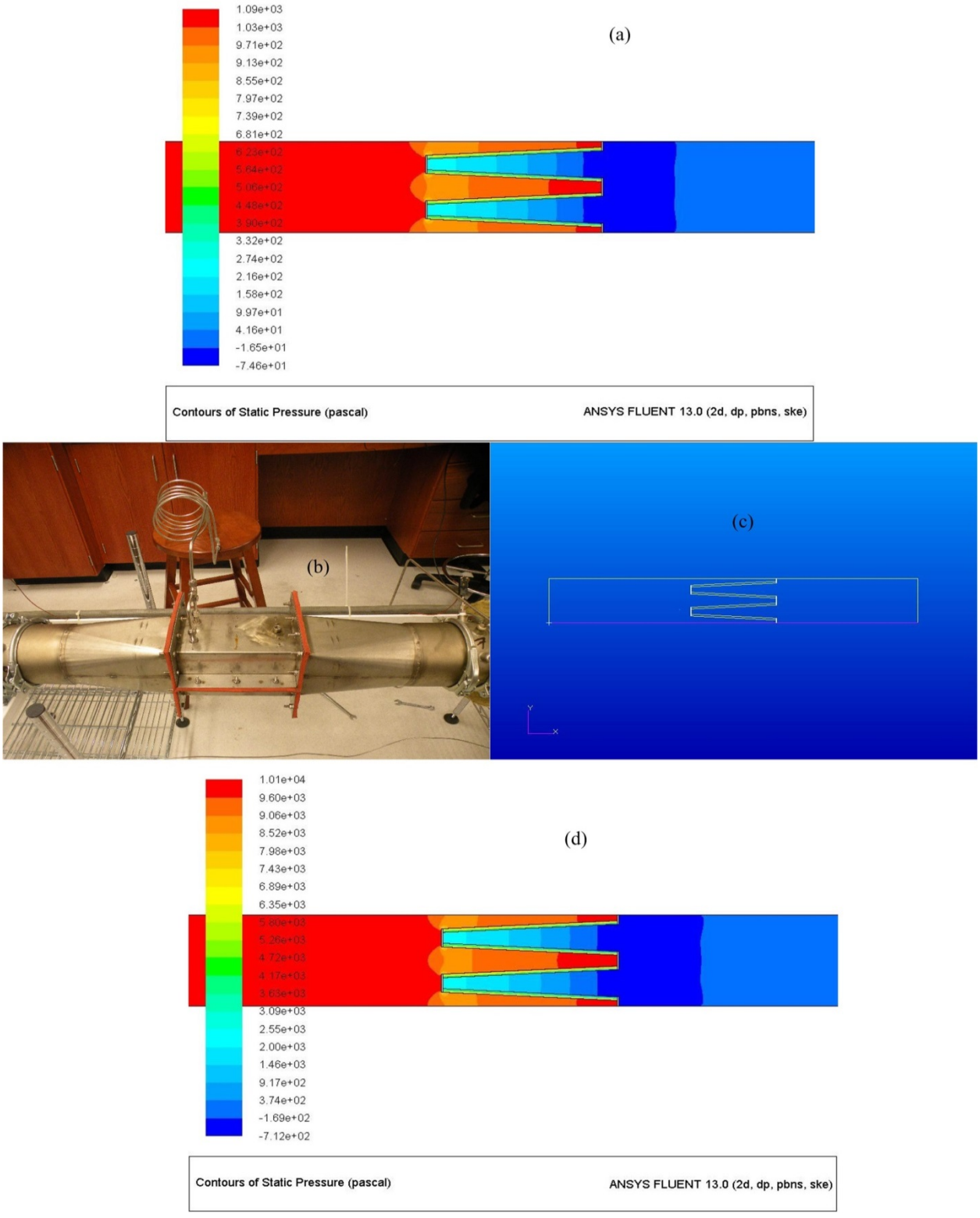

Figure V.8: (a) Contours of static pressure at 10 m/s; (b) Reactor section; (c) Schematic diagram; and (d) Contours of static pressure at 30 m/s

CFD was not only being able to predict the integral performance characteristic like the pressure drop across the system, but also local velocities within the system. Fig. V.9(a) and Fig. V.9(d) show the change in face velocities across the entire reactor length. Due to the contraction created by the pleated structure at the upstream, velocity at the adjacent area of the pleated geometry at the upstream increased. The velocity in the media reduced regularly but did not approach to zero because of the permeability of the media. As the inlet velocity increased, maximum velocity obtainable inside the system i.e. adjacent areas between pleated geometry and downstream, also increased, and this increment was higher than twice of the inlet face velocity. The velocity profile explained appropriately the formation of negative pressure zone in the system. The length of the auxiliary section had taken long enough to consider the flow as fully turbulent flow.

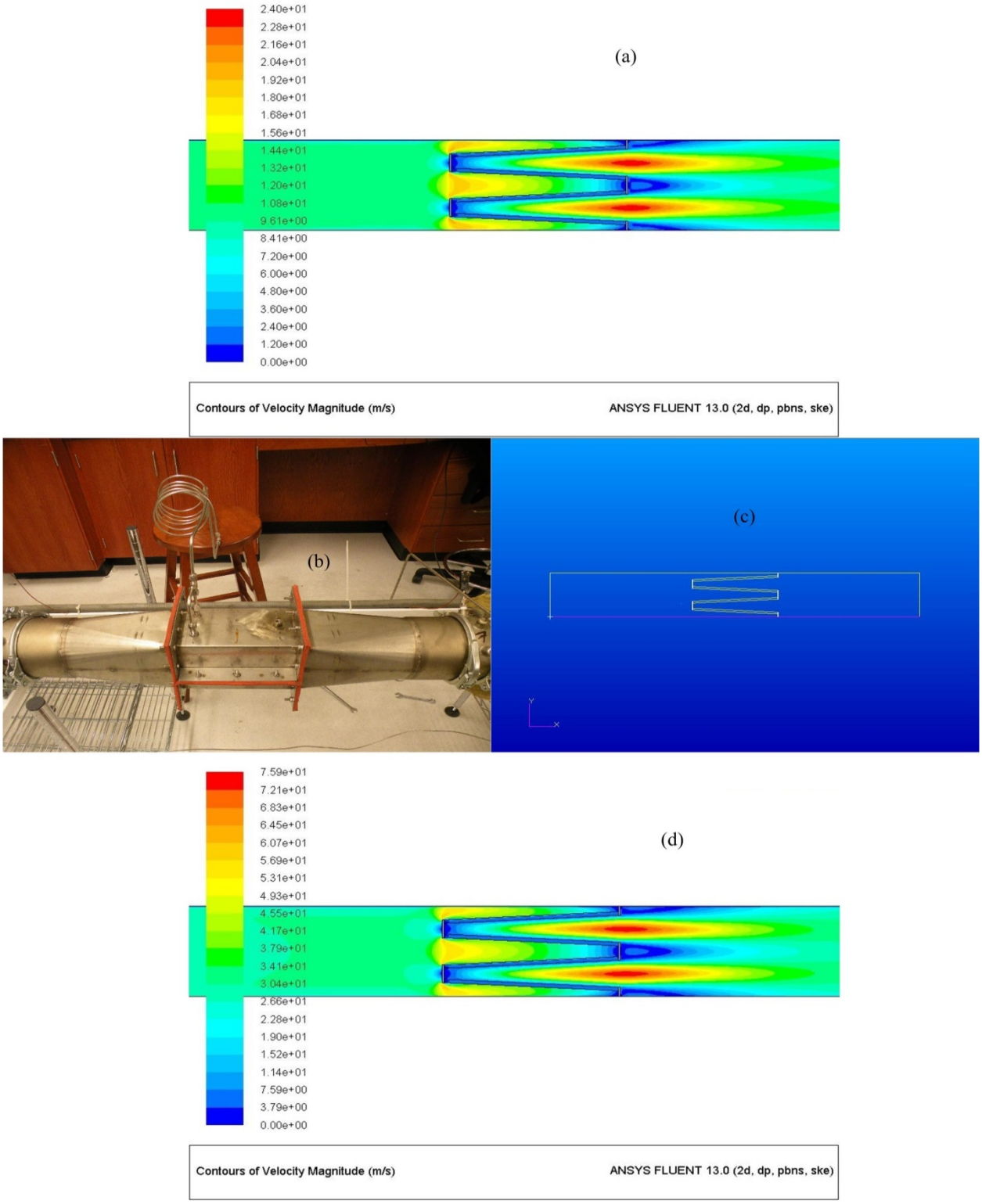

Figure V.9: (a) Contours of velocity at 10 m/s; (b) Reactor section; (c) Schematic diagram; and (d) Contours of velocity at 30 m/s

Table V.3 shows the discretization error results. This is defined by the difference between the numerical solution and the exact solution. The discretization error is the primary source numerical error in CFD simulations. The exact solution was estimated by the Richardson extrapolation [157], according to Eq. V.11. This exact solution was used to estimate the relative discretization error (Eq. V.12). The RDE values were calculated for three different pleated MFECs at their highest face velocities. In this case, the order of accuracy (p) and the grid refinement factor (r) were 2 and 2, respectively. . The estimated discretization error provides the guidance of choosing an appropriate grid. The medium grid was used for all simulations, presented in this study, which has maximum discretization error of 2.8% for the cases examined. As the values of p and r were set to 2 and 2, respectively, according to the Table V.3, the RDE values for the three different grid formation follows Eq. V.13.

$$\Delta P_{exact} = \Delta P_1 + \frac{\Delta P_1 - \Delta P_2}{r^p - 1} \tag{V.11}$$

$$RDE = \frac{\Delta P_{exact} - \Delta P_1}{\Delta P_{exact}} \times 100\% \tag{V.12}$$

$$RDE_1 = \frac{RDE_2}{4} = \frac{RDE_3}{16} \tag{V.13}$$

Table V.3: Discretization error data

Structures	Face velocity (m/s)	Grid type	No. of elements	Relative discretization error (%)
Flat	19	Fine	3,487,077	0.246
		Medium	870,796	0.984
		Coarse	160,161	3.936
V-shaped	27	Fine	3,675,270	0.320
		Medium	1,052,563	1.281
		Coarse	301,264	5.125
W-shaped	30	Fine	1,509,721	0.700
		Medium	459,443	2.801
		Coarse	139,684	11.247

Fig. V.10 shows the comparison between two turbulence models – standard k-ϵ and SST k-ω, for flat and W-shaped structure. There was no significant difference in pressure drops achieved by these two models. Both of these two models exhibited same deviation from the experimental results. This can be attributed to the high Re numbers of the system. The variables near the wall changed rapidly due to the high Re numbers. Therefore, the wall functions for the near wall region behaved similar to far field region. Pressure drops in Fig V.10 were obtained for the highest obtainable velocity in the system. However, the comparison showed similar results for the other velocities.

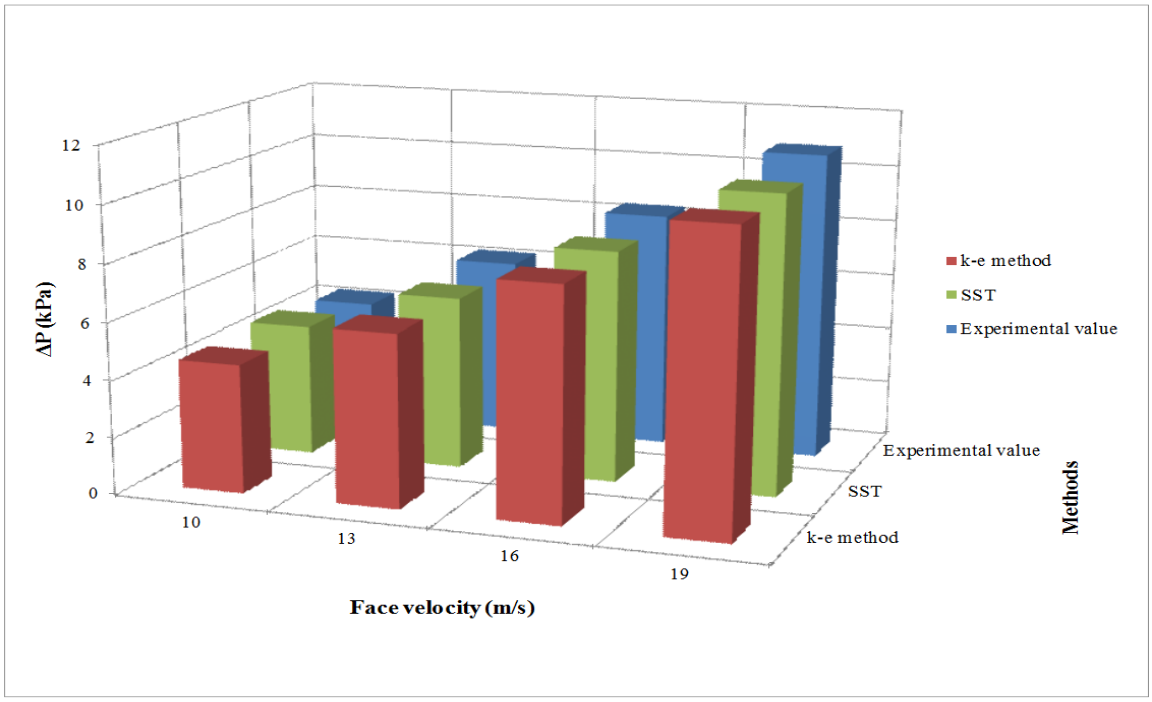

(a)

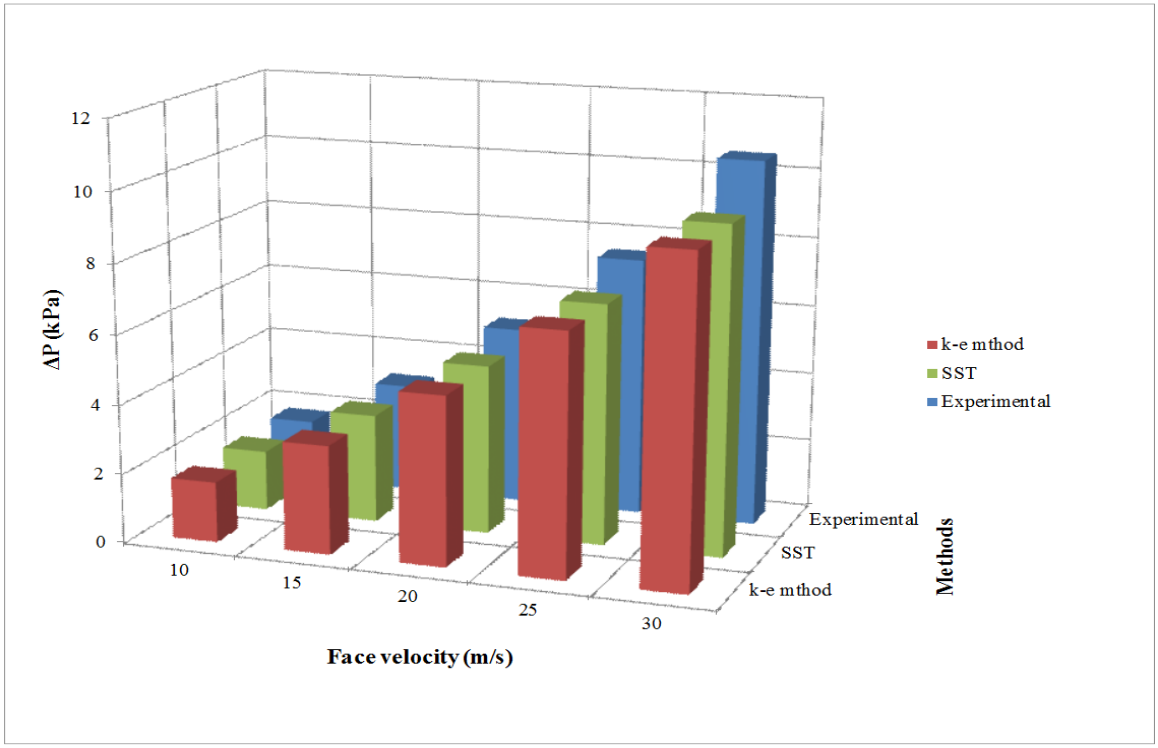

(b)

Figure V.10: Comparison between different turbulence flow models (a) for flat structure; (b) for W-shaped structure

Table V.4 shows the RMS error obtained by the theoretical modeling and the computational modeling. According to the table, CFD showed higher deviation from the experimental results than theoretical modeling. In mathematical modeling, pressure drop was estimated separately for supported media and protective layers whereas CFD considered these as a single media, which resulted different bed compositions. Furthermore, media properties that had been obtained from the experimental data of the flat structure, encountered different thickness as well as voidage for the applied forces corresponding to the gas velocities. CFD that had been performed was based on 2D model with medium grid which is a simplified form of the actual geometry. The accuracy could be increased by refining the mesh, but the additional refinement is expensive in both computational cost and solution time. The purpose of this study was to employ simulation to understand the flow behavior inside the pleated geometry. A simplified CFD simulation was conducted in this regard. Further rigorous microscopic analysis will provide the details insight in the MFEC including axial and radial distribution of pressure drops inside the porous media and will reduce the difference between experimental findings and computationally obtained data. As the implementation of CFD simulation seems very promising, our future work will be focused on rigorous utilization of CFD on the pleated structure of MFEC.

Table V.4: Calculated RMS errors for theoretical and computational modeling

Numbers of pleat	**Theoretical modeling: Difference between experimental pressure drop and pressure drop predicted by modified PMP equations**		**Computational modeling**
	With Cr	**Without Cr**	
1	0.28 kPa	1.25 kPa	0.41 kPa
2	0.44 kPa	1.95 kPa	0.74 kPa
4	0.53 kPa	2.45 kPa	0.81 kPa

In this study, the comparisons of mathematical model and computational model with experimental findings were limited to four number of pleating due to the space constriction of the reactor. Although the data have not been presented here, both of these models have been verified with different particles (250-425 μm) and fiber sizes (12 μm, mixture of 4 μm and 8 μm (1:1 wt ratio)), different amount of particles and fiber loading, and at different temperatures (373 K and 423 K).

V.5 Conclusion:

Pressure drop occurring across a reactor is an essential design criterion for process involving high mass flow rates. A semi-empirical mathematical and a computational pressure drop models were developed for predicting the pressure drop across any pleated MFEC structure. These two models have shown good agreement with the experimental findings. The effect of form drag factor and friction factor was significantly high for both losses due to the addition of irregular shaped particles into the fibers. In addition, thickness of the media changed gradually with the applied force due to the compressibility of the media. Hence, MFEC in the pleated

formation encountered different thicknesses and voidages at different face velocities. The PMP equation was modified by introducing two variables. The empirical correction factor took into account the heterogeneity created by the addition of large particles within the small sintered fiber matrix, and the PF term was used for the reduced velocities (due to the pleating) inside the MFEC. Furthermore, the computational pressure drop model used the CFD method to predict the pressure drop across a pleated MFEC structure and to predict the change in pressure along the media thickness. This method also provided a microscopic insight into the local velocities that exist inside a system as well as inside the media. Simulations were performed for flow through microfibrous media using ANSYS FLUENT. A pressure based segregated algorithm along with turbulence flow model was preferable for porous media simulation. This study has demonstrated techniques for estimating pressure drop from two different approaches—mathematically and computationally. Using these two models and the new insights, it would be possible to design better and more practical catalytic reactor systems through the use of optimized pleated MFEC configurations.

Chapter VI

Comparative Performance Study of VOC Removal in Structured Reactors: Microfibrous Entrapped Catalyst with Enhanced Contacting Efficiency

VI.1 Introduction:

Packed bed reactors and wash-coated monoliths are intended commercially as catalytic reactors for these applications [11, 12, 35, 36]. However, packed beds result higher pressure drops and monoliths cause low fluid-solid mass transfer rates and non-uniform fluid distribution, which causes lower reactor effectiveness. Monolith reactors were initially developed and applied in mid 1970s for the automotive industry as vehicle engine mission converters to remove NO_x, CO and hydrocarbons through gas-solid reactions. Compared to the traditional packed bed catalysts used for gas phase reactions, monolith offered much lower pressure drop, which obviously was very advantageous in this application. Beyond the low pressure drop, the application of the monolith results in high selectivity, elimination of hotspots, and improving catalyst effectiveness factor. However, wash-coated monolith causes low radial heat transfer rate and non-uniform fluid distribution. These complications cause difficulty in temperature control and low reactor effectiveness, respectively. Furthermore, installation of monolith in industrial scale is difficult and expensive as well. Considering these disadvantages of monolith reactors, microfibrous entrapped catalyst (MFEC) can be an innovative approach in the industrial applications for catalytic reaction. Sheng et al. [33] has shown uniform temperature distribution or fine temperature control by MFECs in highly exothermic and highly endothermic reaction systems. Kalluri et al. [32] has investigated the mass transfer rates of different reactors i.e., packed beds, monoliths and MFECs, of different geometries where MFECs have shown improved performance over packed beds and commercial monolith reactors.

In this study, catalytic VOC (e.g., ethanol) removal at high mass flow rates was performed to demonstrate and to understand the advantages of pleated MFEC structures. In this study, for theoretical comparison, packed bed of different particle sizes, monoliths of various CPSI (cells per square inch), and MFEC with various pleat numbers were used to investigate the effect of various reactor geometries on pressure drop and on mass transfer. A performance evaluation parameter, heterogeneous contacting efficiency (η_{HCE}), was introduced to evaluate the performance of those above mentioned reactor geometries. This parameter relies on the logarithmic removal of reactant concentrations per unit of pressure drop. Experimental ethanol conversion and pressure drop tests were also conducted to verify the theoretical findings. However, the experimental comparisons were restricted only to monolith and MFEC considering the practical difficulties of construction and testing of packed beds with the existing apparatus and operating conditions of the experiments. Furthermore, a reaction kinetic model was established for pleated MFEC in order to investigate the reaction kinetics in the velocity controlled region.

VI.2 Mathematical Modeling

For theoretical performance comparison, packed bed of various particle sizes, wash-coated monolith of different CPSI, and pleated MFECs were considered. In this section, the mathematical models, to illustrate the mass transfer and momentum transfer in various reactor geometries, and the performance evaluation criteria are presented. Ethanol removal is a highly exothermic reaction, however due to the low concentration involved in this research; no significant temperature rise is expected in the reactor even for complete ethanol removal. Furthermore, the reactor *Pe* values were considerably high (*Pe* > 10) due to the high face

velocity involved in this process. This indicates to the isothermal plug flow condition [63]. The molecular diffusivity (D_m) of ethanol in air was estimated using Fuller's method as shown in Eq. VI.1 [158]. All the other gas properties considered in this study are based on the operating conditions.

$$D_m = \frac{0.00143T^{1.75}}{PM_{AB}^{1/2}\left[(\sum v)_A^{1/3}+(\sum v)_B^{1/3}\right]^2} \quad \text{(VI.1)}$$

The pressure gradient occurring across packed beds, monoliths and MFECs can be described by a general equation, as shown in Eq. VI.2, where f is the friction factor and d_c is the characteristic length, specific for each reactor type. The characteristic length (d_c) for packed beds and MFECs is equal to the effective particle diameter ($\varphi_p d_p$) whereas for monoliths it is equal to the channel diameter (d_{ch}). Based on the operating conditions and various reactor geometries, different correlations for the friction factors and gas-solid mass transfer coefficients (or Sh) are considered in this section.

$$-\frac{\Delta P}{L} = \frac{1}{2} f \frac{\rho v_o^2}{d_c} \quad \text{(VI.2)}$$

VI.2.1 Packed bed

Packed bed, which is essentially a tubular reactor, is usually packed with solid structured or un-structured catalyst particles. For theoretical comparison various particle diameters were considered for packed beds, as listed in Table VI.1. The smallest particle size in packed beds is similar to that of MFEC catalyst which enables a head to head comparison between packed bed and MFEC performance. Ergun equation [94] was used for the friction factor calculation which is applicable for voidage less than 0.5.

$$f = \left(150\left(\frac{1-\varepsilon_b}{Re_p}\right) + 1.75\right)\left(\frac{1-\varepsilon_b}{\varepsilon_b^3}\right) \quad \text{(VI.3)}$$

Gas-solid mass transfer coefficients or Sh values for packed bed were obtained using Thoenes-Kramers correlation [63]. It is a semi-empirical correlation to estimate the Sh value for flow through a packed bed. This equation is valid for $0.25 < \varphi_p < 0.5$, $40 < Re_p/\varphi_p(1-\varepsilon_b) < 4000$, and $1 < Sc < 4000$. The Re_p and the bed voidage for the packed bed cases used in this study are within the limit of Ergun equation and Thoenes-Kramers correlation.

$$Sh = \frac{(1-\varepsilon_b)^{\frac{1}{2}}\varphi_p^{\frac{1}{2}}}{\varepsilon_b} Re_p^{\frac{1}{2}} Sc^{\frac{1}{3}} \quad \text{(VI.4)}$$

The intra-particle transport rates for packed bed were estimated using the following effectiveness factor correlation (Eq.VI.5) which involves Thiele modulus. The relation between the effectiveness factor and the Thiele modulus indicates the diffusion and reaction limitation phenomena.

$$\eta = \frac{1}{\Phi}\left(coth(3\Phi) - \frac{1}{3\Phi}\right) \quad \text{(VI.5)}$$

$$\Phi = \left(\frac{\varphi_p d_p}{6}\right)\sqrt{\frac{k_r}{D_e}} \quad \text{(VI.6)}$$

For all the reactor geometries compared, the effective diffusivity of ethanol inside the catalyst support followed Eq.(VI.7) with $\tau_p = 2.5$ and $\varepsilon_p = 0.82$. These values of intra-particle tortuosity and porosity resemble to the γ-Al_2O_3 particles used in the experiments.

$$D_e = D_m \frac{\varepsilon_p}{\tau_p} \quad \text{(VI.7)}$$

Table VI.1: Properties of the packed bed

Particle diameter, d_p (mm)	0.19, 0.5, 2.0
Sphericity (φ_p)	0.7
Void (vol.%)	40
Catalyst (vol.%)	60

VI.2.2 Monolith

Wash-coated monoliths provide a number of advantages over traditional pellet-shaped catalyst and thus, are now widely used in environmental applications [11, 12, 35, 36, 82]. Various monoliths are compared in this study. Their structural properties are listed in Table VI.2. The values of wall thickness and cell densities are equivalent to the monoliths used in the experiment. Only square channel monoliths were considered here. Any other channel shape is expected to show similar trend to that observed in this study.

The correlation for estimating pressure drop in a wash-coated monolith, is shown in Eq. VI.8 [11]. This considers apparent Fanning Friction factor.

$$f_F = \frac{13}{\varepsilon_b Re_{ch}} \qquad for \frac{Re_{ch}}{\varepsilon_b} < 1000 \tag{VI.8}$$

$$= \frac{0.03}{\varepsilon_b^{1.88} Re_{ch}^{0.12}} \qquad for \frac{Re_{ch}}{\varepsilon_b} > 1000$$

There are many correlations and theoretical equations available in literature for estimating gas–solid mass transfer coefficients for monoliths [11, 80, 159, 160]. As square channeled monolith was employed in this study, Tronconi and Forzartti correlation was applied [80].

$$Sh = 2.967 + 8.827\left(\frac{1000}{Gz}\right)^{-0.545} exp\left(\frac{-48.2}{Gz}\right) \quad \text{(VI.9)}$$

The internal effectiveness factors for wash-coated monolith were calculated based on Eqs. VI.10 and VI.11 [161]. For theoretical comparison, the catalyst wash-coat density was assumed to be the same as that of particle density of γ-Al_2O_3.

$$\eta = \frac{tanh(\Phi)}{\Phi} \quad \text{(VI.10)}$$

$$\Phi = t_c\sqrt{\frac{k_r}{D_e}} \quad \text{(VI.11)}$$

Table V1.2: Properties of the monolith

Cells per square inch (CPSI)	230	400
Wall thickness, t_w (0.001 in./μm)	8/203	6.5/165
Catalyst washcoat thickness, t_c (μm)	12.5	12.5
Channel diameter, d_{ch} (mm)	1.422	1.054
Void (vol.%)	72.13	68.89
Catalyst (vol.%)	3.484	4.685

VI.2.3 MFEC

The bed properties and the pleat numbers of MFEC structures used in the theoretical comparisons are listed in Table VI.3. These values of bed properties were taken from those of the experimentally tested structures. Nickel fibers those used for MFECs, are infinitely long cylinders with ridges on the surface. The shape factor for infinitely long cylinder is 1.5 and this was multiplied by 0.7 to account the surface roughness because of the ridges on the fibers. As mentioned before, MFEC can be easily pleated. Therefore, pleat factor (*PF*), a term frequently

used with MFEC system, is defined by Eq.VI.12. As a result of pleating, gas velocity decreases inside the MFEC. Hence, Kalluri et al. [32] has incorporated the *PF* term in the porous media permeability equation to correct the actual velocity inside the media. The actual velocities are the system velocities divided by the *PF* term. This value for monoliths and packed beds is always equal to one, as they cannot be pleated.

$$PF = \frac{Total\ face\ area\ of\ MFEC\ media}{Total\ cross\ sectional\ area\ of\ the\ reactor} \tag{VI.12}$$

For determining the friction factor in the pleated MFEC, modified porous-media permeability equation [162] was used. This equation is applicable for a multiparticulate bed with voidage as high as 0.99. The applicability of this equation for MFEC has been verified by the authors [13, 37, 133, 154, 162]. The detailed derivation of these equations (Eqs.VI.13-VI.15) and the significance of each term have been discussed in the above mentioned references.

$$C_D = \frac{30}{Re_p} + \frac{67.289}{e^{5.03\varphi}} \tag{VI.13}$$

$$f = \left\{72\left[\left(\sum \frac{x_i \varphi_p d_p}{\varphi_i d_i}\right)^2 + x_{FD} \sum x_i \left(\frac{\varphi_p d_p}{\varphi_i d_i}\right)^2\right] \frac{(1-\varepsilon_b)}{PFRe_p} + 3\frac{\tau_b}{cos\theta}\frac{1}{PF^2}\left[C_f + C_{FD}\frac{\varepsilon_b}{4}\right]\sum\left(\frac{x_i \varphi_p d_p}{\varphi_i d_i}\right)\right\}\frac{(1-\varepsilon_b)}{\varepsilon_b^3}\frac{\tau_b^2}{cos^2\theta} \tag{VI.14}$$

$$Cr = (1.651x_c^2 - 1.357x_c + 1)\left[1 - 0.1x_c\left(\frac{\varphi_p d_p}{(\varphi_p d_p)_{average\ particle\ size}} - 1\right)\right] \tag{VI.15}$$

In order to predict the *Sh* value in MFECs, the Peffers's model (Eq. (16)) was applied [163], which is applicable for low *Re* number and high *Pe* number. The reason for applying this equation was because it considers the bed voidage. Similar to the friction factor equation

(Eq.VI.14), *PF* term was also introduced in this equation. Thoenes-Kramers correlation for packed bed is not applicable for high voidage bed like MFECs.

$$Sh = 1.26\left(\frac{1-\gamma^5}{W}\right)^{\frac{1}{3}}\left(\frac{Re_p}{PF}Sc\right)^{\frac{1}{3}} \quad \text{(VI.16)}$$

The fibers in the MFECs enhance the fluid flow distribution between the particles that results an improved mass transfer rates. The Re_p for higher pleat number will be of greater interest in this study. The pleated formation and small characteristic dimension of MFECs reduced the *Re* numbers and caused laminar flow inside the media although the system velocity was significantly high. In this study, the flow inside the pleated MFEC was laminar with very little lateral mixing caused by the fibers. The effect of fibers on mass transfer rates was studied by using computational fluid dynamics simulations and was found to be insignificant for low *Re* [39]. Hence, the presence of the fibers was neglected in mass transfer calculation for MFEC, except for bed voidage calculations.

Table VI.3: Properties of the MFEC

Numbers of pleat	1, 2, and 4
Nominal fiber diameter, d_f (μm)	4, 8, and 12
Particle diameter, d_p (mm)	0.19
Catalyst particle sphericity, φ_p	0.7
Fiber sphericity	1.05 (= 1.5 × 0.7)
Catalyst (vol.%)	11.1
Metal (vol.%)	2.2
Void (vol.%)	86.7

VI.2.4 Reaction Kinetics

The gas phase differential equation for reactant A in any plug flow reactor is given by Eq.VI.17.

$$-\frac{v_o}{PF}\frac{dC_A}{dx} = k_m x_c(1-\varepsilon_b)(C_A - C_S) \quad \text{(VI.17)}$$

The mass transfer rate to the catalyst surface in the above expression (Eq.VI.17) should be equal to the surface reaction rate inside the catalyst. The reaction follows first order reaction kinetics according to Fig.VI.6.

$$k_m(C_A - C_S) = \eta k_r C_S \quad \text{(VI.18)}$$

k_{eff} is the effective reaction rate per unit volume of catalyst, is defined by Eq.(20). The balance among Eqs. VI.17-VI.19 results Eq. VI.20. Integration of Eq.VI.20 gives the result shown in Eq. VI.21. In this study, a conversion comparison was made between the theoretical findings and the experimentally obtained data for various reactor geometries.

$$\frac{1}{k_{eff}} = \frac{1}{k_m} + \frac{1}{\eta k_r} \quad \text{(VI.19)}$$

$$-\frac{v_o}{PF}\frac{dC_A}{dx} = k_{eff} x_c(1-\varepsilon_b)C_A \quad \text{(VI.20)}$$

$$Conversion = 1 - exp\left[-k_{eff} x_c(1-\varepsilon_b)\frac{L}{v_o/PF}\right] \quad \text{(VI.21)}$$

VI.2.5 Performance Evaluation Criteria: Heterogeneous Contacting Efficiency

An important objective of this work was to investigate the performances among various reactor geometries at high face velocities for catalytic applications. Many performance features,

for example, pressure drop, chemical conversion, amount of catalyst utilization, cost of construction, catalyst life, etc., would be involved in evaluating the overall performance of a reactor system [39]. Since it is difficult to define one single parameter which will consider all these above mentioned features, chemical conversion and pressure drop across the reactor were considered in this study. Considering these two aspects the present author introduced a parameter, heterogeneous contacting efficiency (η_{HCE}) [149], which is defined in Eq. VI.22. A detailed explanation of this parameter has been provided in above mentioned reference.

$$\eta_{HCE} = \frac{1}{2}\rho v_o^2 \frac{log\left(\frac{C_{Ai}}{C_{Ao}}\right)}{-\Delta P} \tag{VI.22}$$

For a first order reactor kinetics, maximum conversion is attainable when the reactor is operated in a complete gas-solid mass transfer controlled regime [160], i.e., $C_{As} = 0$. Integration of Eq.VI.17 results in Eq.VI.23.

$$log\left(\frac{C_{Ai}}{C_{Ao}}\right) = k_m x_c (1-\varepsilon_b)\left(\frac{L}{v_o/PF}\right) \tag{VI.23}$$

Substitution of Eq.VI.2 for pressure drop and Eq.VI.23 for log reduction of concentration, converts Eq.VI.22 to the following,

$$\eta_{HCE} = \frac{k_m x_c d_c (1-\varepsilon_b) PF}{f v_o} = \frac{Sh x_c d_c (1-\varepsilon_b) PF}{f ReSc} \tag{VI.24}$$

VI.3 Experimental Procedure:

MFEC was prepared in the similar fashion as mentioned in Section III.2. In this case, amount of Ni fiber and γ-Al_2O_3 was 12.5 g and 30 g, respectively. The properties MFEC bed has been shown in Table IV.1. A detailed description of incorporating metal catalyst in MFEC has been mentioned in Section III.2.

For experimental comparison, ceramic honeycomb (Applied Ceramics) of 230 and 400 CPSI was used for the catalyst preparation. The support particles were loaded onto the ceramic substrate by sol-gel technique [164-168]. In this case 1:2:5 (wt.) of urea, 0.3M HNO_3 and boehmite (CATAPAL B, Sasol) were used. The substrate was immersed into the solution for 5 min followed by the removal of the excess solution by flowing air through the substrate. The substrate was dried at 393 K and subsequently calcined at 773 K for 6 hr. These steps were continued until 30 g support was loaded onto the substrate which possessed equal amount pore volume as the MFEC possessed. The wash-coated monolith was then impregnated by $Pd(NO_3)_2$ and $Mn(NO_3)_2$ solution. These were subsequently dried and calcined at the same temperature as conducted for MFEC. This monolith had equal amount of metal which matches MFEC contained.

VI.4 Results and Discussion

VI.4.1 Theoretical Comparison

Fig.VI.1 shows a plot of volumetric mass transfer coefficients versus superficial velocity for various reactor geometries. As discussed before, k_m is the maximum attainable reaction rate constant for a given geometry and operating conditions. In this comparison, the temperature was equal to 473 K for all reactor geometries. As evident from the plot, mass transfer coefficients in monolith is significantly lower than that of packed beds as well as MFEC which indicates one of the major disadvantages of monolith i.e., low fluid-solid mass transfer rates. With the decrease in particle sizes of the packed beds, particle surface area increased. This increment in surface area increased the rate of mass transfer in packed bed. For MFEC, k_m value decreased with increasing pleat number, although all cases of MFECs had same particle size and bed composition. The

reason was the decrease in effective velocity inside the MFEC with increasing pleat number. As MFEC had higher voidage than packed bed, this affected negatively the gas-solid mass transfer coefficients. Therefore, MFEC had lower mass transfer rate than that of packed bed of same particle size (0.19 mm).

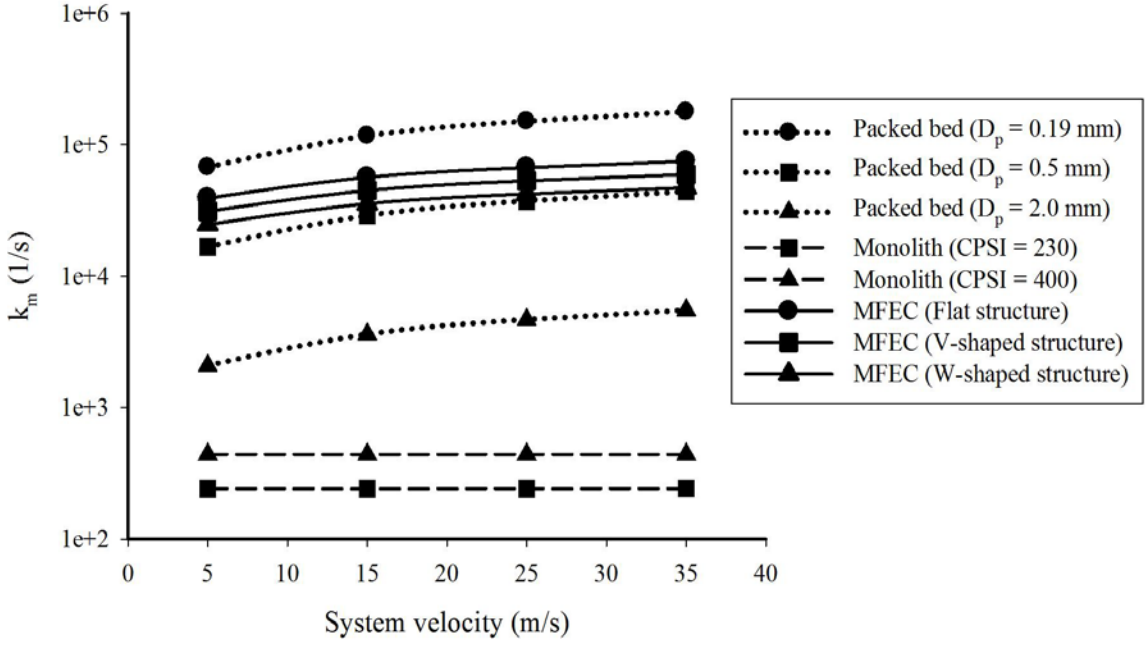

Figure V1.1: Volumetric mass transfer versus system velocity for different catalytic structures

Fig.VI.2 illustrates the comparisons of heterogeneous contacting efficiency (η_{HCE}) versus velocities for various reactor geometries. According to the plot, packed bed showed poor η_{HCE} values as compared to the monolith and MFEC. In spite of the high fluid-solid mass transfer rate in the packed bed of small particle size, the small particles had resulted significantly high pressure drop across the bed as compare to the monolith and the MFEC. Therefore, this high

pressure drop had resulted low η_{HCE} values for packed beds. However, an increase in particle sizes improved the performance. Therefore, in various catalytic applications, monolith is preferable than packed bed. For the monoliths, the η_{HCE} improved with increasing cell density. However, the variations in η_{HCE} values for packed bed of different particle sizes and monolith of different cell densities were in relatively narrow range. For MFEC with number of pleat 1, the performance was slightly better than packed beds but was significantly lower than the monoliths. The reason was high pressure drop across the MFEC. This flat shaped MFEC exhibited characteristic similar to the packed bed of same particle size. However, η_{HCE} values increased with the increase in pleat numbers and were better than the monoliths. The reason was decreased effective velocity inside the MFEC for higher pleat numbers. This decreased velocity reduced the pressure drop accordingly. Furthermore, this decreased velocity resulted higher intra-layer residence time which enhanced ethanol conversions.

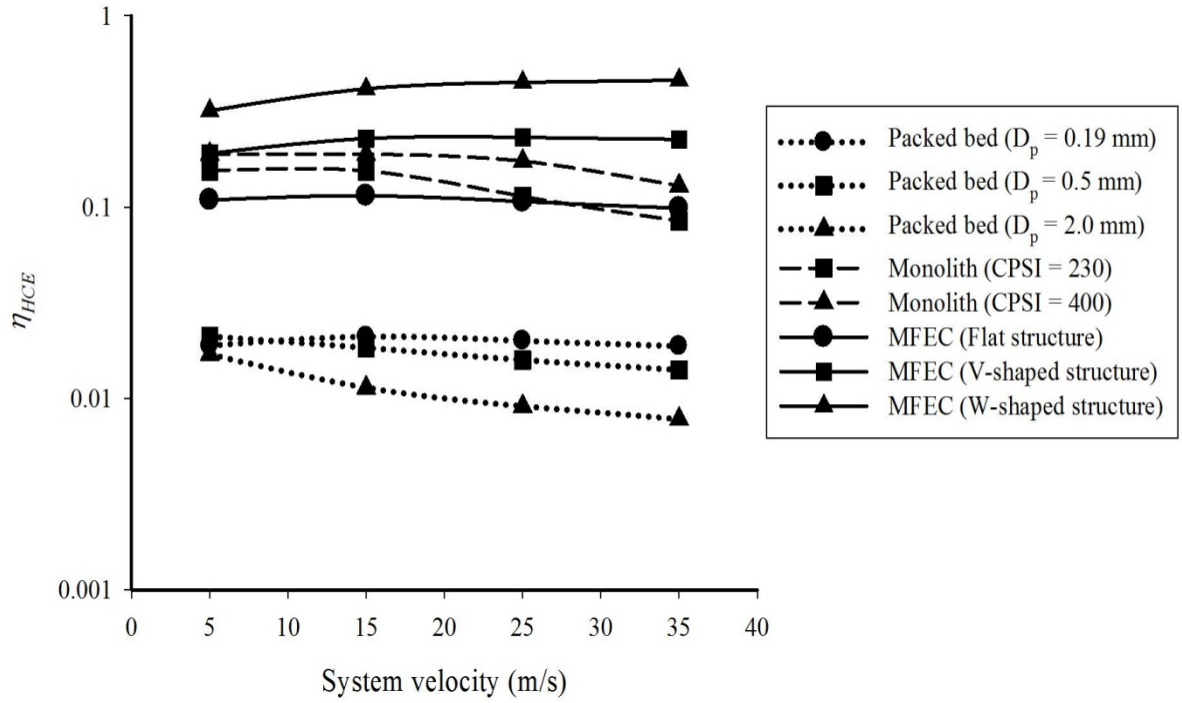

Figure VI.2: Heterogeneous contacting efficiency versus system velocity for different catalytic structures

There are many pressure drop and mass transfer correlations available in the literature for different fixed bed types and operating conditions. The choice of these correlations used in this study was based on the operating conditions, bed properties, *Re*, and *Sc*. A different correlation might slightly change the values i.e., k_m, f, and η_{HCE} but would not significantly alter the η_{HCE} value trends obtained in this study.

In this study, the comparisons of MFEC were limited only to packed beds and monoliths. The η_{HCE} value for catalytic foam lies between 0.1 and 0.3 for wide range of *Re* [168]. Based on these values and Fig.VI.2, it can be concluded that catalytic foams are better than flat shaped MFEC. But MFEC designs with pleat number greater than 2 can perform better than catalytic foams.

VI.4.2 Experimental Comparison

Fig.VI.3 shows experimentally obtained pressure drops at different velocities for various reactor formations. The construction and operation of the packed beds considered in this theoretical study, may not be feasible in practice for the operating conditions (velocity used and mobile settings) used in this application, as this would require construction of extremely thin (≤ MFEC thickness) packed beds for keeping the pressure drop sufficiently low. Therefore, packed bed cases were included only in theoretical comparative study. The plot exhibits that higher pressure drops occurred across the monolith of high cell density. For MFEC, an increase in pleat number reduced the pressure drop due to the deceased effective velocity inside the media. Experimental pressure drop occurring across different reactor geometries showed the following order: Flat shaped MFEC > V-shaped MFEC > 400 CPSI monolith > 230 CPSI monolith > W-shaped MFEC. In this study, pleat number was restricted to 4, although this value can be raised further. However, a further raise in pleat number might negatively affect the advantages of pleating.

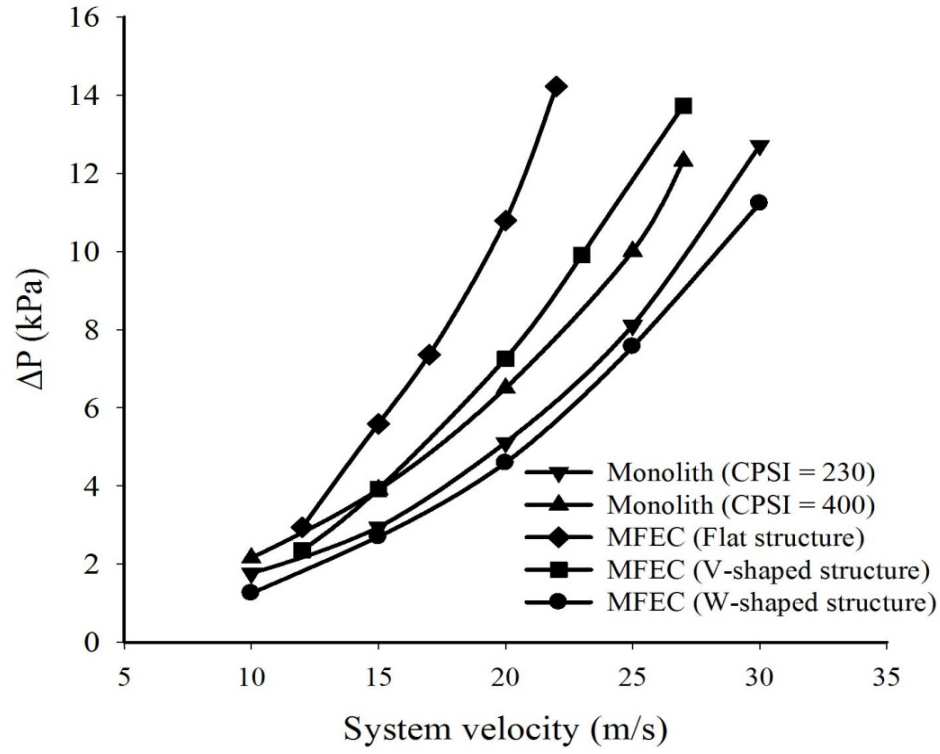

Figure VI.3: Experimental pressure drop occurring across different catalytic structures for various system velocities

The experimental ethanol conversion comparison among MFECs of flat-shaped and W-shaped design and monolith of 400 CPSI are shown in Fig.VI.4. In all cases, the total amount of metal loading and the operating conditions were kept constant. For both flat shaped and W-shaped MFECs, the thickness of the media was constant. Conversions for all cases decreased with the increase of face velocities. These high gas velocities indicated low intra-layer residence times inside the catalytic structure which had resulted short contacting reaction. The low conversion for all cases can be attributed to the fact that overall reaction rates were limited by surface reactions as the compounds diffuse through the pore mouth of the catalyst rapidly. Furthermore, the system temperature (< 473 K) was not high enough for the ethanol to undergo complete removal due to the limitations in the design of the present test apparatus. However, a

change in operating conditions would not alter the reactivity order of different geometries which is as follows: W-shaped MFEC > 400 CPSI monolith > 230 CPSI monolith > flat shaped MFEC.

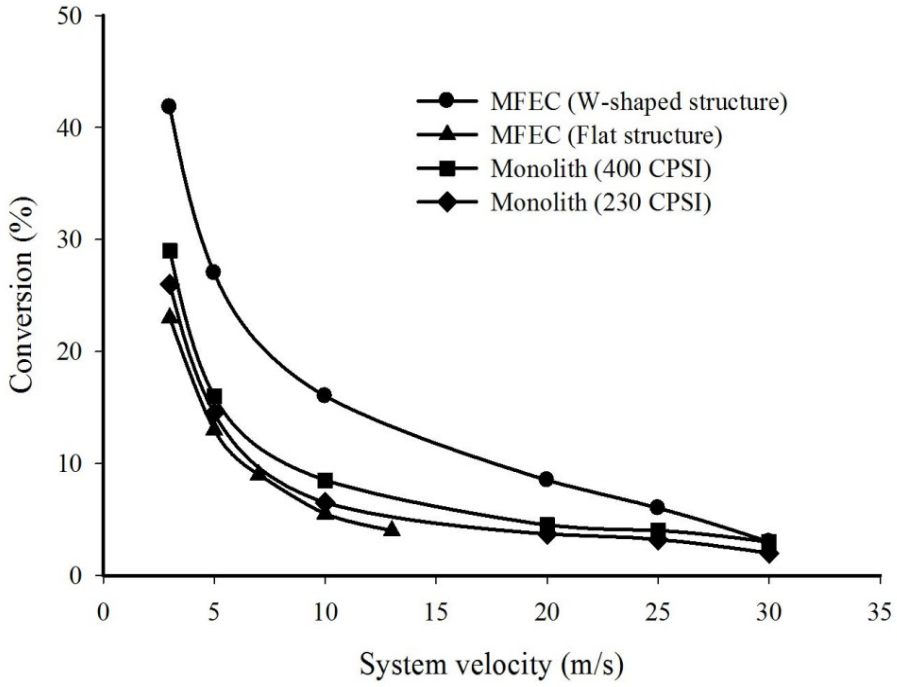

Figure VI.4: Ethanol conversion versus system velocity using different catalyst structures

Based on the experimental pressure drop and ethanol conversion data, the η_{HCE} value was calculated using Eq.VI.22. As in both pressure drop and conversion study, W-shaped MFEC performed better than the other geometries, the same result reflected in Fig. VI.5. This contacting efficiency order supported the theoretical result as well. In both theoretical and experimental study, the W-shaped MFEC showed improved performance than the wash-coated monolith and conventional packed bed in terms of pressure drop, ethanol removal and mass transfer rates. For designing a catalytic structure, pressure drop across reactor and chemical conversion are important criteria considering the energy requirement per pass of contaminant removal.

Therefore, the heterogeneous contacting efficiency can be a preferable parameter for performance evaluation.

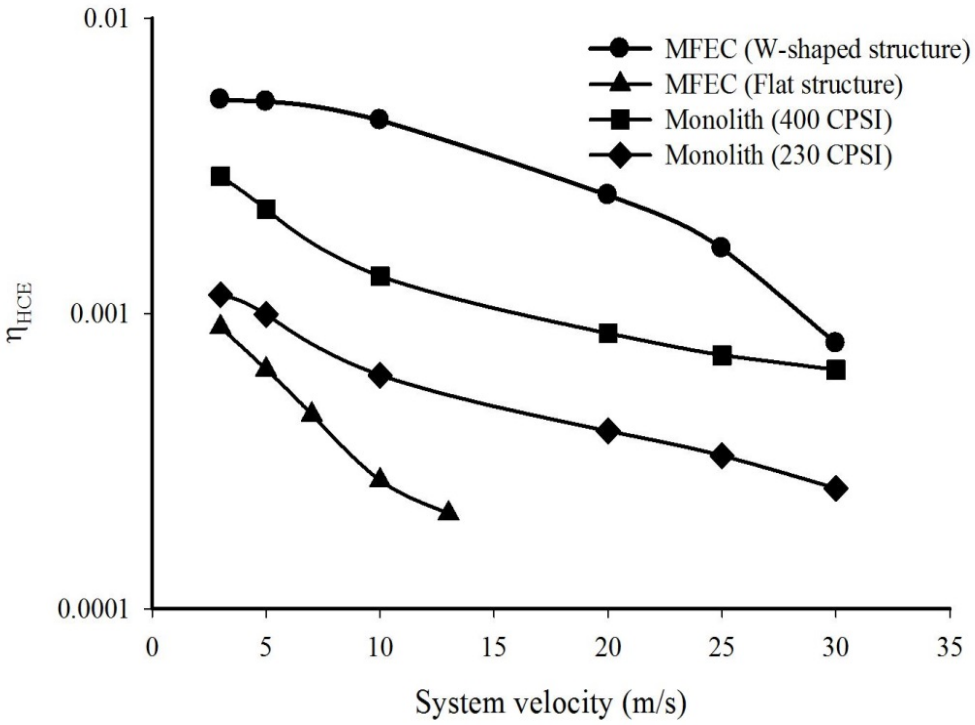

Figure VI.5: Experimentally obtained heterogeneous contacting efficiency for different catalytic structure at different system velocities

VI.4.3 Kinetic Modeling:

Fig VI.6 shows the relationship of the rate of reaction with inlet ethanol concentration. The assumption was that all the tested VOC would follow the same order of reaction. According to Mar-Van Krevelen mechanism, the order of reaction is a function of both VOC and O_2 concentration. However, O_2 concentration is essentially constant in this study. Therefore, the rate of reaction primarily depends on the VOC concentration. According to this figure, the reaction followed first order rate of reaction.

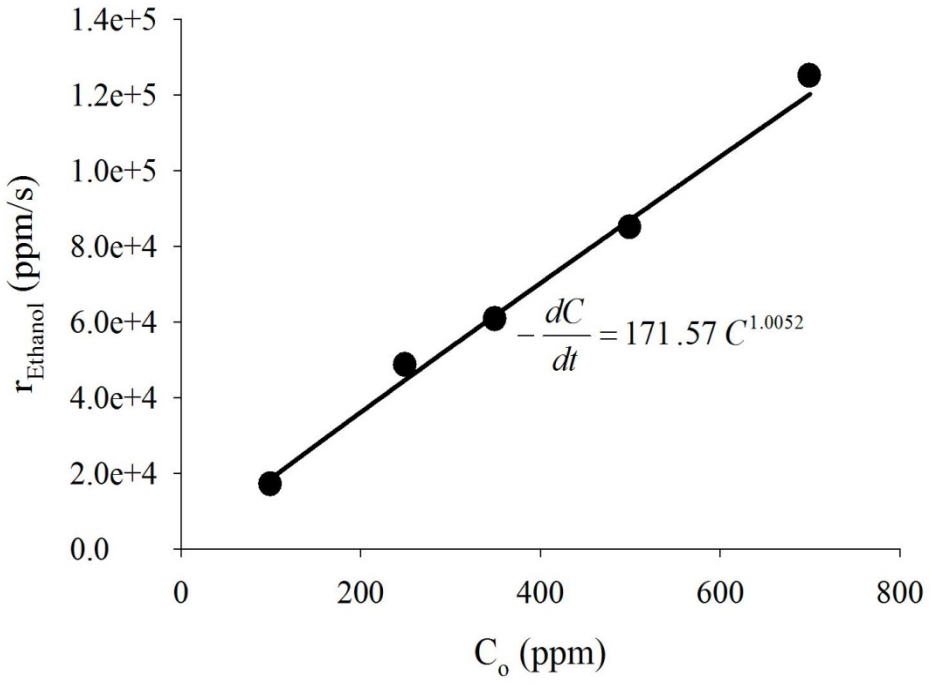

Figure VI.6: Rate of reaction versus inlet concentration for ethanol

Fig. VI.7-VI.15 show the comparison between the model predicted conversions and the experimental conversions of VOCs for flat-shaped and W-shaped MFECs, and wash-coated monolith, respectively based on the kinetic study discussed in Section VI.2.4. The model predictions are in reasonable agreement with the experimental values for flat structures. For W-shaped structure, the experimental values differ from the model predictions. This difference can be attributed to the actual velocity inside the media and the change in media thickness due to the media compressibility. As the nickel fibers are malleable in nature, the voidage of media decreases due to compression, which eventually reduces the media thickness. Voidage and media thickness play significant roles in conversion measurement according to Eq.VI.19. Furthermore, due to the pleated formation, vortices might form at the entrance of the structure. As discussed before, during actual velocity (inside the MFEC) calculation by the inclusion of *PF* term, these

vortices were not taken into account which might result slight difference in actual velocities. These explain the difference between the model predicted conversions and the experimental conversions for the W-shaped MFEC. For the monolith, the model predictions are in reasonable agreement with experimental values, as shown in Fig.VI.12-VI.14 because a well-established mass transfer correlation was used for reaction kinetics based on the operating conditions.

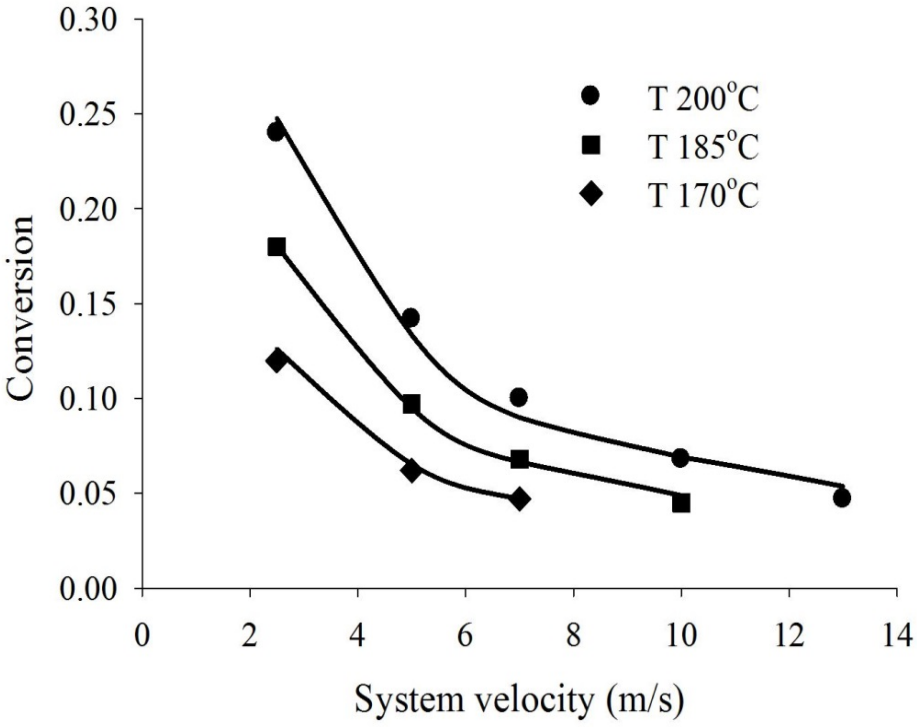

Figure VI.7: Comparison between model prediction and experimentally obtained ethanol conversion at different system velocities using flat structure of MFEC

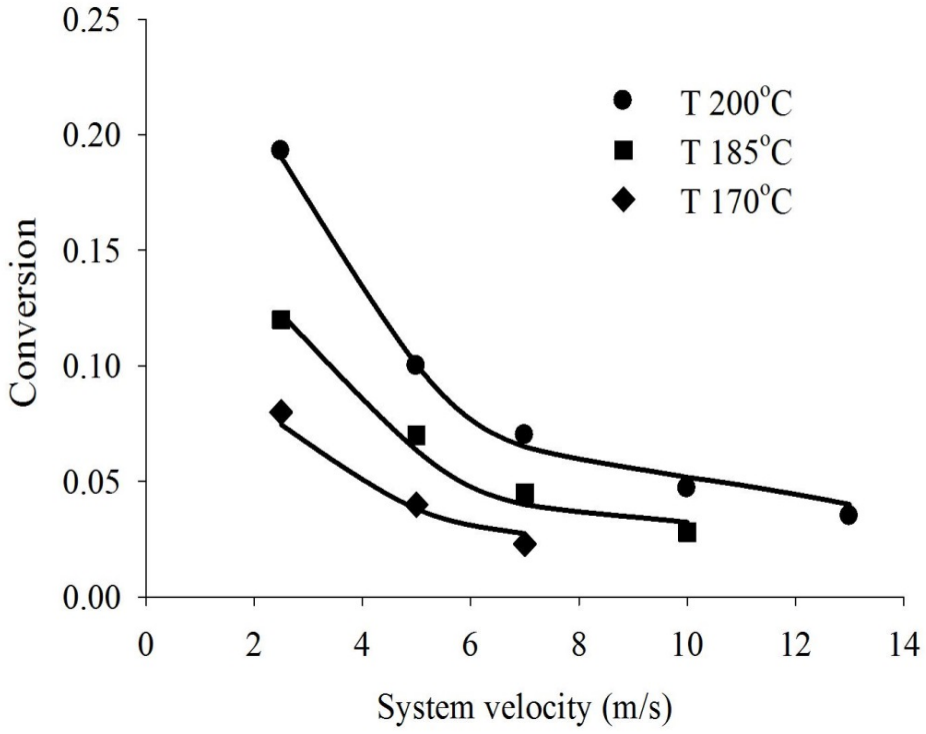

Figure VI.8: Comparison between model prediction and experimentally obtained toluene conversion at different system velocities using flat structure of MFEC

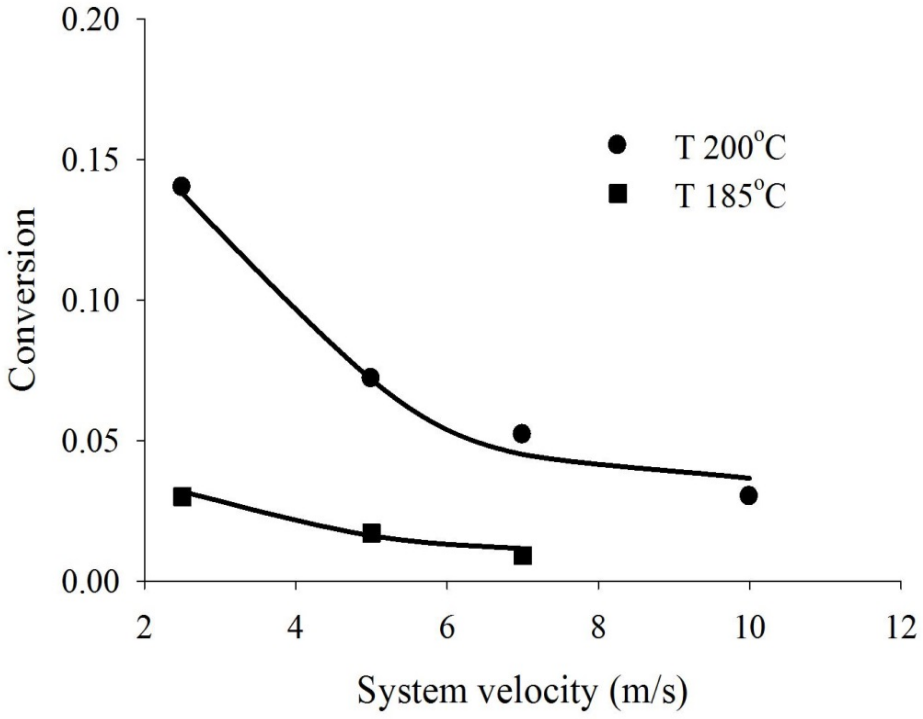

Figure VI.9: Comparison between model prediction and experimentally obtained toluene conversion at different system velocities using flat structure of MFEC

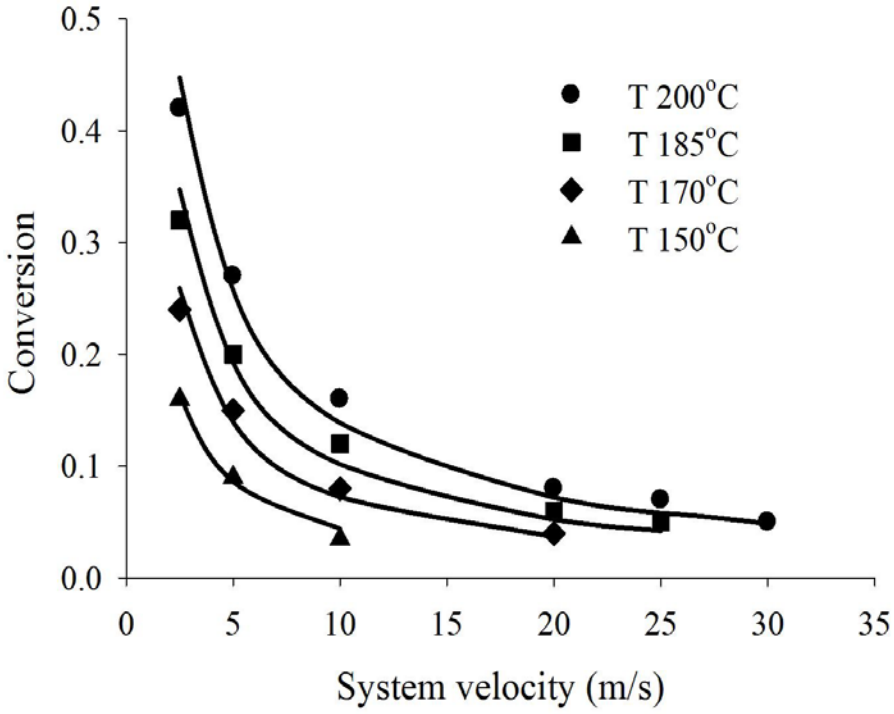

Figure VI.10: Comparison between model prediction and experimentally obtained ethanol conversion for different system velocities using W-shaped structure of MFEC

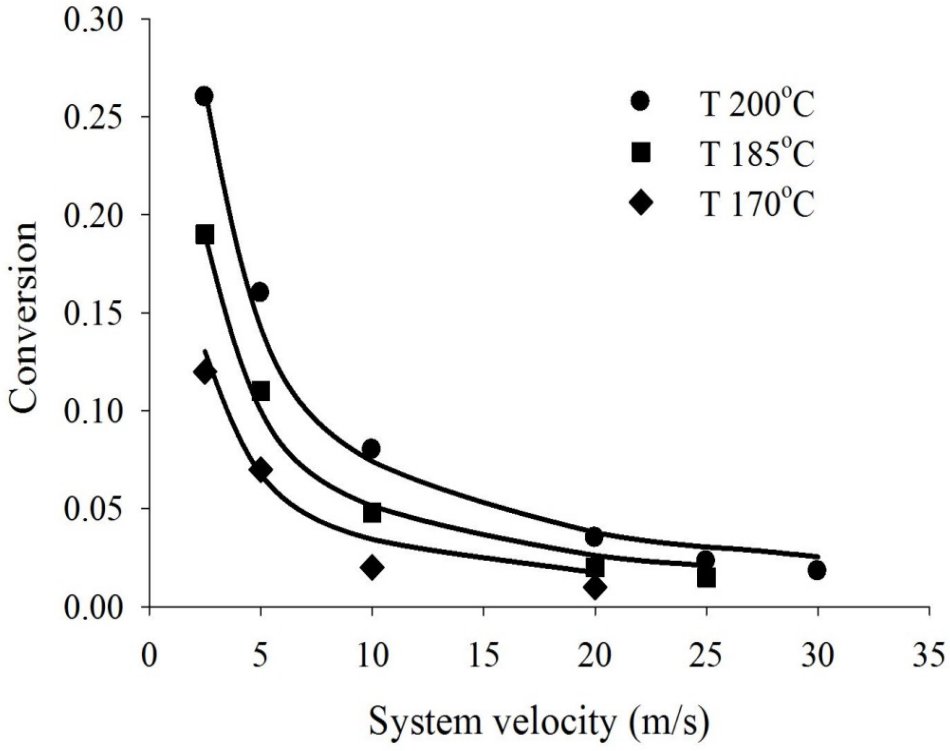

Figure VI.11: Comparison between model prediction and experimentally obtained toluene conversion for different system velocities using W-shaped structure of MFEC

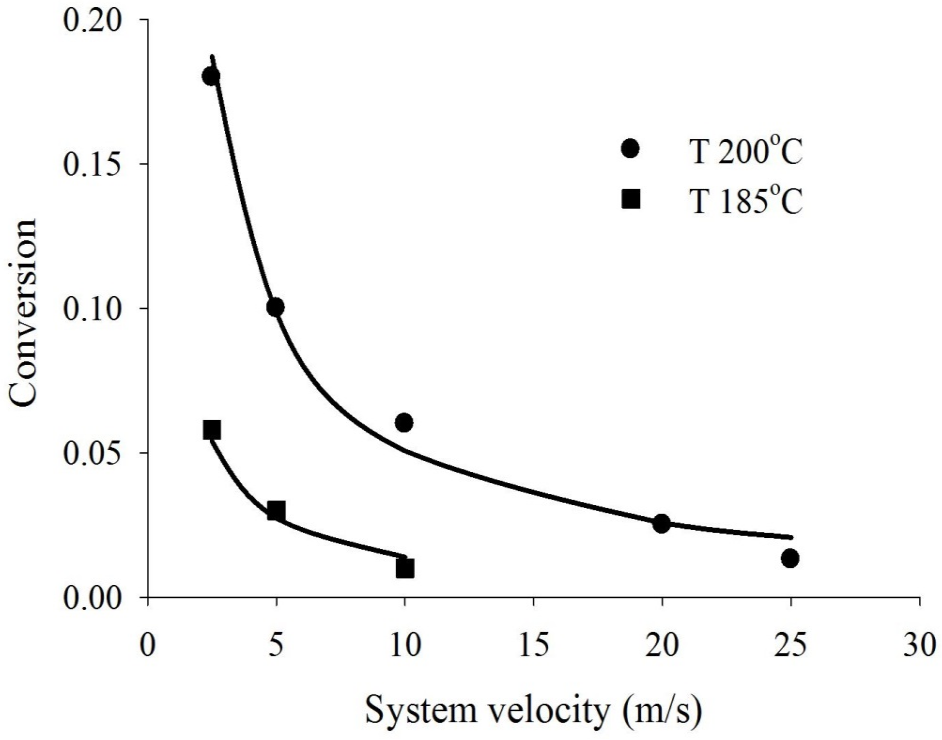

Figure VI.12: Comparison between model prediction and experimentally obtained n-hexane conversion for different system velocities using W-shaped structure of MFEC

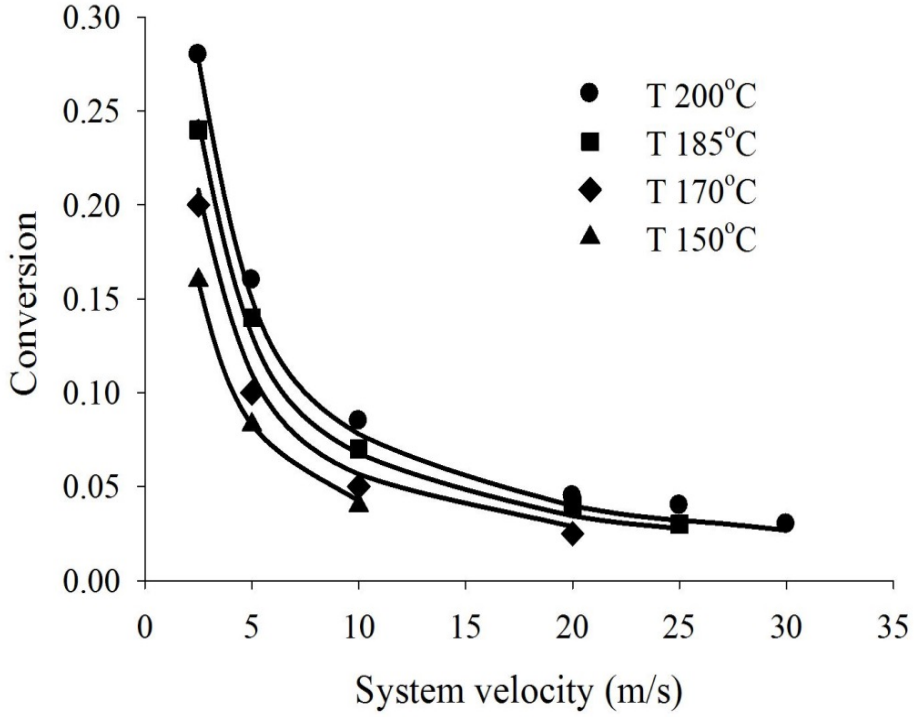

Figure VI.13: Comparison between model prediction and experimentally obtained ethanol conversion at different system velocities using wash-coated monolith

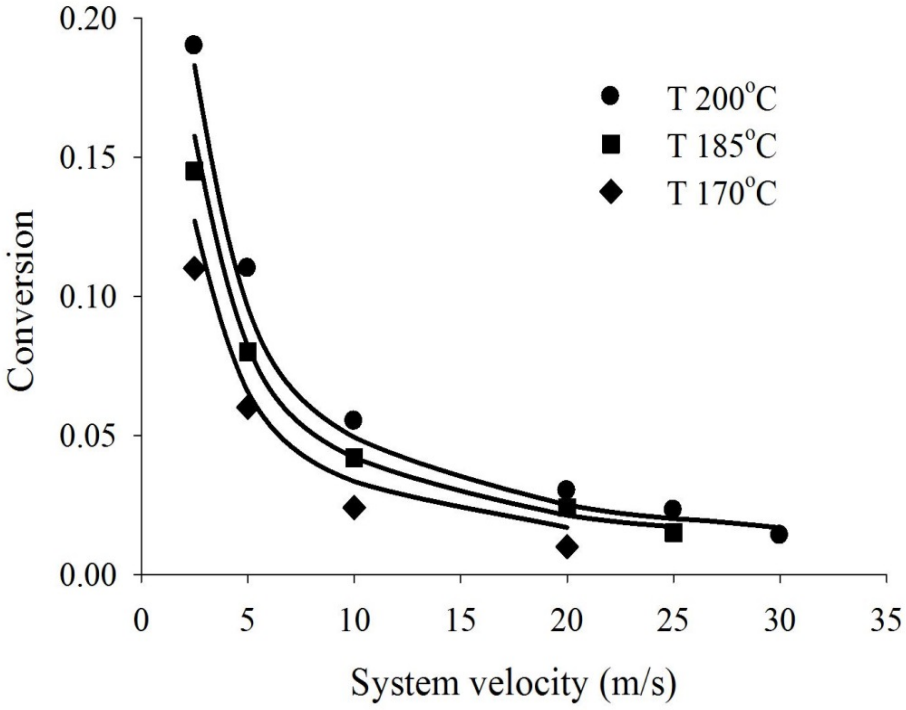

Figure VI.14: Comparison between model prediction and experimentally obtained toluene conversion at different system velocities using wash-coated monolith

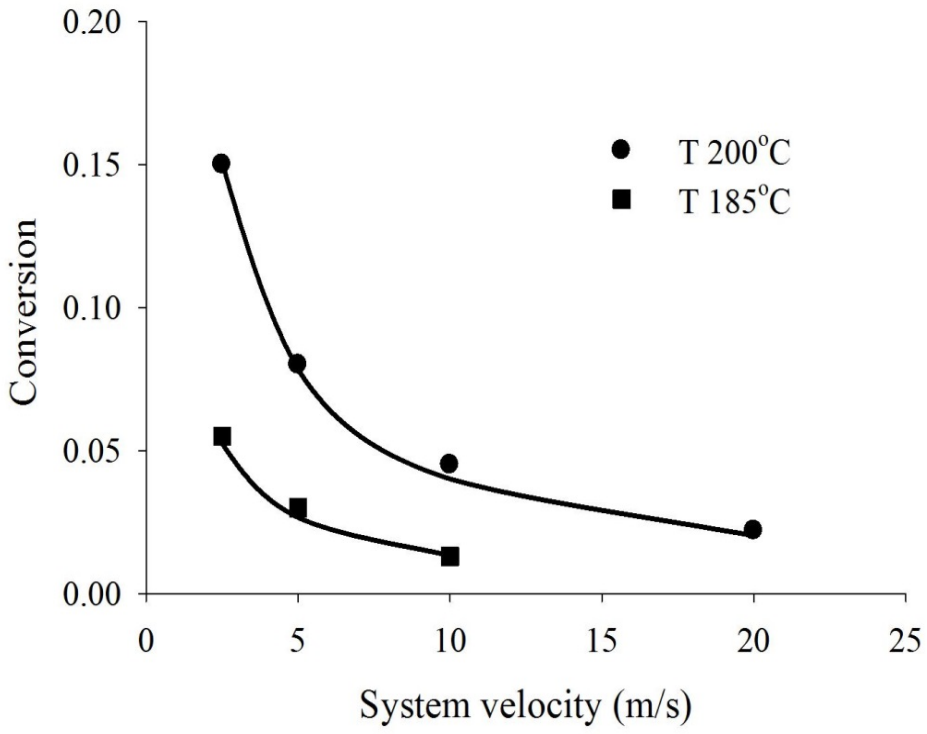

Figure VI.15: Comparison between model prediction and experimentally obtained conversion at different system velocities using wash-coated monolith

Based on the above results, activation energies for different reactor geometries were calculated and are shown in Table VI.4. For all cases, the total amounts of Pd and Mn were kept constant. Although the MFECs were differently pleated, the activation energies were almost equal for both cases whereas for the monolith this amount was significantly higher. This can be attributed to the variations in the percentage of metal loading. MFEC can possess higher percentage of metal loading than monolith in order to accumulate same amount of metal onto it. Furthermore, Table VI.4 contains the information of intra-layer residence times and Re numbers corresponding to the operating conditions. Small characteristic dimension of the MFECs enhanced the laminar behavior inside the media even though the system velocities were significantly high whereas in monolith, the flow was in turbulent region. The intra-layer

residence time corresponded to the space time in reactor geometry. As the MFEC thickness was substantially lower than the length of the monolith and the effective velocities were lower due to pleating, these residence times were low by an order of magnitude.

Table VI.4: Comparison among W-shaped MFEC, flat MFEC and wash-coated monolith

Structures	**Activation energy, E_a (kJ/mol)**			**Intra-layer residence time[a], (μsec)**	**Reynolds number[a], Re_p**
	Ethanol	**Toluene**	**n-Hexane**		
W-shaped MFEC	40.9 ± 5	58.9 ± 10	167 ± 6	2750 - 275	2.84 – 28.4
Flat MFEC	42.9 ± 3	61.2 ± 9	173 ± 10	690 - 69	11.4 - 114
Monolith (400 CPSI)	56.0 ± 2	71.0 ± 10	211 ± 7	49600 - 4960	90.2 - 902
Monolith (230 CPSI)	59.2 ± 4	73.4 ± 5	215 ± 5	49600 - 4960	122 - 1220

a: Values are calculated based on T = 473 K

In the above experiments, MFEC reactor operation was not in the inter-phase mass transfer controlled regime, and hence, there is further scope for improving the reactant conversion in MFEC by increasing the catalytic activity. In general, commercial monolith performs in inter-phase mass transfer controlled regime. Hence, a higher catalytic activity and a higher temperature will affect more positively the performance of MFEC than that of monolith.

In this study, higher temperatures could not be used due to the design limitations of the test apparatus. As the ethanol conversion was very low, the bed composition and properties of MFECs require further optimization. The bed properties and compositions of MFEC can be easily tailored based on the specific application. Hence, our future work will be MFEC optimization and operate it in inter-phase mass transfer controlled regime in order to achieve better conversion.

VI.5 Conclusion

Although mass transfer coefficients for the packed beds were higher than those of monoliths and MFECs, the heterogeneous contacting efficiencies for the same structures, regardless to the particle sizes, were found extremely low. Packed bed with small particle size offered high mass transfer rates but their associated pressure drop is high. Therefore, the packed beds were relatively inefficient in terms of contacting efficiency. Monoliths of various CPSI provided low resistance to flow due to the straight channel. However, the limitation of monolith was low inter-phase mass transfer rates. Hence, monolith performed better relative to the packed beds and the MFEC of low pleat numbers. Although MFEC with lower pleat number exhibited weak performance than monolith, the heterogeneous contacting efficiencies improved radically with the increase of pleat number. This increase in performance was the result of decreased effective velocity (inside the MFEC) due to the pleated formation. The decreased effective velocity lowered the pressure drop and increased the intra-layer residence time which resulted better conversion. This dual advantage provided by the pleated MFEC leads to higher η_{HCE} values compared to that of monoliths.

In the experimental study, MFEC with higher pleat numbers performed better than the monolith in terms of the ethanol conversions and the pressure drops. Experimentally obtained η_{HCE} values for the monolith and MFEC validated the theoretical findings. Hence, MFECs with higher pleat number have demonstrated better contacting efficiency in terms of pressure drops, conversions and mass transfer rates, theoretically and experimentally, compared to the conventional reactor systems i.e., packed bed and wash-coated monolith. Furthermore, the reaction kinetic model for the pleated MFEC was verified by the experimental findings. Pleated

MFEC showed promising performance as it provided a large surface/volume ratio for the entrapped catalyst. This attribute facilitates the weight and volume demand of the air handling system in a limited space. As this study showed some remarkable advantages of pleated MFEC, further improvements of MFEC bed properties and compositions (Pleat numbers, voidage, catalyst loading, etc.) appear to be very promising.

Chapter VII

Catalyst Characterization

VII.1 Introduction

Catalyst characterization is extremely important for catalyst development. This involves the measurement of critical parameters and properties of the catalysts. Heterogeneous catalyst having higher surface area, e.g., MFEC, requires undergoing characterization process. This characterization involves – elemental identification, chemical composition, chemical state, particle size distribution, surface area measurement, pore size distribution, imaging, metal dispersion, oxidation state of the metals, etc. A detailed analysis of MFEC, which resembles to "frozen fluidized bed" of catalyst particulates, is essential for understanding its performance and the associated reaction mechanism. In this research, mixed metal oxide e.g. Pd-Mn/Al_2O_3 catalyst exhibited better performance for VOCs removal than noble metal oxide (Pd/Al_2O_3) and transition metal oxide (Mn/Al_2O_3).

Several factors that could significantly affect the performance of Pd-Mn/Al_2O_3 catalyst were investigated in this chapter. Method of impregnation or volume of impregnation plays vital role for MFEC. Generally the volume of impregnation affects the homogeneity of the active species on the support. Higher impregnation volumes have been shown to produce more homogeneous catalysts. Smaller volumes of impregnation have been shown to render the properties of catalyst more sensitive to preparation variables. Higher volumes of impregnation produce high concentration gradients during the precursor drying stages and result in lower dispersion. A drying stage is employed to drive the precursor solvent from support. In general, drying is performed at temperatures near or above the boiling point of the solvent or under vacuum. The ratio of the precursor nucleation rate to crystal growth rate determines the crystal

size during solvent vaporization [169]. Calcination is generally carried out in an oxidizing atmosphere for precursor decomposition, formation of an oxide species, bonding of the formed oxide to the support, removal of some of the elements introduced during the impregnation step and sintering of the formed oxides. In this study, wet impregnation method was employed for catalyst preparation in order to obtain more homogeneous catalyst sites. Furthermore, applying dry impregnation of the prepared media was complicated.

A wide range of techniques are available for catalyst characterization. Selection of the techniques is another important issue. In this part, some intuitive techniques were employed on the catalyst particles that have been entrapped in microfibers. Inductively coupled plasma-atomic emission spectroscopy (ICP-AES) was employed for measuring the metal content (Pd and Mn). X-ray diffraction (XRD) was applied for identifying the metal and crystallite size. In order to have surface topography of MFEC and wash-coated monolith scanning electron microscopic (SEM) was applied. Temperature programmed reduction (TPR) indicated the reducibility of the metal oxide. N_2 physisorption and CO chemisorption were performed for surface area measurement, metal dispersion. Brief review of these characterization techniques have been provided in Section I.7.

VII.2 Characterization Techniques

VII.2.1 Inductively Coupled Plasma-Atomic Emission Spectroscopy (ICP-AES)

The catalyst particulates entrapped in MFEC and the wash-coated monolith went through ICP-AES analysis for measuring the metal content of the catalyst. This technique was performed by Hazen Research Inc. Table VII.1 shows the result of ICP-AES analysis, i.e., the amount metal deposited into the support particles of MFEC and wash-coated monolith. During catalyst

preparation in MFEC and monolith, same amount of pore volume was maintained. Table VII.2 shows the properties of the support particles, i.e., Al_2O_3 of MFEC and monolith.

Table VII.1: Metal content of the tested catalyst in MFEC and in monolith

Metal content (wt.%)	**MFEC**	**Monolith**
Pd	3.59	1.83
Mn	7.57	4.84

Table VII.2: Properties of the support particles in MFEC and in monolith

Properties	**MFEC**	**Monolith**
Pore volume (cc/g)	0.98	0.50
Total pore volume (cc)	15.3	15.0
Surface area (m^2/g)	247	220

VII.2.2 Scanning Electron Microscopy (SEM):

In this study, scanning electron microscopy was performed on both MFEC and monolith. The SEM images were obtained using a JEOL JSM 840 (20 kV) SEM. Fig. VII.1 shows the micrographs of MFEC where 150-250 µm Al_2O_3 are entrapped in 8 µm Ni fibers and unsintered Ni fibers. According to the figure, the fibers are infinitely long cylinder with ridges on the surface. These fibers are connected at their junction during sintering. Thereby, they create trap for the catalyst or support particles. Fig. VII.2 shows the SEM image of γ-Al_2O_3 particles those have been used for this study.

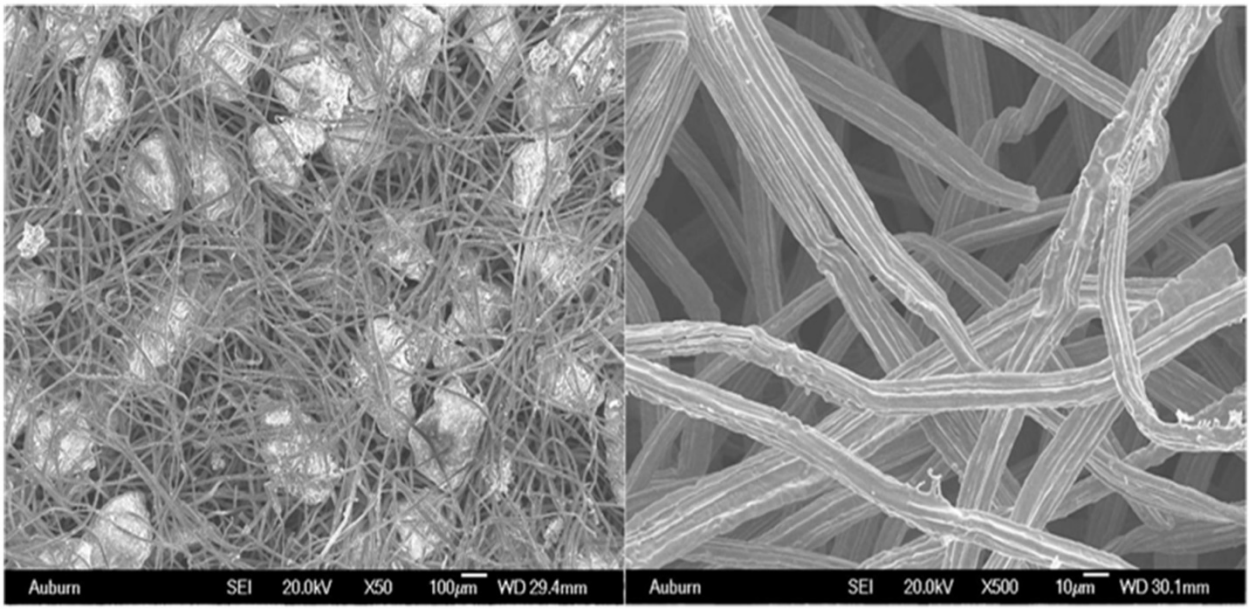

Figure VII.1: SEM image of (a) MFEC; (b) unsintered Ni fibers

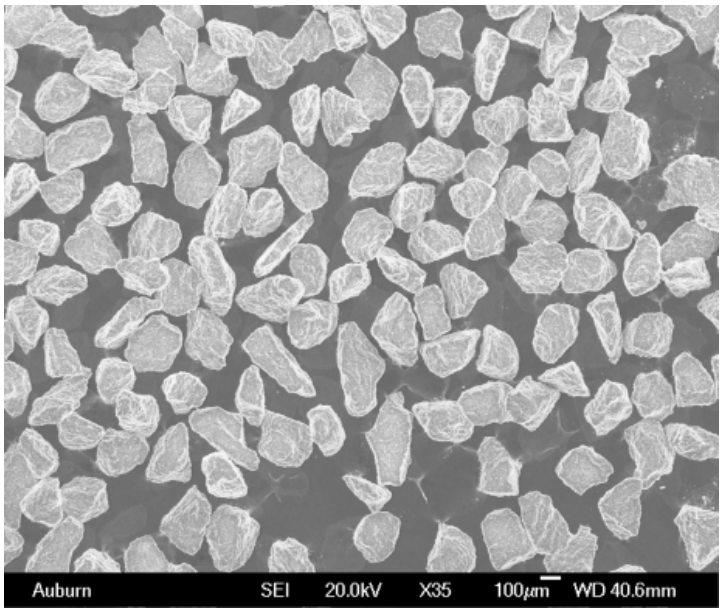

Figure VII.2: SEM image of 150-250 μm γ-Al_2O_3 particles

Fig VII.3 shows the change in monolith structure due to wash-coating. According to the figure, before applying wash-coat, the substrate was composed of porous ceramic compound. After applying wash-coat of support particles and catalyst, these pores were occupied. Due to continual wash-coating, multiple layers of support particles were formed. Furthermore, the change on the top surface due to wash-coating was observed. The surface topography was changed after applying coating. The topography showed that the coating was not uniform.

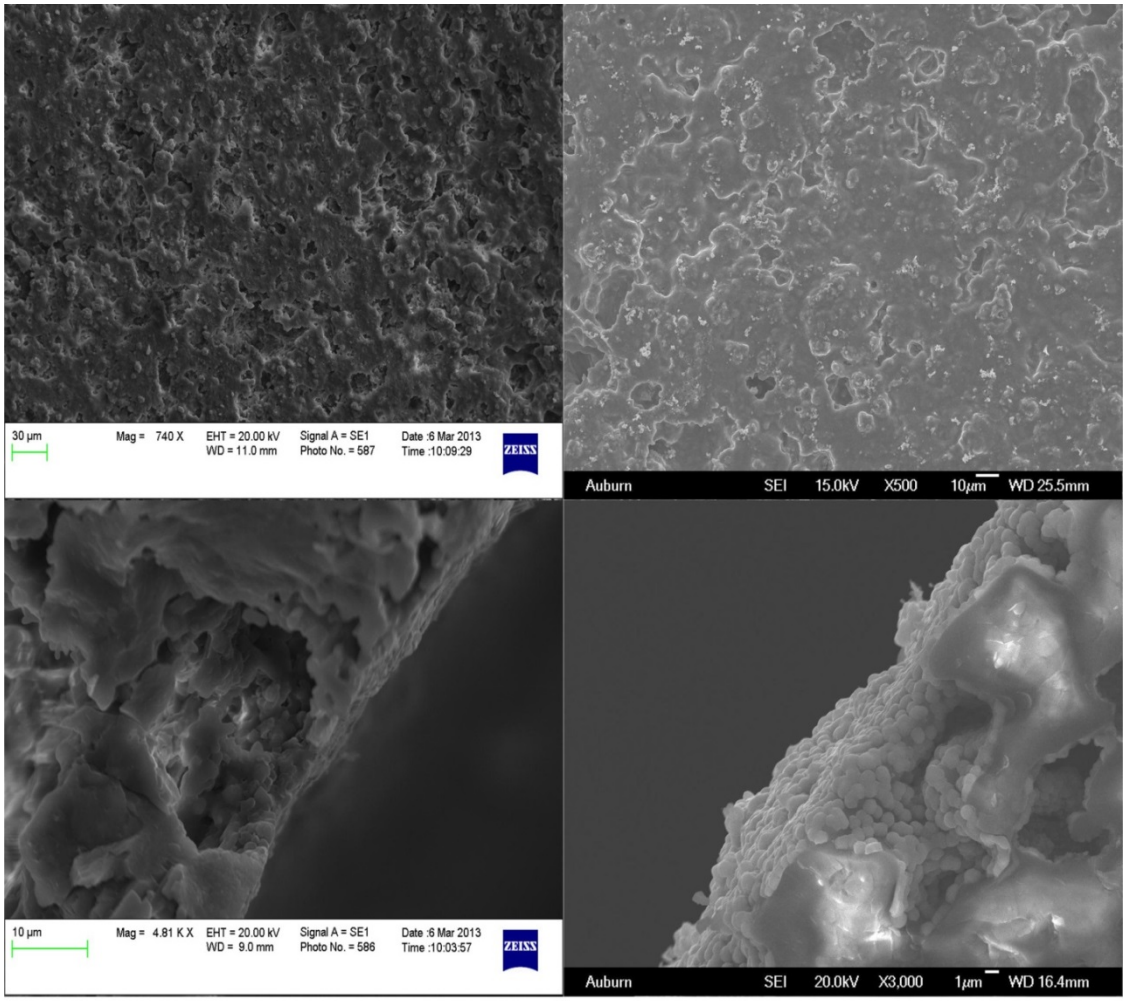

Figure VII.3: Micrograph of monolith (change in the structure after wash-coating the surface)

VII.2.3 X-Ray Diffraction (XRD):

The adsorbents were characterized via XRD in a Bruker D-8 x-ray diffractometer equipped with a CuKα (40KV/40mA) source. The XRD scan range was 20°–90° and the scan speed was 0.2 second/step (~3.76°/min). Fig. VII.4 shows the XRD plot of fresh γ-Al_2O_3 particles and sintered γ-Al_2O_3 particles. According to this figure, peaks are obtained at 37°, 45° and 68°. There is no significant change in peak position for the support particles which indicated that Al_2O_3 was in gamma phase after sintering. These peak positions can be used as reference while XRD will be performed on catalyst particles.

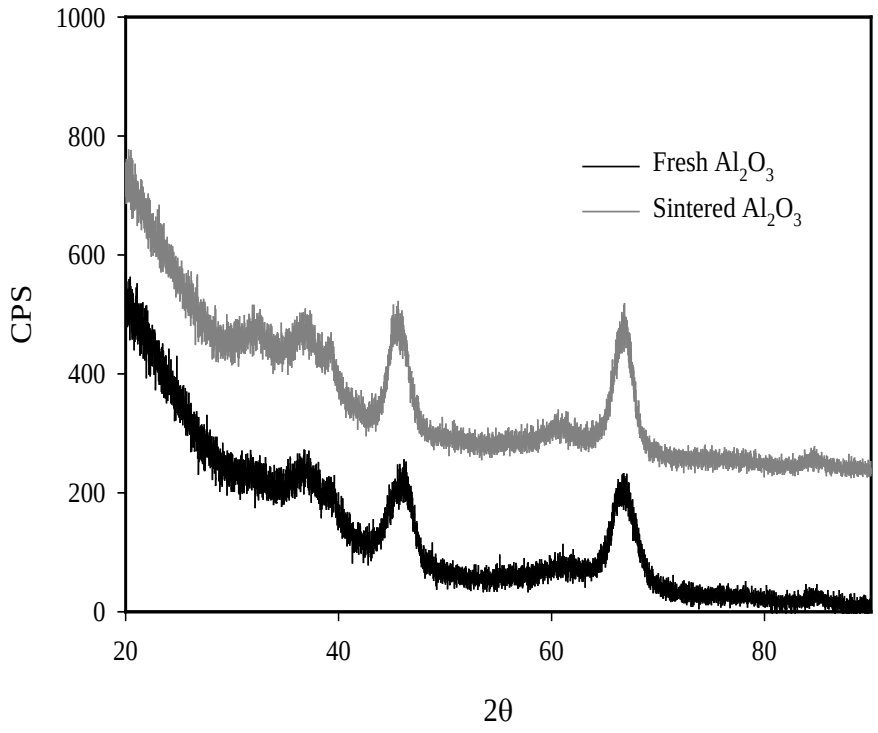

Figure VII.4: XRD plot of fresh γ-Al_2O_3 and sintered γ-Al_2O_3 particles

Fig.VII.5 shows the XRD peak of tested catalysts. All the samples primarily show Al_2O_3 peaks. For 3.59% PdO/Al_2O_3, there is a weak reflection of PdO (101) at 33.5° which is similar to the JCPDS 75-0584 [54, 170]. The reflection of PdO is weakly identifiable in the diffraction pattern, which indicates the predominant presence of PdO at the surface of catalyst. For Pd-Mn catalyst, the major peaks were obtained for γ-Al_2O_3. There is a very weak reflection of MnO_2 and PdO. This infers that the metals were in an amorphous or disordered phase or the particles were too small to be detected by XRD.

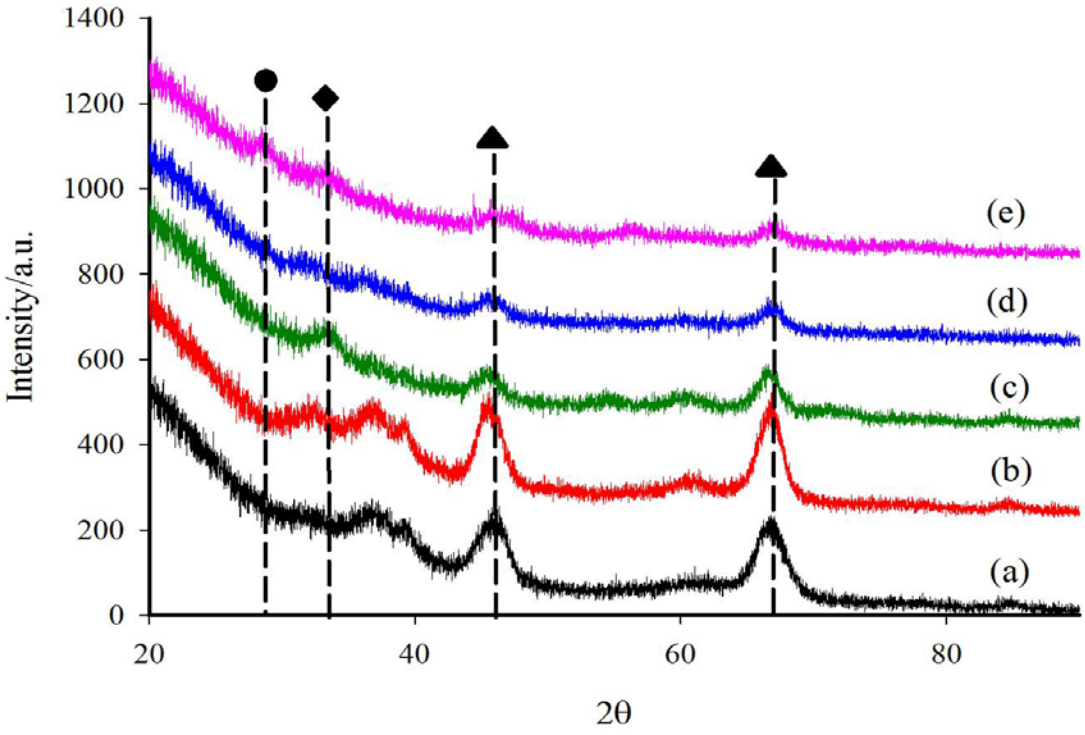

Figure VII.5: XRD plot (a) Fresh Al_2O_3; (b) Sintered Al_2O_3; (c) 3.59% PdO/Al_2O_3; (d) 7.57% MnO_x/Al_2O_3; and (e) 3.59% PdO-7.57% MnO_x/Al_2O_3 (●: MnO_2;▲: Al_2O_3; and ♦: PdO)

VII.2.4 Pore Volume and Surface Area Measurement:

In this study, properties of un-sintered and sintered γ-Al_2O_3, were obtained from N_2 physisorption other than the supplied data sheet. The data were collected using Quantachrome AS1 surface area and pore size analyzer. All the values were measured at 77 K. There were slight difference between experimentally obtained data and the product data sheet, as shown in Table VII.3. According to this table, the properties of support particles, i.e., pore diameter, pore volume, and surface area, changed due to sintering at high temperature. Due to sintering at 1173 K, pore blockage of the Al_2O_3 particle occurred. Furthermore, the available surface area by the support particles reduced significantly. Therefore, there was change in properties of support particles due to sintering, according to Table VII.4.

Table VII.3: Properties of the support particles obtained from the data sheet and BET isotherm

Properties	**Product data sheet**	**BET isotherm**
Surface area (m^2/g)	253	247
Pore volume	1.15	1.12
Average pore diameter (Å)	118	108.2

Table VII.4: Effect of sintering on the properties of support particles

Properties	**Before Sintering**	**After Sintering**
Surface area (m^2/g)	247	219.3
Pore volume (cm^3/g)	1.12	0.98
Average pore diameter (Å)	108.2	88.75

VII.2.5 CO Chemisorption:

Static CO chemisorption was performed to estimate the metal dispersion and active metal surface area of the mixed metal oxide catalyst using the same Quantachrome AS1 instrument. A stoichiometry of (1:1) was assumed for (CO:Pd) for chemisorption at 303 K. In order to get reproducible CO isotherms, the pre-treatment steps followed were: cleaning at 473 K using He for 1 h, evacuation at 473 K for 2 h, reduction at 573 K using H_2 for 1 h, removal of adsorbed H_2 in vacuum at 573 K in 1 h. For individual metal oxide catalysts (Mn/Al_2O_3 and Pd/Al_2O_3), the weight percent was obtained from the ICP-AES analysis. In case of mixed metal oxide, the catalyst particles were dislodged mechanically and were then analyzed in a powder form.

Active metal surface area, metal dispersion, and CO uptake increased for mixed oxide catalyst than those of individual metal oxide catalyst, according to Table VII.5. This infers that addition of Pd and Mn together enhanced the properties of the catalyst by producing more catalyst sites. Therefore, mixed metal oxide catalyst exhibited better performance, as shown in Fig. III.3.

Table VII.5: Properties of the tested metal catalysts

	Mn/Al_2O_3	**Pd/Al_2O_3**	**$Pd\text{-}Mn/Al_2O_3$**
Active metal surface area (m^2/g)	0.00617	1.851	1.978
Metal dispersion (%)	1.385	11.54	12.33
CO uptake (µmol/g)	1.301	39.02	41.70

VII.2.6 Temperature Programmed Reduction (TPR)

To measure the reducibility of the metal oxides, temperature programmed reduction (TPR) was performed. H_2-TPR was done by the gas-chromatography method using a thermal conductivity detector. The samples were pre-treated by passing air at 573 K for 2 h followed cooling at 298 K. Afterwards, the samples were heated up at a constant rate of 10°C/min in a 5% H_2-95% Ar stream at a flow rate of 15 cc/min. The consumption of hydrogen gas was measured from the effluent gas by using the TCD detector.

The TPR profiles of Pd/Al_2O_3, Mn/Al_2O_3, and $Pd\text{-}Mn/Al_2O_3$ are shown in Fig.VII.6. The reduction profiles of PdO and MnO_x are characterized by a single peak at 318 K and 738 K, respectively. However, in $PdO\text{-}MnO_x/Al_2O_3$ reduction profile, no peak was observed at 738 K. This indicates that Pd assisted reduction of Mn-O occurs. The absence of separate Mn-O peak confirmed the existence of bimetallic formation of Pd and Mn which inferred that there were so separate particles of Pd and Mn.

The TPR data was used to evaluate the reactivity of lattice oxygen towards H_2 in bimetallic oxide. Table VII.6 shows the amount of hydrogen consumed during TPR measurement. Since Al_2O_3 did not show any H_2 reduction, it was assumed that all the consumed H_2 contributes to the reduction of metal. Total H_2 consumption increased significantly due to the bimetallic formation of Pd-Mn. Due to the bimetallic formation, oxidation state of Pd and Mn might have changed, which enhanced the H_2 consumption.

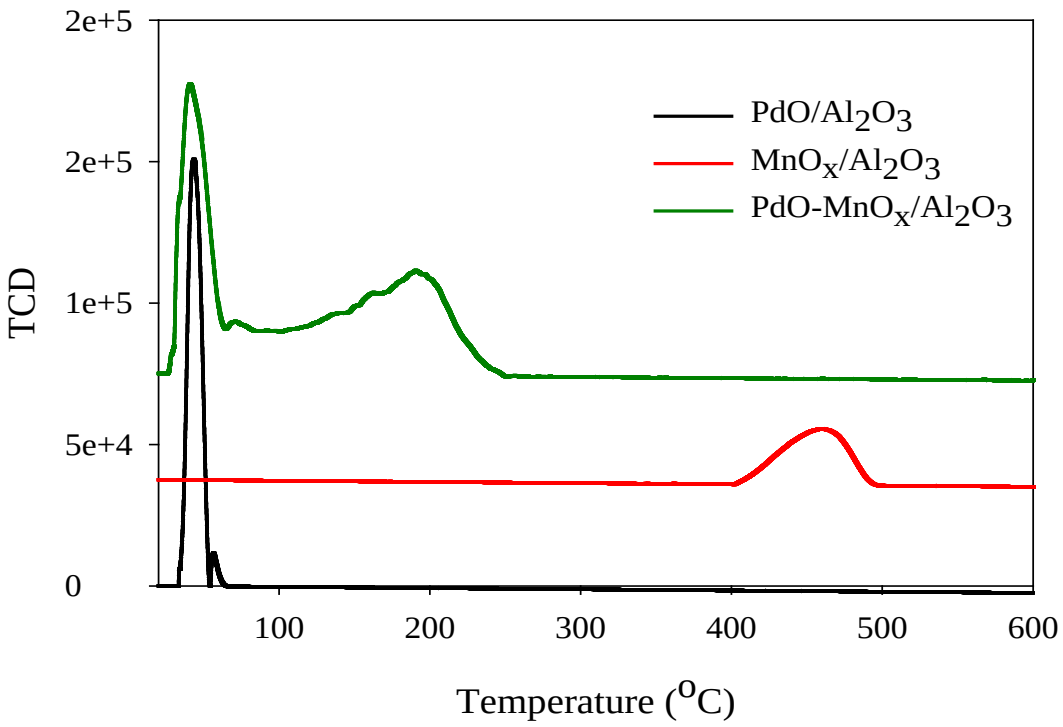

Figure VII.6: TPR profile of the tested catalysts

Table VII.6: H_2 consumption of the tested metal catalysts

Catalyst	H_2 consumption (µmol/g)
Al_2O_3	0.00
3.59% PdO/Al_2O_3	160.28
7.57% MnO_x/Al_2O_3	97.23
3.59% PdO-7.57% MnO_x/Al_2O_3	559.86

VII.3 Conclusion:

Catalyst characterization provides meticulous insight of mixed metal oxide supported catalyst. The ICP-AES analysis showed that MFEC was able to possess more metal content than

wash-coated monolith although they had same amount of pore volume and same concentration of the metal salt solution. There was no observable change in MFEC due to sintering except the joining of the metal fibers whereas for monolith, due to wash-coating the ceramic pores were occupied by the support particles and metals. However, the support particles are significantly smaller for wash-coated monolith than MFEC. Furthermore, the XRD analysis exhibited the amorphous state of metals on the support particle where the predominant peak was obtained for γ-Al_2O_3 even though the support particles had been sintered at high temperature. However, the porous properties and surface area of support particles changed considerably. In addition, CO chemisorption demonstrated the presence of more active sites and metal dispersion in Pd-Mn/Al_2O_3 catalyst than individual metal oxide catalysts. Hence, Pd-Mn/Al_2O_3 catalyst showed improved performance than the other tested catalyst. The TPR profile for the tested catalysts showed that Pd and Mn were in a bimetallic form which had higher reducibility i.e., H_2 consumption than PdO and MnO_x individually. This study may help to extend the knowledge of understanding the function of bimetallic oxide catalyst in case of VOC removal at high mass throughput system in a uniquely velocity controlled regime.

Chapter VIII

Conclusions & Recommendations for Future Work

VIII.1 Conclusions:

This study demonstrates catalytic removal of air contaminants i.e., VOC, using microfibrous entrapped catalyst for the application in automobile exhaust and fuel cell systems. Multi-elemental structured array of MFECs were developed with the intended application in air purification. This eliminates the weight and volume demand of the air handling devices. MESA enabled MFEC loaded with bimetallic Pd-Mn oxide catalyst on γ-Al_2O_3 can perform as an active catalytic structure for VOC removal in high volumetric flow rate system. However, optimum design study was required for this purpose which was achieved by performing pressure drop measurement across different pleated geometries. In addition to this catalytic VOC removal in pleated MFEC, reaction kinetics, reaction mechanism, comparative pressure drop study-theoretical and computational, comparative performance study among different heterogeneous contacting systems – conventional packed beds, wash-coated monolith and pleated MFECs. Investigation showed reaction followed Mars-Van Krevelen mechanism in this velocity controlled system where surface reaction is the limiting factor in the overall rate if reaction. Furthermore, pressure drop study will help to extend the knowledge of system energy requirement. The semi-empirical theoretical model provided an insight on inertial pressure loss and viscous pressure loss whereas computational method assisted to understand the flow behavior inside the pleated media. Moreover, pleated MFEC exhibited better than other contacting systems in terms of pressure drop, conversion, mass transfer and contacting efficiency. The reduced effective velocity inside the media, small catalyst particulates entrapped

in the microfibers, minimal thickness and pleating flexibility enhanced the performance of MFEC over other tested catalytic structure. Thus, this study has shown remarkable advantages of pleated MFEC as a catalytic reactor.

VIII.2 Recommendations for Future Work:

1. The pleated MFEC can be employed for different mixture of air contaminants (NO_x, VOC and O_3) in order to investigate the performance of the catalyst and inhibition effect of the contaminants. This will help to understand the use of a three way catalyst and will provide an understanding of practical automobile exhaust gas system. Furthermore, different VOC mixture can be injected as well.
2. The effluent from the system after the reaction requires investigation. This will help to understand the Mars-Van Krevelen mechanism and will also provide an idea the possible way to perform deep oxidation of VOCs.
3. The effect of high pressure inside the system (higher than ambient pressure) can be examined. The durability of the pleated MFEC, the change in the rate of reaction, and pressure drop occurring across the reactor can be measured through this investigation.
4. Different reactor geometries of pleated MFEC can be investigated. In this study, square geometries have been used for manufacturing convenience. However, this can be compared with round shape geometries in order to investigate the change in flow behavior and the performance.
5. Photo-catalysts are widely used in industry for VOC oxidation. By implementing photo-catalyst in this high volumetric system, VOC removal study can be performed and can be compared with the conventional pleated MFEC.

6. Improvisation of the high volumetric flow rate system is required in order to achieve high VOC conversion. This can be attained by increasing the system temperature and improving the bed properties (catalyst loading, thickness, pleat number, size of the reactor etc.). Temperature affects reaction significantly. However, as system is limited by temperature, changes in the bed properties can play an important role in this regard. This can be achieved by increasing media thickness or by perforating the media at random positions which will decrease the pressure drop and will increase the intra-layer residence time.
7. Global reaction and micro-scale reaction phenomena can be investigated by computational method in order to provide a deep insight of the reaction mechanism in this uniquely velocity controlled regime. This will help to demonstrate the reaction parameters which can be compared with the experimentally obtained results. Furthermore, this study can be performed for a wide range of temperatures, velocities and concentrations which are not possible to obtain in the high volumetric test recycle loop. Therefore, this study will assist to identify the optimum reaction condition for obtaining maximum output.
8. Temperature distribution across the media can also be performed.

References:

[1] T. Godish, Indoor Environmental Quality, Lewis Publishers, Boca Raton,FL, 2001.

[2] D. Moffat, W., **Handbook of indoor air quality management**, Prentice Hall, Englewood Cliffs, NJ, 1997.

[3] J.J. Schauer, M.J. Kleeman, G.R. Cass, B.R.T. Simoneit, Environmental Science & Technology 33 (1999) 1566-1577.

[4] J.J. Schauer, M.J. Kleeman, G.R. Cass, B.R.T. Simoneit, Environmental Science & Technology 36 (2002) 567-575.

[5] J.J. Schauer, M.J. Kleeman, G.R. Cass, B.R.T. Simoneit, Environmental Science & Technology 36 (2002) 1169-1180.

[6] J.M. Samet, M.C. Marbury, J.D. Spengler, Journal of Allergy and Clinical Immunology 79 (1987) 685-700.

[7] J.M. Samet, M.C. Marbury, J.D. Spengler, American Review of Respiratory Disease 137 (1988) 221-242.

[8] Friedlan.Sk, Environmental Science & Technology 7 (1973) 235-240.

[9] H. Akimoto, Science 302 (2003) 1716-1719.

[10] M. Wolfgang, K. Halfar, Air pollution control, Wright, H.D.,, US, 3911080, October 7, 1975.

[11] R.M. Heck, R.J. Farrauto, Catalytic Air Pollution Control: Commercial Technology, Van Nostrand Reinhold, New York, 1995.

[12] R.M. Heck, R.J. Farrauto, Applied Catalysis a-General 221 (2001) 443-457.

[13] D.R. Cahela, B.J. Tatarchuk, Catalysis Today 69 (2001) 33-39.

[14] B. Tatarchuk, M. Rose, A. Krishnagopalan, J. Zabasajja, D. Kohler, Mixed fiber composite structures high surface area high conductivity mixtures, US Patent 5,304,330, April 19, 1994.

[15] B.J. Tatarchuk, M.F. Rose, A. Krishnagopalan, Method of optimizing composite preparation for electrical properties: maximum capacitance electrodes, US Patent 5,102,745, April 7, 1992.

[16] B. Tatarchuk, M. Rose, A. Krishnagopalan, J. Zabasajja, D. Kohler, Preparation of mixed fiber composite structures, US Patent 5,080,963, January 14, 1992.

[17] B. Tatarchuk, M. Rose, A. Krishnagopalan, J. Zabasajja, D. Kohler, Mixed fiber composite structures, US Patent 5,096,663, March 17, 1992.

[18] B.K. Chang, B.J. Tatarchuk, Abstracts of Papers of the American Chemical Society 228 (2004) U686-U686.

[19] B.K. Chang, B.J. Tatarchuk, Abstracts of Papers of the American Chemical Society 226 (2003) U569-U569.

[20] B.K. Chang, B.J. Tatarchuk, Journal of Materials Engineering and Performance 15 (2006) 453-456.

[21] B.K. Chang, Y. Lu, H.Y. Yang, B.J. Tatarchuk, Journal of Materials Engineering and Performance 15 (2006) 439-441.

[22] Y. Lu, N. Sathitsuksanoh, H.Y. Yang, B.K. Chang, A.P. Queen, B.J. Tatarchuk, in: Y. Wang, J.D. Holladay (Eds.), Microreactor Technology and Process Intensification, 2005, pp. 406-422.

[23] H.Y. Yang, N. Sathitsuksanoh, Y. Lu, B.J. Tatarchuk, Abstracts of Papers of the American Chemical Society 230 (2005) U1655-U1656.

[24] H. Yang, Y. Lu, B.J. Tatarchuk, Journal of Power Sources 174 (2007) 302-311.

[25] H.Y. Yang, D.R. Cahela, B.J. Tatarchuk, Chemical Engineering Science 63 (2008) 2707-2716.

[26] H.Y. Yang, R. Sothen, D.R. Cahela, B.J. Tatarchuk, Industrial & Engineering Chemistry Research 47 (2008) 10064-10070.

[27] B.K. Chang, Y. Lu, B.J. Tatarchuk, Chemical Engineering Journal 115 (2006) 195-202.

[28] L.Y. Chen, B.K. Chang, Y. Lu, W.G. Yang, B.J. Tatarchuk, Abstracts of Papers of the American Chemical Society 224 (2002) U568-U568.

[29] A.P. Queen, High efficiency adsorption filters via packed bed + polishing sorbent architectures of regenerable collective protection equipment, Chemical Engineering, Auburn University, Auburn, AL, 2005.

[30] R.R. Kalluri, D.R. Cahela, B.J. Tatarchuk, Separation and Purification Technology 62 (2008) 304-316.

[31] M. Meffert, Preparation and characterization of sintered metal microfiber-based composite materials for heterogeneous catalyst applications, Chemical Engineering, Auburn University, Auburn, AL, 1998.

[32] R.R. Kalluri, D.R. Cahela, B.J. Tatarchuk, Applied Catalysis B-Environmental 90 (2009) 507-515.

[33] M. Sheng, H.Y. Yang, D.R. Cahela, B.J. Tatarchuk, Journal of Catalysis 281 (2011) 254-262.

[34] U.S.E.P. Agency, Our Nation's Air: Status and Trends through 2010, Research Triangle Park, NC, 2012.

[35] R.J. Farrauto, R.M. Heck, Kinetics and Catalysis 39 (1998) 594-599.

[36] R.M. Heck, S. Gulati, R.J. Farrauto, Chemical Engineering Journal 82 (2001) 149-156.

[37] D.K. Harris, D.R. Cahela, B.J. Tatarchuk, Composites Part a-Applied Science and Manufacturing 32 (2001) 1117-1126.

[38] R.K. Duggirala, C.J. Roy, S.M. Saeidi, J.M. Khodadadi, D.R. Cahela, B.J. Tatarchuk, Journal of Fluids Engineering-Transactions of the Asme 130 (2008).

[39] R.R. Kalluri, Microfibrous entrapped catalysts and sorbents: Microstructured heterogeneous contacting systems with enhanced efficiency, Chemical Engineering, Auburn University, Auburn, AL, 2008.

[40] www.epa.gov/iaq/voc.

[41] N.R. Council, The Airliner Cabin Environment and the Health of Passengers and Crew, National Academy Press, Washington, DC, 2002.

[42] T. Salthammer, Organic Indoor Air Pollutants: Occurrence - Measurement - Evaluation, Wiley-VCH, December, 2007.

[43] C. Jia, S. Batterman, C. Godwin, Atmospheric Environment 42 (March, 2008).

[44] N. Klepeis, W. Nelson, W. Ott, J. Robinson, A. Tsang, P. Switzer, J. Behar, S. Hern, W. Engelmann, J. Expo. Anal. Env. Epidemiol 11(3) (May-June, 2001).

[45] T. Woodruff, D. Axelard, J. Caldwell, R. Morello-Frosch, A. Rosenbaum, Environmental Health Aspect 106(5) (1998).

[46] Y. Kim, S. Harrad, R. Harrison, Environ. Sci. Technol 35 (2001).

[47] D. Walkinshaw, G. Mitalas, C. McNeil, K. Preston, Environment control system for aircraft having interior condensation problem reduction, cabin air quality improvement, fire suppression and fire venting functions, US Patent 6,491, 254, Dec. 10, 2002.

[48] E.C. Moretti, N. Mukhopadhyay, Chemical Engineering Progress 89 (1993) 20-26.

[49] A. Kolodziej, J. Lojewska, Catalysis Today 105 (2005) 378-384.

[50] R.K. Shah, B. Thonon, D.M. Benforado, Applied Thermal Engineering 20 (2000) 631-650.

[51] C. Kennes, F. Thalasso, Journal of Chemical Technology and Biotechnology 72 (1998) 303-319.

[52] R.E. Hester, R.M. Harrison, Volatile Organic Compounds in the Atmosphere, RSC Cambridge, 1995.

[53] S. Todorova, H. Kolev, J.P. Holgado, G. Kadinov, C. Bonev, R. Pereniguez, A. Caballero, Applied Catalysis B-Environmental 94 (2010) 46-54.

[54] S.K. Ihm, Y.D. Jun, D.C. Kim, K.E. Jeong, Catalysis Today 93-5 (2004) 149-154.

[55] W.B. Li, J.X. Wang, H. Gong, Catalysis Today 148 (2009) 81-87.

[56] S.K. Gangwal, M.E. Mullins, J.J. Spivey, P.R. Caffrey, B.A. Tichenor, Applied Catalysis 36 (1988) 231-247.

[57] J.J. Spivey, Industrial & Engineering Chemistry Research 26 (1987) 2165-2180.

[58] P. Papaefthimiou, T. Ioannides, X.E. Verykios, Applied Catalysis B-Environmental 13 (1997) 175-184.

[59] P. Papaefthimiou, T. Ioannides, X.E. Verykios, Applied Thermal Engineering 18 (1998) 1005-1012.

[60] P. Papaefthimiou, T. Ioannides, X.E. Verykios, Catalysis Today 54 (1999) 81-92.

[61] K. Everaert, J. Baeyens, Journal of Hazardous Materials 109 (2004) 113-139.

[62] O. Levenspiel, Chemical Reaction Engineering, 3rd ed., John Wiley & Sons, Inc, 1999.

[63] H. Fogler, Elements of Chemical Reaction Engineering, 4th ed., Prentice-Hall, Inc, NJ, USA, 2006.

[64] Encyclopedia of Environmental Control Technology, Gulf Publishing Co., 1989.

[65] R.M. Heck, R.J. Farrauto, Applied Catalysis A: General 221 (2001), 443-457.

[66] R.M. Heck, S. Gulati, R.J. Farrauto, Chemiccal Engineering Journal 82 (2001), 149-156.

[67] J.L. Williams, Catalysis Today 69 (2001), 3-9.

[68] A. Cybulski, J.A. Moujlin, Structured Catalysts and Reactors, CRC Press, Boca Raton, FL, 2006.

[69] J. Zhidong, K.-S. Chung, G.-R. Kim, J.-S. Chung, Chemical Engineering Science 58 (2003), 1103-1111.

[70] J.L. Hu, Y. Wang, D. VanderWiel, C. Chin, D. Palo, r. Rozmiarek, R. Dagle, J. Holladay, E. Baker, Chemical Engineering Journal 93 (2003), 55-60.

[71] A.Y. Tonkovich, S. Perry, Y. Wang, D. Qiu, T. LaPlante, W.A. Rogers.

[72] A.Y. Tonkovich, J.L. Zilka, M.J. LaMont, Y. Wang, R.S. Wegeng, Chemical Engineering Science 54 (1999), 2947-2951.

[73] H. Pennemann, V. Hessel, H. Lowe, Chemical Engineering Science 59 (2004), 4789-4794.

[74] K.F. Jensen, Microreactor Technology and Process Intensification, ACS Syposium Series 914, Washington, DC, September 7-11, 2003.

[75] P.D.I. Fletcher, S.J. Haswell, E. Pombo-Villar, B.H. Warrington, P. Watts, S.Y.F. Wong, X. Zhang, Tetrahedron 58 (2002), 4735-4757.

[76] K.F. Jensen, Chemical Engineering Science 56 (2001), 293-303.

[77] D. Kunni, O. Levenspiel, Fluidization Engineering, 2nd ed., Butterworth-Heinemann, Boston, 1991.

[78] P.N. Dwivedi, S.N. Upadhyay, Industrial & Engineering Chemistry Process Design and Development 16 (1977) 157-165.

[79] V. Balakotaiah, S.M.S. Dommeti, Chemical Engineering Science 54 (1999) 1621-1638.

[80] E. Tronconi, A. Beretta, Catalysis Today 52 (1999) 249-258.

[81] J. Richardson, Principles of Catalyst Development, Plenum Press, New York, 1989.

[82] C.H. Bartholomew, R.J. Farrauto, Fundamentals of Industrial Catalytic Processes, 2nd ed., John Wiley and Sons, Inc, NJ, 2006.

[83] http://nanonet.rice.edu/research/BET/.

[84] S. Lowell, J.E. Shields, M.A. Thomas, M. Thommes, Characterization of porous solids and powder:Surface area, pore size and density, Kluwer Academic Publishers, Netherlands, 2004.

[85] K. Kohse-Hoinghause, J.B. Jeffries, Applied Combustion Diagonistics, 2002.

[86] D.D. Eley, E.K. Rideal, The catalysis of the parahydrogen conversion by tungsten, Proc. R. Soc., 1941.

[87] P. Mars, D.W.V. Krevelen, Chemical Engineering Science 3 (1954), 41-59.

[88] S. Scire, P.M. Riccobene, C. Crisafulli, Applied Catalysis B-Environmental 101 (2010) 109-117.

[89] S. Larrondo, A. Barbaro, B. Irigoyen, N. Amadeo, Catalysis Today 64 (2001) 179-187.

[90] P. Nithiarasu, K. Ravindran, Computer Methods in Applied Mechanics and Engineering 165 (1998) 147-154.

[91] P. Nithiarasu, K.N. Seetharamu, T. Sundararajan, Communications in Numerical Methods in Engineering 14 (1998) 241-251.

[92] H. Darcy, Les Fontaines Publiques de la Ville de Dijon (1856).

[93] A.E. Scheidegger, The physics of flow through porous media, University of Toronto Press, Toronto, Canada, 1974.

[94] S. Ergun, Chem. Engr. Prog. 48 (1952), 89-95.

[95] F.C. Blake, Trans. Amer. Inst. Chem. Engrs. 14 (1922).

[96] I.J. Kozeny, Wasserkraft und Wasserwertschaft, 1931.

[97] S.P. Burke, W.B. Plummer, Industrial and Engineering Chemistry 20 (1928), 1196-1200.

[98] L.-S. Fan, C. Zhu, Principles of gas-solid flows, Cambridge University Press, New York, 1998.

[99] R.B. Bird, W.E. Stewart, E.N. Lightfoot, Transport Phenomena, 2nd ed., John Wiley & Sons, Inc, New York, 2007.

[100] J.M. Coulson, J.F. Richardson, J.R. Backhurst, J.H. Harker, Coulson and Richardson's Chemical Engineering, Butterworth-Heinemann.

[101] D. Nemec, J. Levec, Chemical Engineering Science 60 (2005) 6947-6957.

[102] D. Handley, P.J. Heggs, Transactions of the Institution of Chemical Engineers and the Chemical Engineer 46 (1968).

[103] H.C. Brinkman, Appl. Sci. Research A1 (1949).

[104] D.A. Nield, A. Bejan, Convection in porous media, Springer Science + Business Media, NY, USA, 2006.

[105] M.A.A. Spaid, F.R. Phelan, Physics of Fluids 9 (1997) 2468-2474.

[106] L. Durlofsky, J.F. Brady, Physics of Fluids 30 (1987) 3329-3341.

[107] R. Rivers, D. Murphy, ASHRAE Transactions 106 (2000).

[108] A. Bensoussan, J.L. Lions, G. Papanicolaou, Comptes Rendus Hebdomadaires Des Seances De L Academie Des Sciences Serie A 281 (1975) 89-94.

[109] A. Bensoussan, J.L. Lions, G. Papanicolaou, Comptes Rendus Hebdomadaires Des Seances De L Academie Des Sciences Serie A 282 (1976) 143-147.

[110] A. Bensoussan, J.L. Lions, G. Papanicolaou, Comptes Rendus Hebdomadaires Des Seances De L Academie Des Sciences Serie A 284 (1977) 587-592.

[111] A. Narasimhan, J.L. Lage, Journal of Heat Transfer-Transactions of the Asme 123 (2001) 31-38.

[112] D.A. Anderson, J.C. Tannehill, R.H. Pletcher, Computational Fluid Mechanics and Heat Transfer, McGraw Hill, 1984.

[113] J.D. Anderson, Computational Fluid Dynamics: The Basics with Applications, McGraw-Hill, New York, 1995.

[114] S. Middleman, An Introduction to Fluid Dynamics: Principles of Analysis and Design, 2nd ed., Wiley, New York, 1998.

[115] H.P.A. Calis, J. Nijenhuis, B.C. Paikert, F.M. Dautzenberg, C.M. van den Bleek, Chemical Engineering Science 56 (2001) 1713-1720.

[116] A.G. Dixon, M.E. Taskin, M. Nijemeisland, E.H. Stitt, Chemical Engineering Science 63 (2008) 2219-2224.

[117] A.G. Dixon, M.E. Taskin, M. Nijemeisland, E.H. Stitt, Industrial & Engineering Chemistry Research 49 (2010) 9012-9025.

[118] M. Nijemeisland, A.G. Dixon, E.H. Stitt, Chemical Engineering Science 59 (2004) 5185-5191.

[119] M.E. Taskin, A.G. Dixon, M. Nijemeisland, E.H. Stitt, Industrial & Engineering Chemistry Research 47 (2008) 5966-5975.

[120] A. Guardo, M. Coussirat, M.A. Larrayoz, F. Recasens, E. Egusquiza, Chemical Engineering Science 60 (2005) 1733-1742.

[121] A. Guardo, M. Coussirat, F. Recasens, M.A. Larrayoz, X. Escaler, Chemical Engineering Science 61 (2006) 4341-4353.

[122] http://en.wikipedia.org/wiki/Finite_volume_method.

[123] http://math.nist.gov/mcsd/savg/tutorial/ansys/FEM/.

[124] U.S. Dixit, Finite element method: An introduction.

[125] B.E. Launder, D.B. Spalding, Lectures in Mathematical Models of Turbulence, Academic Press, London, England, 1972.

[126] B. Maze, Q. Wang, H.V. Tafreshi, B. Pourdeyhimi, Journal of Aerosol Science 38 (2007), 550-571.

[127] Q. Wang, B. Maze, H.V. Tafreshi, B. Pourdeyhimi, Chemical Engineering Science 61 (2006), 8085-8088.

[128] S. Zobel, B. Maze, H.V. Tafreshi, Q. Wang, B. Pourdeyhimi, Chemical Engineering Science 62 (2007), 6285-6296.

[129] X. Chen, T.D. Papathanasiou, Composites, Part A: Applied Science and Manufacturing 37 (2006), 836-846.

[130] X. Chen, T.D. Papathansiou, Transport in Porous Media 71 (2007), 233-251.

[131] M.M. Tomadakis, T.J. Robertson, Journal of Composite Materials 39(2) (2005), 163-188.

[132] http://www.nae.edu/nae/bridgecom.nsf/weblinks/MKEZ-5HUM3J?OpenDocument.

[133] A.N. Karwa, B.J. Tatarchuk, Separation and Purification Technology 86 (2012), 55-63.

[134] R.A. Sothen, B.J. Tatarchuk, Hvac&R Research 15 (2009) 269-286.

[135] W. Chu, H. Windawi, Chemical Engineering Progress 92 (1996) 37-43.

[136] G. Centi, Journal of Molecular Catalysis a-Chemical 173 (2001) 287-312.

[137] C. Lahousse, A. Bernier, P. Grange, B. Delmon, P. Papaefthimiou, T. Ioannides, X. Verykios, Journal of Catalysis 178 (1998) 214-225.

[138] B.A. Tichenor, M.A. Palazzolo, Environmental Progress 6 (1987) 172-176.

[139] J. Hermia, S. Vigneron, Catalysis Today 17 (1993) 349-358.

[140] S. Vigneron, P. Deprelle, J. Hermia, Catalysis Today 27 (1996) 229-236.

[141] R. Sothen, Novel Packaging Designs for Improvement in Air Filtration Performance, Chemical Engineering, Auburn University, Auburn, AL, 2009.

[142] A. Trovarelli, Catalysis Reviews-Science and Engineering 38 (1996) 439-520.

[143] C.T. Campbell, C.H.F. Pendden, Science 29 (2005), 713-714.

[144] S.S.T. Bastos, S.A.C. Carabineiro, J.J.M. Orfao, M.F.R. Pereira, J.J. Delgado, J.L. Figueiredo, Catalysis Today 180 (2012) 148-154.

[145] S.M. Sager, D.I. Kondarides, X.E. Verykios, Applied Catalysis B-Environmental 103 (2011) 275-286.

[146] S.C. Kim, W.G. Shim, Applied Catalysis B-Environmental 98 (2010) 180-185.

[147] A. O'Malley, B.K. Hodnett, 3rd World Congress on Oxidation Catalysis 110 (1997) 1137-1144.

[148] R. Spinicci, A. Tofanari, M. Faticanti, I. Pettiti, P. Porta, Journal of Molecular Catalysis a-Chemical 176 (2001) 247-252.

[149] S. Wahid, B.J. Tatarchuk, Industrial & Engineering Chemistry Research, 52 (2013), 15494-15503.

[150] A.S. Foust, L.A. Wenzel, C.W. Clump, L. Maus, L.B. Anderson, Principles of Unit Operations, 2nd ed., John Wiley & Sons, Inc, New York, 1980.

[151] P.C. Carman, Transactions, Institute of Chemical Engineering 15 (1937), 150-166.

[152] P.C. Carman, Flow of Gases through Porous Media, Butterworths Scientific Publications,, London, 1956.

[153] C.N. Davies, Air Filtration, Academic Press, 1973.

[154] S.F. Chien, Spe Drilling & Completion 9 (1994) 281-289.

[155] R.C. Brown, Air Filtration: An Integrated Approach to the Theory and Application of Fibers Filters, Pergamon Press, Oxford, 1993.

[156] ANSYS FLUENT 12.0: User's Guide.

[157] C.J. Roy, Journal of Computational Physics 205 (2005) 131-156.

[158] E.N. Fuller, Schettle.Pd, J.C. Giddings, Industrial and Engineering Chemistry 58 (1966) 19-27.

[159] M. Uberoi, C.J. Pereira, Industrial & Engineering Chemistry Research 35 (1996) 113-116.

[160] D.H. West, V. Balakotaiah, Z. Jovanovic, Catalysis Today 88 (2003) 3-16.

[161] G.F. Froment, K.B. Bischoff, Chemical reactor analysis and design, Wiley, New York, 1990.

[162] S. Wahid, D.R. Cahela, B.J. Tatarchuk, Industrial & Engineering Chemistry Research, 52 (2013), 14472-14482.

[163] R. Peffer, I&EC Fundamentals 3 (1964), 380-383.

[164] C. Plana, S. Armenise, A. Monzon, E. Garcia-Bordeje, Topics in Catalysis 54 (2011) 914-921.

[165] E. Garcia-Bordeje, I. Kvande, D. Chen, M. Ronning, Advanced Materials 18 (2006) 1589-+.

[166] E. Garcia-Bordeje, I. Kvande, D. Chen, M. Ronning, Carbon 45 (2007) 1828-1838.

[167] T.A. Nijhuis, A.E.W. Beers, T. Vergunst, I. Hoek, F. Kapteijn, J.A. Moulijn, Catalysis Reviews-Science and Engineering 43 (2001) 345-380.

[168] L. Giani, G. Groppi, E. Tronconi, Industrial & Engineering Chemistry Research 44 (2005) 4993-5002.

[169] L. Page, Applied Heterogeneous Catalysis: Design, Manufacture, Use of Solid Catalysts, 1987.

[170] T. Maillet, C. Solleau, J. Barbier-Jr, D. Duprez, Applied Catalysis B-Environmental 14 (1997) 85-95.